

证明材料目录

附件 1-论文证明材料	1
附件 2-专利证明材料	35
附件 3-项目证明材料	36



Aggregation-induced emission nanoprobe assisted ultra-deep through-skull three-photon mouse brain imaging



Mubin He^{a,1}, Dongyu Li^{c,1}, Zheng Zheng^{d,1}, Hequn Zhang^{a,e}, Tianxiang Wu^a, Weihang Geng^a, Zhengwu Hu^c, Zhe Feng^a, Shiyi Peng^a, Liang Zhu^e, Wang Xi^e, Dan Zhu^c, Ben Zhong Tang^{b,*}, Jun Qian^{a,*}

^a State Key Laboratory of Modern Optical Instrumentations, Centre for Optical and Electromagnetic Research, College of Optical Science and Engineering, International Research Center for Advanced Photonics, Zhejiang University, Hangzhou 310058, China

^b Shenzhen Institute of Aggregate Science and Technology, School of Science and Engineering, The Chinese University of Hong Kong, Shenzhen, 2001 Longxiang Boulevard, Longgang District, Shenzhen, Guangdong 518172, China

^c Britton Chance Center for Biomedical Photonics, Wuhan National Laboratory for Optoelectronics, MoE Key Laboratory for Biomedical Photonics, Huazhong University of Science and Technology, Wuhan, Hubei 430074, China

^d School of Chemistry and Chemical Engineering, Hefei University of Technology, Hefei 230009, China

^e Interdisciplinary Institute of Neuroscience and Technology (ZIINT), College of Biomedical Engineering and Instrument Science, Zhejiang University, Hangzhou 310027, China

ARTICLE INFO

Article history:

Received 6 March 2022

Received in revised form 29 May 2022

Accepted 20 June 2022

Available online xxxx

Keywords:

Aggregation-induced emission

Brain imaging

Through skull

Optical clearing

Three-photon microscopy

ABSTRACT

Optical microscopy has enabled *in vivo* monitoring of brain structures and functions with high spatial resolution. However, the strong optical scattering in turbid brain tissue and skull impedes the observation of microvasculature and neuronal structures at a large depth. Herein, we proposed a strategy to overcome the influence induced by the high scattering effect of both skull and brain tissue via the combination of skull optical clearing (SOC) technique and three-photon fluorescence microscopy (3PM). The visible-NIR-II compatible skull optical clearing agents (VNSOCA) we applied reduced the skull scattering and water absorption in long wavelength by refractive index matching and H₂O replacement to D₂O respectively. 3PM with the excitation in the 1300-nm window reached 1.5 mm cerebrovascular imaging depth in cranial window assisted by a kind of bright aggregation-induced emission (AIE) nanoprobe we developed with a large three-photon absorption cross section. Combining the two advanced technologies together, we achieved so far the largest cerebrovascular imaging depth of 1.0 mm and neuronal imaging depth of > 700 μm through intact mouse skull. Dual-channel through-skull imaging of both brain vessels and neurons was also successfully realized, giving an opportunity of non-invasively monitoring the deep brain structures and functions at single-cell level simultaneously.

© 2022 Elsevier Ltd. All rights reserved.

Introduction

Brain structural and functional imaging is essential for monitoring neuronal circuitry and pathogenesis of brain diseases including Alzheimer's disease and Parkinson's disease [1–6]. Optical imaging is optimal for its high spatial resolution, real-time performance and free of ionizing radiation. However, the strong scattering effect of biological tissues [7] has impeded it from observing vasculature and neuronal structures at a large depth. Many technologies

have been developed to reduce the scattering effect, including photoacoustic tomography [8–12] with acoustic penetration, optical coherent tomography [13–15] with optical heterodyne amplification, and so on. However, these modalities performed poorly in neuronal structure imaging due to the lack of specific mark to neuron, let alone neuronal dynamic imaging.

The mouse cortex is mainly protected by the skull, which exhibits strong scattering, causing a severe limitation for large-depth and high-contrast optical imaging. In fact, several technologies have been proposed to avoid the influence of optical scattering caused by the skull, including the open-skull glass window [17], the thinned-skull cranial window [18,19] and the skull optical clearing window [20,21]. The open-skull glass window, which is formed by removing

* Corresponding authors.

E-mail addresses: tangbenz@cuhk.edu.cn (B.Z. Tang), qianjun@zju.edu.cn (J. Qian).

¹ These authors contribute equally.

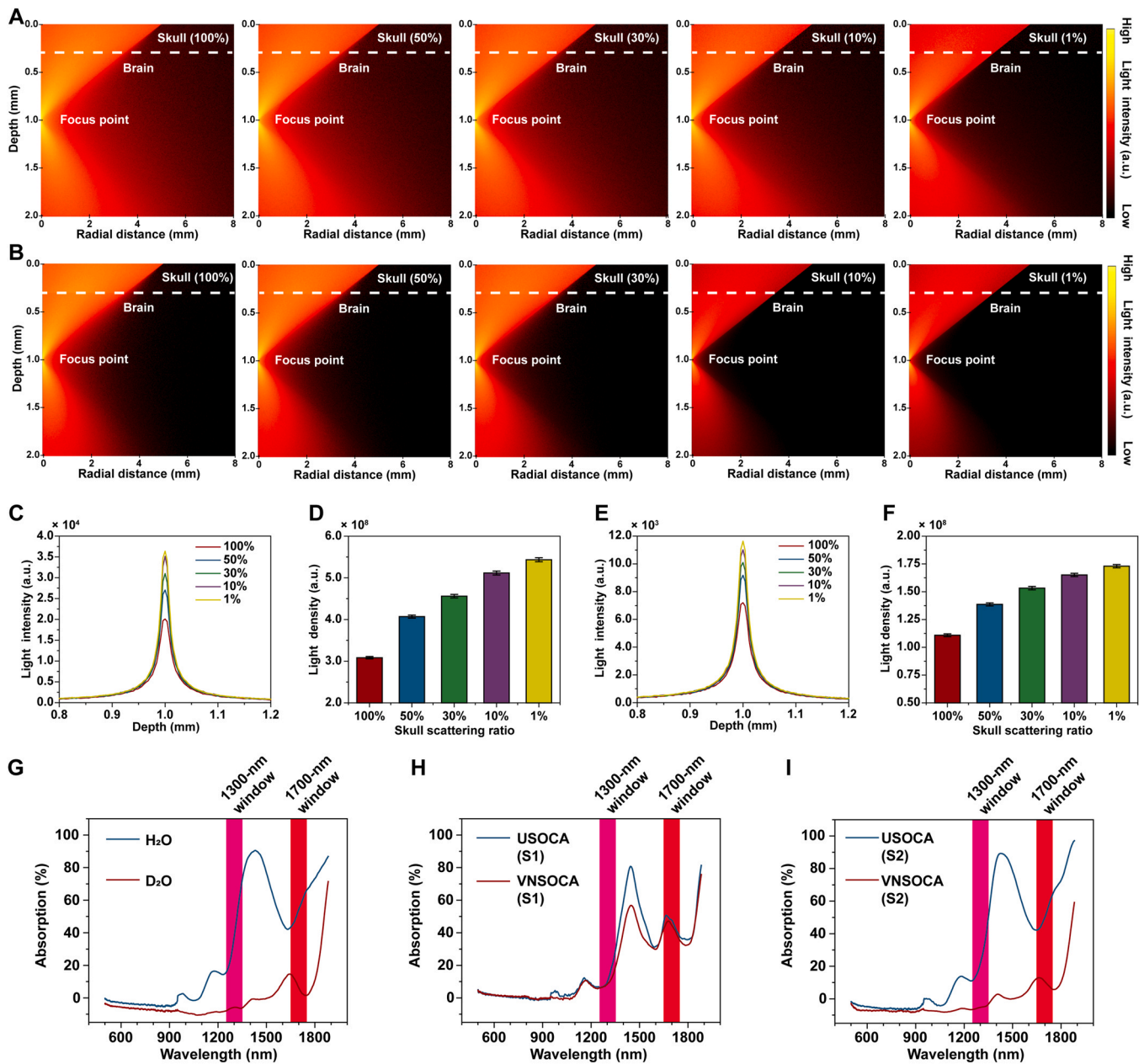


Fig. 1. Skull scattering reduction improved performance of through-skull 3PM. (A–B) R-Z plane light distribution simulation of excitation light in the 1300-nm window (A) and the 1700-nm window (B) penetrating through skull and brain tissue with different remaining skull scattering ratio (100–1%). Focal depth = 1 mm. Each photon package, which was generated randomly outside the tissue, propagated toward the focus point in tissue. Stimulated imaging contrast in (A) and (B) was adjusted respectively. (C, E) Light intensity profiles along the depth (Radial distance = 0 mm) from 0.8 mm to 1.2 mm with different remaining skull scattering ratios (100–1%) in the 1300-nm window (C) and the 1700-nm window (E). (D, F) Light density (light intensity divided by focal spot area) at the focal point with different remaining skull scattering ratio (100–1%) in the 1300-nm window (D) and the 1700-nm window (F). (G) Absorption spectra of H₂O and deuterium oxide (D₂O). (H, I) Absorption spectra of solution 1 (S1) and immersed solution 2 (S2) of USOCA and VNSOCA. (Optical length = 1 mm).

a part of skull and replacing with a glass coverslip, tends to induce a series of inflammatory reactions and increase intracranial pressure [22]. The thinned-skull cranial window, which is literally formed by thinning the skull, requires operating repeatedly due to bone growth and is difficult to use [18]. However, the skull optical clearing window, which locally applies some chemical agents to the skull for refractive index matching, is safe and repeatable, without any craniotomy [20]. Previously developed skull optical clearing windows have enabled repeated imaging of the dendritic protrusions, microglia dynamics and blood capillaries, combined with optical microscopy [20,21]. Nevertheless, most of them employed H₂O as solution, which has large absorption coefficient in near-infrared region,

especially beyond 1300 nm. This would inevitably cause adverse impact on optical imaging with near-infrared excitation or emission.

In addition, mouse brain tissue also exhibits strong scattering effect and impedes deep imaging, unable to be resolved by *in vivo* tissue optical clearing technology at present. Fortunately, three-photon fluorescence microscopy (3PM) is a typical way for deep imaging with high contrast in turbid tissue [23]. The character of long-wavelength excitation light with low tissue scattering guarantees 3PM large penetration depth, thus maintaining well focus efficiency in turbid tissue [24]. Meanwhile, high-order nonlinear optical effect of three-photon fluorescence (3PF) ensures the localized excitation, and therefore improves imaging resolution and contrast. The two acknowledged long-wavelength excitation windows for

3PM are the 1300-nm and 1700-nm spectral ranges [25], both of which have long attenuation length at brain tissue. Among the two excitation windows, the 1300-nm window is favored for its lower tissue absorption induced heating effect. Moreover, considering universal commercial fluorescent probes for neuronal labeling, the 1300-nm window is more commonly used in 3PF neuronal structural and functional imaging [26,27], and more capable of simultaneous multi-color imaging [28]. However, 3PM using the 1300-nm excitation under the intact skull currently achieved only ~300 μm neuronal imaging depth [27] and 510 μm cerebrovascular imaging depth [27] owing to the low excitation efficiency.

Developing fluorescent probes with bright 3PF intensity would be helpful for increasing three-photon brain imaging depth. The 3PF intensity of a probe attributes to its three-photon action cross section, which consists of three-photon absorption cross section (σ_3) and quantum yield [28]. Aggregation-induced emission (AIE) luminogen [29] is a kind of ideal organic three-photon fluorophore. When forming aggregates in nanoprobe, the intramolecular motion of AIE molecules are restricted and their nonradiative process is restrained. Thus, the quantum yield of AIE nanoprobe can be enhanced accordingly [30]. In addition, the large amount of AIE molecules inside can improve the σ_3 of nanoprobe effectively [31]. Though some of the AIE molecules are photobleached by femtosecond (fs) irradiation with high peak power during imaging, most ones are unbleached and can still emit fluorescence. Thus, the photostability of AIE molecule encapsulated nanoprobe are maintained [32]. Moreover, when AIE molecules are coated with amphiphilic organic polymers to form AIE nanoparticles (NPs), the hydrophilicity and biocompatibility of AIE NPs are also ameliorated. Features above including highly bright 3PF intensity, high photostability and excellent biocompatibility insure AIE nanoprobe quite appropriate for 3PM. However, recently reported AIE nanoprobe were mostly excited by the fs laser at 1500–1700 nm spectral region [33–35]. Few of them were applied in the 1300-nm excitation window [36].

Herein, we combined *in vivo* skull optical clearing (SOC) technique and 1300-nm excited 3PM to overcome the scattering and absorption of the skull as well as brain during deep-cortical visualizing. Skull scattering reduction could improve the performance of 3PM effectively according to Monte Carlo simulation results. The visible-NIR-II compatible skull optical clearing agents (VNSOCA) we applied introduced D_2O solution to replace H_2O solution. Therefore, the light scattering and absorption of skull in the 1300-nm window were both reduced effectively. Afterwards, we realized largest 3PF through-skull cerebrovascular imaging depth (1.0 mm), assisted by a kind of AIE nanoprobe called DCBT NP, whose isolated molecule possesses extremely larger σ_3 ($3.53 \times 10^{-78} \text{ cm}^6 \text{ s}^2 \text{ photon}^{-2}$ at 1300 nm) than other reported organic probes [36]. Meanwhile, 3PF through-skull neuronal imaging also improved to > 700 μm depth. With prominently reduced scattering effect and near-infrared absorption of skull, 3PM in the 1300-nm window achieved dual-channel deep imaging of both brain vessels and neurons under the intact skull for the first time.

Results

Skull scattering reduction improved performance of through-skull 3PM

Skull scattering is one of the major barriers that constrains the through-skull imaging quality. And SOC technique could reduce the skull scattering effectively. Herein, we performed Monte Carlo simulation to investigate how SOC would enhance the performance of three-photon excitation due to the better focusing inside brain tissue. Fig. 1A shows the simulated distribution of light intensity when the 1300-nm light was focused on the brain tissue through skull with the scattering of skull decreasing. Fig. 1B states the

situation when a 1700-nm light was focused on the brain tissue. It was obvious that reducing the skull scattering would effectively reduce the out-of-focus light both for 1300-nm window and 1700-nm window (Fig. 1A–B and Fig. S1). In addition, quantitative analysis demonstrated that, both the light intensity and light density at the focus point were getting better as the skull scattering coefficient decreased in the 1300-nm window (Fig. 1C and 1D) and the 1700-nm window (Fig. 1E and 1F). In addition, we simulated the amount of signal intensity left at the skull surface after penetrating through brain tissue and skull when the emission was generated at certain depth of brain. As shown in Fig. S2, the signal light showed similar distribution on the surface as the skull scattering coefficient decreased. However, the overall light intensity penetrating successfully to the surface obviously increased as the skull scattering coefficient decreased (Fig. S3). Simulation results above verified the skull scattering reduction induced by SOC could promisingly increase the light density of the three-photon excitation light at focus point, and decrease the attenuation of the generated three-photon emission signals before detected.

Light absorption by water in near-infrared region was another factor that should be considered while applying the skull optical clearing agent (SOCA) to 3PM. Since deuterium oxide (D_2O) has been applied as an immersion medium in near-infrared imaging for its reduced absorption in near-infrared region (Fig. 1G) [37]. In this work we prepared VNSOCA which replaced H_2O in urea-based skull optical clearing agents (USOCA) with deuterium oxide solution. Then we used Monte Carlo simulation to compare two SOCA to investigate the impact of absorption of the SOCA (Fig. 1H and 1I) on 3PM. As shown in Fig. S4, after SOC treatment, solution 2 (S2) of the SOC was remained on the skull for imaging. Therefore, simulations were performed to investigate the 1300-nm and 1700-nm light focusing ability when S2 of USOCA and VNSOCA covered skull. As shown in Fig. S5, compared with USOCA, VNSOCA can increase the 1300-nm light density at the focal point by 1.25 times. Similarly, as shown in Fig. S6, VNSOCA can increase the 1700-nm light density at the focal point by 2 times. However, in the case of VNSOCA, the absolute value of 1700-nm light density was lower than that of 1300-nm light density at the focal point (1.4×10^4 VS 3.1×10^4), due to stronger brain tissue absorption.

Furthermore, we also performed *ex vivo* 3PM test to verify the skull clearing effect by VNSOCA. A kind of lab-synthesized AIE nanoprobe named DCBT NP (the details will be discussed later), and a lab-built three-photon microscopic system (Fig. S7), were used for the test. The results indicated that, covered by an intact skull, the 3PF signals of DCBT NPs-filled capillary were rather weak. On the contrary, when the skull was treated by VNSOCA, the signals were remarkably increased (Fig. S8). In addition, VNSOCA treatment also increased the signal-to-background ratio (SBR, Fig. S9) and the resolving power (Fig. S10) of 3PM.

Overall, VNSOCA assisted skull optical clearing could reduce both light absorption by water in near-infrared region and skull scattering, therefore enhanced the performance of through-skull 3PM.

3PF properties of DCBT NPs under 1300-nm and 1700-nm excitation windows

The benefits of long excitation wavelength and high-order non-linear optical confinement attributed to 3PM were effective ways to overcome the scattering effect in deep brain imaging. The greatest advantages of the 1300-nm excitation window against the 1700-nm excitation window are its much lower tissue absorption and higher excitation efficiency.

We conducted the Monte Carlo simulation of temperature rising caused by tissue absorption of excitation light in Fig. S11–S13. Compared with 1700-nm window, temperature rising in the 1300-nm window was obviously milder. Also, the temperature

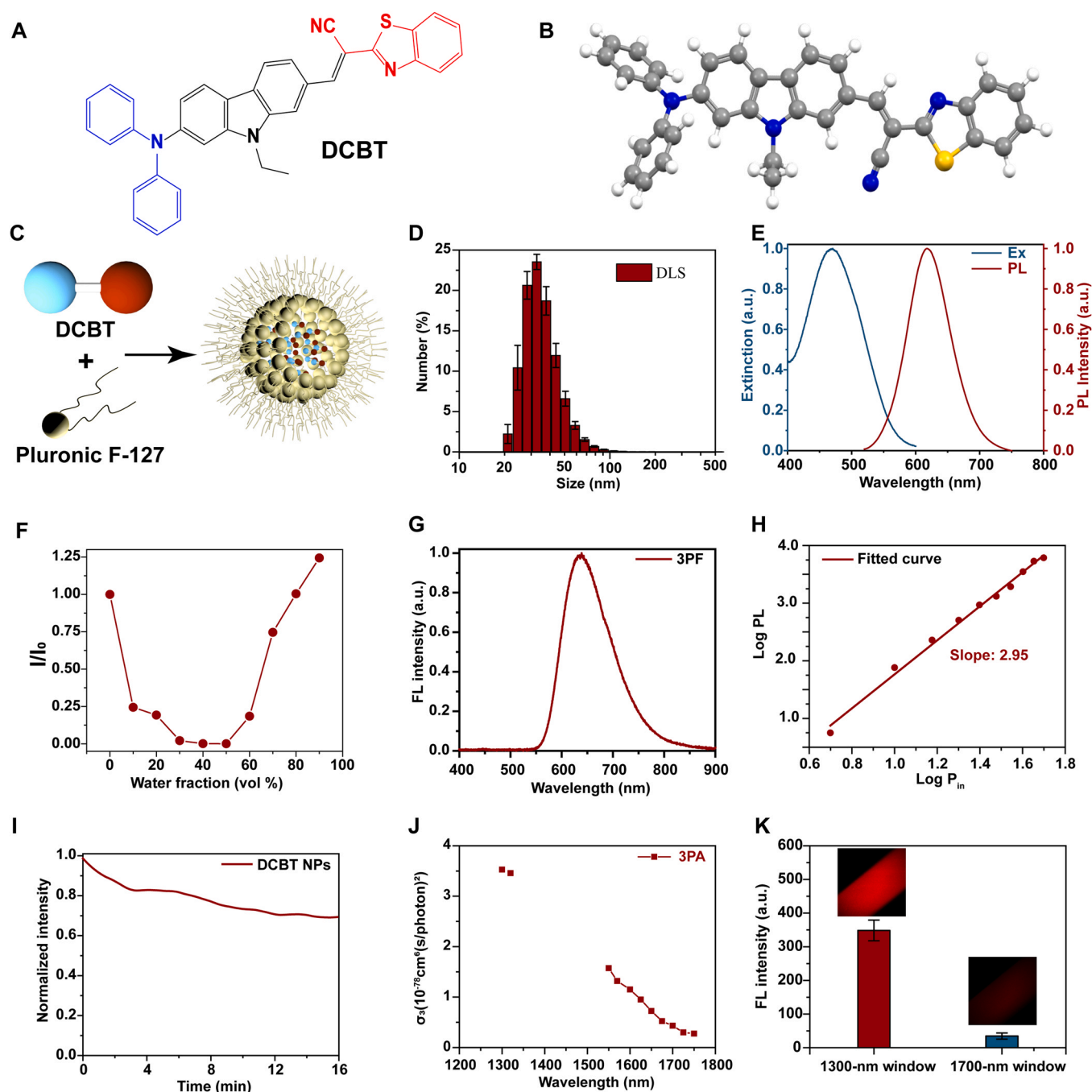


Fig. 2. Optical properties of DCBT NPs. (A) Molecular structure and (B) optimized molecular geometry of DCBT. (C) Schematic illustration of the fabrication of DCBT NPs. (D) DLS results of DCBT NPs. (E) Normalized extinction and PL spectra of DCBT NPs. (F) Plot of relative 3PF intensity (I/I_0) vs different water fractions (f_w) of the acetone/water mixtures of DCBT, [DCBT] = 20 μM . (G) 3PF spectrum of DCBT NPs under the excitation of 1300 nm fs laser. (H) Power dependence of fluorescence intensity of DCBT NPs under the 1300 nm fs excitation intensity. (I) Photostability of DCBT NPs under the continuous irradiation of 1300 nm fs laser (Average power: 7 mW). (J) Measured σ_3 of DCBT molecules in CHCl_3 solution from 1300 nm to 1750 nm. (K) 3PF intensity of DCBT NPs under the excitation of 1300-nm window and 1700-nm window. Insert: 3PF images of DCBT NPs filled in the glass capillary.

distribution in the 1300-nm window was more dispersive, avoiding local overheating at focused point. On the contrary, 1700-nm light would cause a sharp temperature rise near the focus, where overheated damage tended to happen easier.

In addition, compared with the 1700-nm excitation window, the 1300-nm excitation window should obtain higher excitation efficiency and fluorescence intensity for its shorter wavelength according to the multi-photon fluorescence photon flux formula [38]. However, the low σ_3 of most fluorescence probes restricted their 3PF intensity from further strengthening. Fortunately, we currently

developed an AIE fluorophore named DCBT with large σ_3 which was realized by the intra- and intermolecular synergistic engineering. The compound (Fig. 2A) can be readily synthesized, and the detailed synthetic process are presented in Supporting Information (Scheme S1). The optimized molecular geometry of DCBT indicated that 2-benzothiazoleacetonitrile and carbazole skeleton were essentially planar, which allowed good π -electron delocalization over the whole molecule (Fig. 2B). The strong push-pull character and the extended π -conjugation of DCBT may effectively lead to near-infrared emission and large σ_3 value. The photophysical property of DCBT at aggregated

state was studied by increasing the water fraction ($f_w = \text{volume (water) / volume (water + acetone)}$) in acetone/water mixture (Fig. S14–S15). The photoluminescence (PL) intensity of DCBT was dramatically decreased as the water fraction increased from 0% to 50%, while further increasing f_w from 60% to 90% resulted in the enhanced PL intensity because of the aggregates formation. This phenomenon revealed the AIE feature of DCBT. Then, we tried to seal it into the aggregated nanoparticles. As shown in Fig. 2C, DCBT were encapsulated by F-127, which was approved by the US Food and Drug Administration (FDA), to form amphiphatic organic nanoparticles. The results of dynamic light scattering (DLS, 36.2 ± 1.9 nm, Zetasizer Nano-ZS) in Fig. 2D showed the micellar systems were uniformly distributed. The extinction and PL spectra were displayed in Fig. 2E. The quantum yield of DCBT NPs was measured as 3.17%. Afterwards, we measured the nonlinear optical character of DCBT. With increasing f_w from 60% to 90% in acetone/water mixture, DCBT molecules showed similar enhanced 3PF intensity under the 1300-nm fs excitation, which further confirmed aggregation-induced 3PF enhancement (Fig. 2F and Fig. S16). As shown in Fig. 2G, DCBT NPs generated red emission spectrum with a peak at ~ 640 nm under the 1300-nm fs excitation. In addition, the dependence relationship between the nonlinear fluorescence intensity and the excitation light intensity was measured. As shown in Fig. 2H, the logarithm of the emission intensity against that of the excitation intensity showed a linear slope of approximately 2.95, indicating a major three-photon absorption process under 1300-nm fs excitation. Moreover, 3PF intensity decreased by only 30% over 16 min of continuous irradiation (Fig. 2I), suggesting the promising photostability of DCBT NPs for 3PF. Furthermore, σ_3 of DCBT at various wavelengths were measured, since it was the major feature manifesting the 3PF capability of an optical probe. Results showed that, the σ_3 of DCBT at 1300 nm was much larger than that at 1700 nm (Fig. 2J). The largest σ_3 at 1300 nm within the test range was calculated to be $3.53 \times 10^{-78} \text{ cm}^6 \text{ s}^2 \text{ photon}^{-2}$, which is a much higher value than the reported organic probes [28,36]. Hence, 3PF intensity excited at the 1300-nm wavelength was ~ 10 times higher than that excited at the 1700-nm wavelength (Fig. 2K).

Therefore, with the help of the improved σ_3 of DCBT NPs and lower heating effect, *in vivo* 3PF imaging in the 1300-nm window would be more suitable for the observation of brain tissue with the high scattering.

In vivo deep 3PF brain vasculature imaging of the mouse with the open-skull glass window

With the assistance of DCBT NPs and utilization of open-skull glass window (Fig. 3A), we adopted 3PF to perform ultra-deep visualization of mouse cerebral vessels. The mouse was imaged after injected with DCBT NPs dispersion (1.5 mg/mL, 0.2 mL). DCBT NPs in blood and liver (Fig. S17) showed slightly blue-shifted fluorescence, which brought no influence for *in vivo* three-photon fluorescence cerebrovascular imaging. Fig. 3B showed 3D reconstruction of cerebral vessels under the excitation of 1700-nm window and 1300-nm window. The imaging depth of 3PF using the 1700-nm window only reached 1.1 mm (Fig. S18) due to the low three-photon action cross section. In contrast, 3PF performed with the 1300-nm window could reach 1.5-mm imaging depth. This imaging depth has already passed through the white matter layer and reached the hippocampus regions, and broke the previously reported organic probe-assisted 3PF imaging depth record (1.4 mm [36]) using the 1300-nm window.

Brain vessels at various depth was shown in Fig. 3C–J. The tiny blood capillary with a size of $3.7 \mu\text{m}$ could be distinguished at the 1.5 mm depth (Fig. 3J and Fig. S19). We firstly verified the position of white matter based on the third-harmonic generation (THG) microscopic imaging of mouse brain using a kind of nanocrystal. As

shown in Fig. S20, THG signal outside blood vessels appeared from $850 \mu\text{m}$ depth and disappeared at $1050 \mu\text{m}$ depth, which indicated that the position of white matter was within depth between $850 \mu\text{m}$ and $1050 \mu\text{m}$ roughly. Images at neocortex layer maintained extremely high SBR due to the background-free feature of 3PF as shown in Fig. 3K. Some large blood vessels were observed from white matter layer to hippocampus layer, which was consistent with the results in previous 3PF deep imaging works [39–41]. Because of the higher scattering effect of white matter, SBR appeared to decrease when the region of interest (ROI) travelled through it (Fig. 3K). Such situation is similar to what was observed in long-wavelength excited confocal fluorescence imaging [42].

Nevertheless, even with relatively low SBR (~ 2), the vessels were still distinguishable. 3D reconstruction of brain vessels in the 1.1–1.3 and 1.3–1.5 mm was displayed in Fig. 3L–M. Large blood vessels extended up to 1.5 mm below was displayed clearly. However, it was the working distance of the objective (2 mm) that constrained imaging depth available in our experiment. As demonstrated by the results above, the scattering effect of brain was effectively overcome by 3PF with the improved σ_3 of DCBT NPs in the 1300-nm excitation window.

In vivo deep brain 3PF under the 1300-nm excitation window with the optical clearing window

Combining the SOC technique and 3PF together, we performed 3PF microscopic imaging of the mouse with the skull optical clearing window. The schematic of mouse head imaging was displayed in Fig. 4A. The typical bright field view of the mouse brain vasculature after skull clearing in Fig. 4B showed more apparent than that before skull clearing. Intensity analysis of vasculature under the VNSOCA treated skull in Fig. 4C demonstrated four distinct brain vessels, which were almost invisible under the untreated turbid skull. Afterwards, the 3PF cerebrovascular imaging before and after skull clearing were carried out on mouse injected with DCBT NPs. As Fig. 4D–G showed, 3PF imaging performed through the original skull had only reached $550 \mu\text{m}$, which was comparable with the previously reported imaging depth [27]. On the contrary, after VNSOCA treatment on the skull to decrease its scattering, 3PF imaging of the same field of view showed enhanced signal intensity and optimized SBR (Fig. 4H–O), especially at large depth. The final 3PF imaging depth reached 1.0 mm through the skull optical clearing window (Fig. 4P–S). The small blood vessel with a diameter of $4.5 \mu\text{m}$ at $700 \mu\text{m}$ depth was clearly visualized (Fig. 4P, T). Moreover, a $10.4 \mu\text{m}$ vessel at $1000 \mu\text{m}$ depth could also be distinguished (Fig. 4S, U). 3D reconstruction of brain vessels from 0 to $1000 \mu\text{m}$ was displayed in Fig. 4V. To the best of our knowledge, our 3PF achieved the largest millimeter-level imaging depth under the intact skull, thanks to the reduced skull scattering induced by VNSOCA and reduced brain tissue scattering overcome by 3PF.

Apart from cerebrovascular imaging, visualization of mouse brain neurons at neocortex layers was also conducted under the intact skull. As shown in Fig. 5A–D, not only the signal intensity, but also the SBR and resolution of neuronal dendrite were considerably enhanced at shallow depth after skull optical clearing. Fig. 5E–F showed that the skull optical clearing treatment introduced a 6-time improvement of the 3PF intensity, and compressed the half-height full width of an imaged dendrite from $3.1 \mu\text{m}$ to $1.2 \mu\text{m}$ at $25 \mu\text{m}$ depth. More abundant dendrites emerged at the depths of $75 \mu\text{m}$ and $160 \mu\text{m}$ after skull optical clearing compared with those observed through original skull (Fig. 5G–J).

Thanks to the strengthened signal level and improved image contrast after skull clearing, we were able to track the deep axons of *Thy-1-GFP* neurons from 250 to $700 \mu\text{m}$ (Fig. 5K and Fig. S21). The vivid *Thy-1-GFP* neuron structures were visualized clearly after skull optical clearing, with improved imaging depth up to $> 700 \mu\text{m}$. In

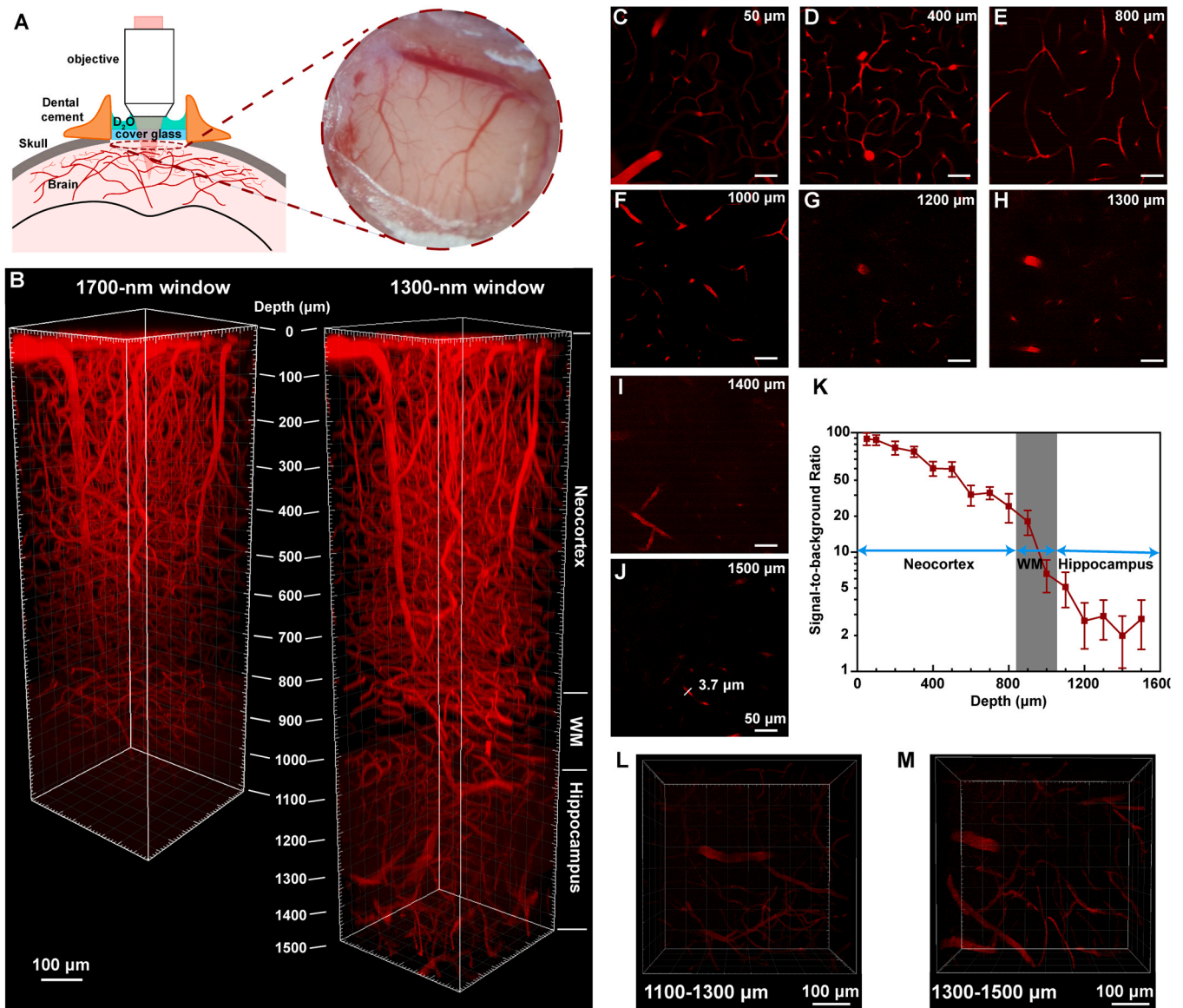


Fig. 3. *In vivo* deep 3PF brain vasculature imaging of the mouse with the open-skull glass window. (A) Schematic of mouse head imaging with the open-skull window. The bright field picture of mouse brain was shown at right position. (B) 3D reconstruction of the cerebrovascular imaging under 3PM excited using the 1700-nm window (0–1100 μm) and 1300-nm window (0–1500 μm). (C–J) 3PF imaging of the mouse brain vasculature at various depths excited in the 1300-nm window. (K) The SBR as a function of imaging depth. The white matter region of the mouse brain, where the SBR decreased sharply, is indicated in blue. (L–M) 3D reconstruction of the cerebrovascular imaging in 1100–1300 μm and 1300–1500 μm depth.

virtue of the red emission of DCBT NPs under 1300-nm three-photon excitation, multicolor fluorescence imaging was also carried out. The 3D reconstruction in Fig. 5L clearly displayed the merged image of the *Thy-1-GFP* neurons and DCBT NPs-labeled vessels from 0 to 600 μm . So far as we know, this is the first reported 3PF deep and simultaneous imaging of brain vessels and neurons under the intact skull.

Discussion and conclusion

We proposed a solution to the high scattering effect of both skull and brain tissue through the combination of SOC technique and 3PM, and therefore realized ultra-deep cerebrovascular and neuronal imaging under intact skull. While previous skull optical clearing agents were mainly applied in two-photon fluorescence microscopy, overlooking large light absorption by water at long excitation wavelength, the VNSOCA we prepared could efficiently reduce both scattering and absorption coefficients of skull during 3PM

process (Fig. 1). We also proposed a kind of AIE NPs named DCBT NPs with large σ_3 in the 1300-nm excitation window (Fig. 2). Meanwhile, we confirmed its great 3PF performance on the mouse brain imaging with an open-skull glass window, and achieved 1.5-mm imaging depth employing the 1300-nm excitation window, which was the largest one ever known (Fig. 3). Such imaging depth reached hippocampal region, and was almost comparable to the depth achieved by the 3PM excited in the 1700-nm window [40]. In addition, DCBT NPs assisted 3PM on the mouse's brain with intact skull combined with SOC technique enabled 1-mm cerebrovascular imaging depth (Fig. 4), which broke the through-skull 3PM depth record using the 1700-nm excitation window [43]. Finally, the 3PF through-skull imaging depth of neuron achieved over 700 μm . In addition, dual-channel deep imaging of both vessels and neurons under intact skull was also realized thanks to the reduced scattering of skull and brain tissue (Fig. 5).

The combination of the two techniques is quite reasonable. On the one hand, despite that 3PM alone could reduce the skull

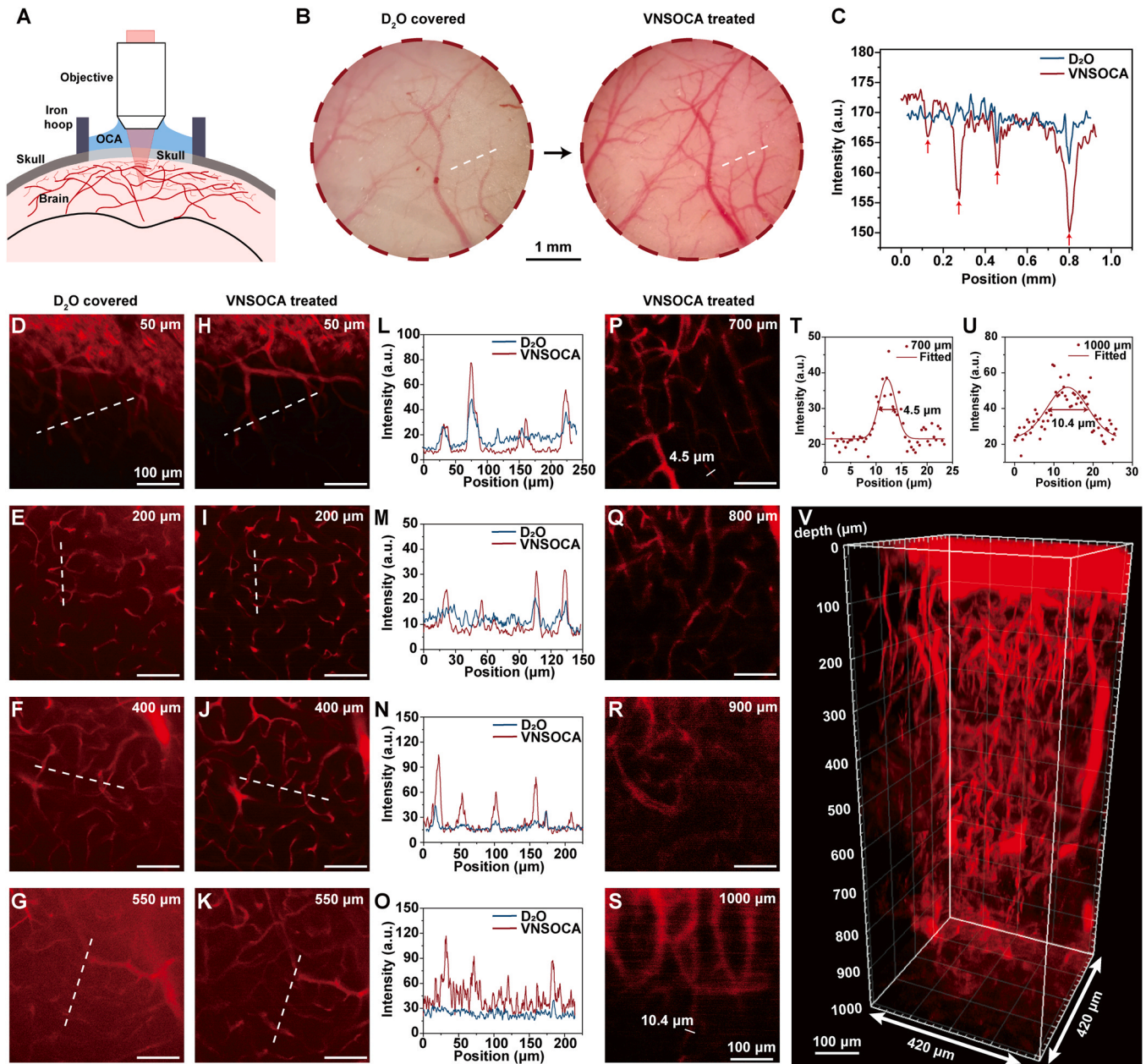


Fig. 4. *In vivo* deep 3PF brain vasculature imaging of the mouse with the optical clearing window. (A) Schematic of mouse head imaging with the optical clearing window. (B) Typical bright field pictures of the mouse brain vasculature before and after skull clearing. (C) Intensity profiles along the white dashed lines across the vasculature in (B). The arrows indicated the positions of vessels. (D–G) 3PF imaging of the mouse brain vasculature at various depths with original skull. (H–K) 3PF imaging of the mouse brain vasculature at various depths after skull clearing. (L–O) Intensity profiles along the white dashed lines across the brain vasculature in (D)–(K) respectively. (P–S) Deep 3PF images of the mouse brain vasculature after skull clearing. (T–U) FWHM analysis of the brain vasculature at the depths of 700 μm (T) and 1000 μm (U). (V) 3D reconstruction of the cerebrovascular imaging with the optical clearing window (0–1000 μm).

scattering effect to a certain extent, the efficiency is not enough owing to the extremely higher scattering of skull compared with the brain tissue [7]. Our previously reported 3PM on the mouse brain with intact skull reached only 400- μm depth in cerebrovascular structure imaging with excitation wavelength at 1550 nm. On the other hand, although *in vivo* skull SOC could overcome the skull scattering, itself was unable to conquer the scattering effect of brain tissue. For instance, 2PM through the optical skull clearing window only reached \sim 300- μm depth in the cortex [20]. Therefore, the combination of SOC technique and 3PM is a rather necessary solution to through-skull ultra-deep brain imaging. Accordingly, we realized 1000- μm 3PF cerebrovascular imaging and over 700 μm 3PF neuronal imaging of mouse brain with intact skull.

Even with the assistance of SOC technique and 1300-nm excited 3PM, ideal optical probes are still important for the final imaging performance. Although 3PM excited in the 1300-nm window has lower heating effect and higher excitation efficiency compared with that in the 1700-nm window, the stronger scattering in the 1300-nm window still constrained its imaging depth ever reported [36,44]. As a solution, we proposed a new kind of AIE NPs with extraordinarily large σ_3 at 1300 nm to improve the brightness of 3PF, and eventually achieved 1.5-mm 3PM depth with open-skull glass window, which was the deepest one in the 1300-nm window.

Since neuronal imaging is more important in monitoring brain function, we achieved three-photon through-skull neuronal imaging over 700 μm and dual-channel imaging of both vessels and neurons over 600 μm . This would be helpful for through-skull visualization of

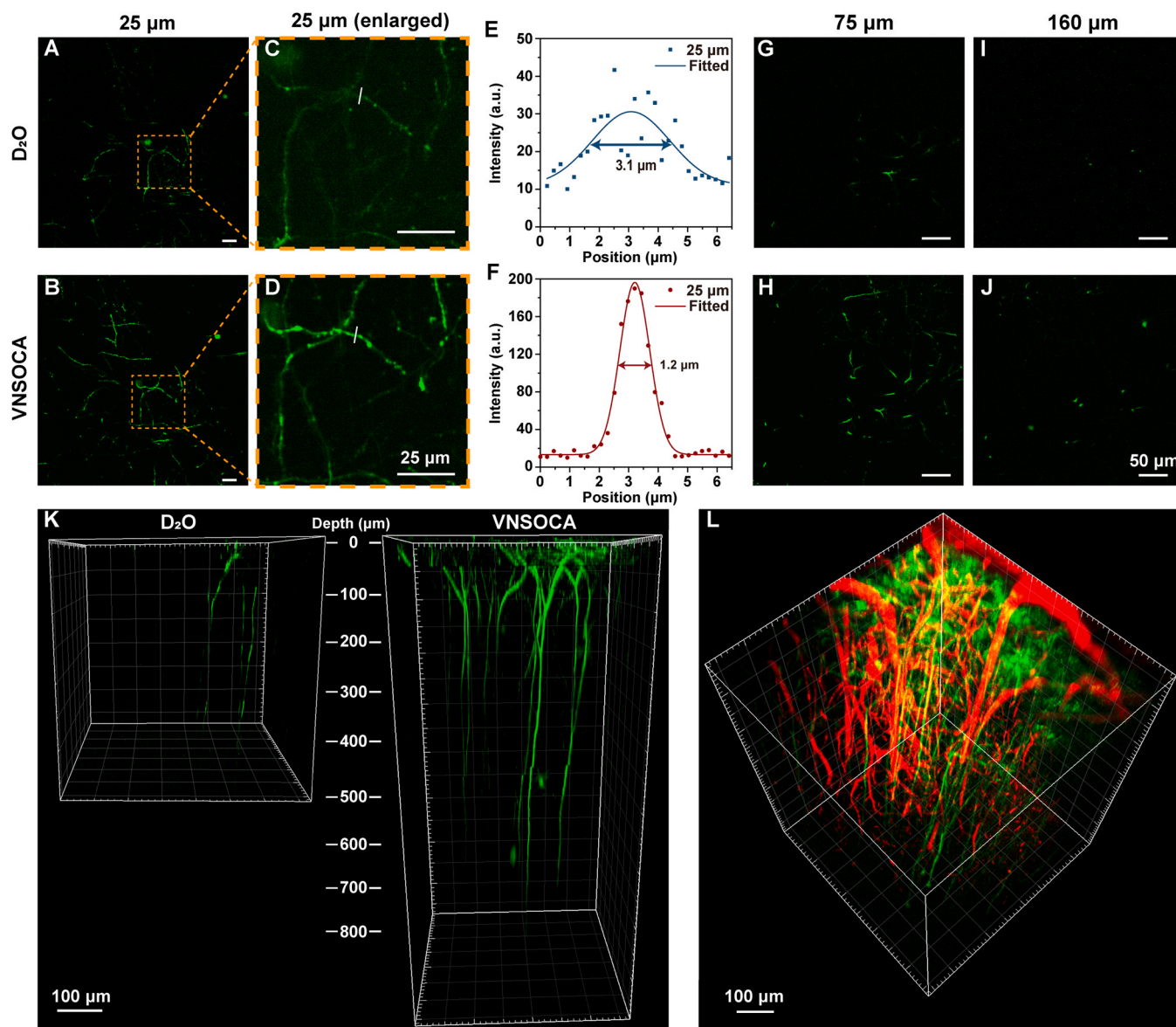


Fig. 5. *In vivo* deep 3PF brain neuron imaging and neuron-vessels dual channel imaging of the mouse with the optical clearing window. (A–B) 3PF images of the mouse brain neurons at 25- μm depth before and after skull clearing. (C–D) Enlarged 3PF images of the mouse brain neurons in (A) and (B). (E–F) Intensity and FWHM analysis of the brain neurons in (C) and (D). (G–J) 3PF images of the mouse brain neurons before and after skull clearing at depth of 75 μm and 160 μm . (K) 3D reconstruction of the 3PF neuronal imaging through the original skull (0–400 μm) and the skull optical clearing window (0–800 μm). (L) 3D reconstruction of the neuron-vessels dual channel imaging of the mouse with the optical clearing window (0–600 μm).

interaction between neuron and cerebral vessels at a large depth, and thus provide useful tool for monitoring brain disease such as epilepsy and stroke. Moreover, another possible way to imaging deeper neuron is to apply brighter foreign three-photon fluorescent probes to stain neurons. SNAP-tag is a very convenient technique for labeling specific cells [45–47]. Briefly, first, a specific kind of cells (such as nerve cells) is transfected with virus to express a specific protein. Then a specific marker for the protein is conjugated with the optical probe, making it able to selectively target the specific cells. Here, DCBT was encapsulated with F-127 polymer, which is lack of functional groups (e.g. NH_2 - and $-\text{COOH}$) for marker conjugation. The AIE molecules can also be doped into organic NPs by other polymers, such as DSPE-PEG- NH_2 and DSPE-PEG- COOH [48,49], which can be easily conjugated with the specific marker of the protein. Therefore, it is possible to use DCBT NPs for three-photon neuron imaging by the SNAP-tag technology in the future work.

The scattering reduction strategy presented here opens the opportunity for *in vivo* ultra-deep brain 3PM under the intact skull, where the imaging depth was nearly comparable with 3PM through the cranial window [50]. In addition, the 1300-nm excitation realized multi-color 3PM, making it possible for *in vivo* observation of molecular and cellular interactions in the brain under intact skull over a large depth in future. Moreover, the SOC procedure presented here is safe and easy-handling, not as difficult as craniotomy. Therefore, 3PM based on the skull optical clearing window can be widely used in various situations. We believe that *in vivo* 3PF imaging of hippocampus region under the intact skull of mouse brain will be realized with further reduced scattering effect of both brain tissue and skull, as well as improved 3PF probes. The combination of SOC technique and 3PM will contribute to faster and deeper imaging in scattering tissues including skull and brain.

Materials and methods

Materials

The details for DCBT synthesis were described in the [Supporting Information](#). Pluronic F-127 was bought from Sigma-Aldrich (USA). Deionized (DI) water with a resistivity of 16–18.2 M Ω cm was prepared an Eco-Q15 DI water system (Shanghai Hitech Instruments Co., Ltd.).

Preparation of DCBT NPs

DCBT NPs were prepared according to the standard procedure reported previously [51]. Briefly, 1 mg DCBT molecules and 12 mg Pluronic F-127, which were dissolved in 0.5 mL tetrahydrofuran (THF) respectively, were mixed together and sonicated for 9 min. Then, the mixture solution was dropped into 12 mL DI water. Afterwards, the residue THF was evaporated in the fume hood through stirring for 5 h. Finally, the DCBT NPs solution was concentrated in ultrafiltration tube.

Monte Carlo simulation of NIR photon penetration in skull and brain tissue

The Monte Carlo method was utilized to simulate the propagation of light beams in biological tissues. There are two layers of tissue in the simulation, representing the mouse skull and mouse brain tissue, respectively. We rasterized the tissue to record the scattering and absorption events of photons. In the simulation of focusing light in the tissue, photons enter the immersion media from the air, pass through the skull and focus on a specific depth in brain layer. The position of photon is randomly set within the beam radius. Meanwhile, the focal point was set at 1 mm depth in the skull and brain tissue after refracting in multiple tissue layers. Absorption matrix is formed to record absorbed energy of photons in tissue. The temperature profile of brain can be calculated by solving the thermal diffusion equation with absorption distribution. We set the refractive index of the skull and brain tissue as 1.369, and the scattering anisotropy factor as 0.98. The absorption coefficient of skull and brain tissue was set according to the water absorption coefficient in 1300 nm and 1700 nm. The reduced scattering coefficient of brain tissue was calculated using the following formula: [7] $\mu'_s = 24.2 \left(\frac{\lambda}{500\text{nm}}\right)^{-1.611}$. Thus, the brain tissue scattering coefficient in Fig. 1 was set as 5.192 cm⁻¹ in the 1300-nm window and 3.370 cm⁻¹ in the 1700-nm window respectively. The reduced scattering coefficient of skull was calculated using the following formula: [7] $\mu'_s = 22.9 \left(\frac{\lambda}{500\text{nm}}\right)^{-0.716}$. Accordingly, the remaining skull scattering coefficient in Fig. 1 was set as 11.554 cm⁻¹ (100%), 5.777 cm⁻¹ (50%), 3.466 cm⁻¹ (30%), 1.155 cm⁻¹ (10%), 0.116 cm⁻¹ (1%) in the 1300-nm window and 9.534 cm⁻¹ (100%), 4.767 cm⁻¹ (50%), 2.860 cm⁻¹ (30%), 0.953 cm⁻¹ (10%), 0.095 cm⁻¹ (1%) in the 1700-nm window respectively.

Preparation and vis-NIR-II absorption measurement of optical clearing agents

VNSOCA contain a saturated supernatant solution of urea and ethanol (named S1), and a high-concentration sodium dodecyl benzenesulfonate (named S2). To prepare S1, 75% (vol/vol) ethanol in deuterioxide solution was dropped onto the excessive urea and mixed together in a beaker. The mixture was stirred for 10 min and stayed for 15 min to dissolve urea fully. The synthesized S1 was then obtained after the supernatant solution was transferred. As to S2, the sodium dodecyl benzenesulfonate (mass = 5 g) and 0.7 M NaOH in deuterioxide solution (volume = 24 mL) were mixed together, under

the condition of 7.2–8 pH value. Finally, both S1 and S2 solution of VNSOCA were sealed and stored at room temperature. USOCA were prepared under the similar procedure, apart from deuterioxide replaced by deionized water. The absorption spectra of both VNSOCA and USOCA were measured from 500 to 1880 nm with two spectrophotometers (PG2000, Ideaoptics Instruments and NIR2200-Px, Ideaoptics Instruments).

3PF microscopic system

3PF microscopic system included two major parts, a non-collinear optical parametric amplifier (NOPA) with wavelength-tunable femtosecond (fs) laser output and a commercial Bruker scanning microscope. The NOPA system included a 1030 nm fs pump laser (Spectra-Physics, Spirit) and an OPA system (Spectra-Physics, NOPA-VISIR). 1300-nm fs laser beam (115 fs, 1 MHz) and 1700-nm fs laser beam (203 fs, 1 MHz) were obtained through two amplification stages in NOPA-VISIR and introduced into the scanning microscope as excitation source. The excitation beam was focused on the sample through the objective (XLPLN25XWMP2, Olympus, NA=1.05), and the excited three-photon fluorescent signals were then collected by a GaAs PMT (H7422-40, Hamamatsu), after reflected by a 700 nm DMLP and passing through a 560 nm DMLP. The filters for red channel and green channel were FF02-641/75 (Semrock) and FF02-525/40 (Semrock).

Optical Characterization of DCBT NPs

The absorption spectra and fluorescence spectra of DCBT NPs were measured on a UV-vis scanning spectrophotometer (UV-2550, Shimadzu, Japan) and a HITACHI F-2500 fluorescence spectrophotometer. The PL of DCBT NPs under 1300 nm fs excitation was carried out as following. The fs laser beam traveled through a focal lens (f= 30 mm) and was focused on a cuvette, which contained the dispersion of DCBT NPs. The 3PF signal was recorded with an optical fiber spectrometer (PG2000, Ideaoptics Instruments) through an objective (XLPLN25XWMP2, Olympus, NA= 1.05). The fluorescence quantum yield of DCBT NPs was measured via the comparative method with Rhodamine 6 G in DI water as reference. Details were described in our previous work [52].

P-I relationship measurement and σ_3 cross section measurement

The DCBT NPs were contained in the glass capillary and imaged under the 3PF microscopic system. The 3PF images under various excitation powers were recorded. The intensity of 3PF (I) vs the average power of 1300 nm fs laser (P) was plotted to determine the P-I relationship of DCBT NPs.

To obtain σ_3 of DCBT, the comparison method was applied. The σ_3 of TPATCN in CHCl₃ solution at 1550 nm [52] was selected as the reference. DCBT and TPATCN in CHCl₃ solution were excited by the 1550 nm fs laser, and their 3PF signals were collected by a photo-multiplier tube (PMT). The mean 3PF intensities were calculated by ImageJ. The σ_3 value of DCBT molecules was calculated by the following equation:

$$\sigma_{31} = \sigma_{30} \frac{F_1 \eta_0 c_0 n_0}{F_0 \eta_1 c_1 n_1} \quad (1)$$

Where F is the 3PF intensity, η is the fluorescence quantum yield, c is the molar concentration of sample, n is the refractive index of the solvent, and the subscripts 1 and 0 represent DCBT and TPATCN, respectively.

σ_3 of DCBT at other excitation wavelengths were referenced to the value at 1550 nm measured above and calculated by the following equation:

$$\sigma_{3,\lambda} = \sigma_{3,1550} \frac{P_{1550}^3 \tau_{\lambda}^2 F_{\lambda}}{P_{\lambda}^3 \tau_{1550}^2 F_{1550}} \left(\frac{\lambda}{1550}\right)^2 \quad (2)$$

Where $\sigma_{3,\lambda}$ is the wavelength dependent three-photon absorption cross section, $\sigma_{3,1550}$ is σ_3 of DCBT at 1550 nm, P_{1550} and P_{λ} are the measured excitation powers on the sample, τ_{1550} and τ_{λ} are the measured pulse widths on the sample, and F_{1550} and F_{λ} are the measured 3PF intensities with excitation at 1550 nm and other wavelengths, respectively.

Ethical approval

All animal experiments performed in this study were conducted strictly in compliance with the ethical standards of the Institutional Ethical Committee of Animal Experimentation of Zhejiang University.

In vivo 3PF microscopic cerebrovascular imaging of the mouse with the cranial window

The C57 mouse (male, 8–10 weeks old) was anesthetized by pentobarbital sodium (0.14 mL, mass concentration = 1%), and a cranial window with diameter of around 6 mm was produced by removing the scalp and a small piece of skull. After injected with DCBT NPs (1.5 mg/mL, 200 μ L) via the tail vein, the mouse was immobilized on a lab-built plate and imaged under the 3PF microscopic system. The z-stack images were taken at 2- μ m step and the scanning speed was 2.2 μ s/pixel (512 \times 512 pixels per frame).

In vivo 3PF microscopic brain imaging of the mouse with intact skull

Animal preparations with intact skull window and optical clearing window followed standard surgery reported previously [53]. The Balb/c mice (male, ~6 weeks old) with intact skull window were injected with DCBT NPs (1.5 mg/mL, 200 μ L) through tail vein. Through-skull imaging was then carried out on the 3PF microscopic system. To evaluate the improved effects of imaging depth as well as imaging quality of 3PF microscopic cerebrovascular imaging through the established vis-NIR-II skull optical clearing window, the skull window was treated with S1 and S2 of VNSOCA to get skull optical clearing window. After that, imaging of the same field of view was conducted on the 3PF microscopic system. *Thy-1-GFP-M-line* male mice (~6 weeks old) were treated by the operation mentioned above to obtain the skull optical clearing window. And 3PF neuronal imaging and dual-channel cerebrovascular and neuronal imaging were carried out under the same 3PF microscopic system.

Data analysis

Image J software (Version 1.6.0, National Institutes of Health, USA) was applied for quantitative analysis of each fluorescent image. Origin Pro software (Version 9.0, OriginLab Company, USA), Imaris (Version 9.0, Oxford Instruments) and Adobe Illustrator CC (Version 2018) was applied for graph generation.

CRediT authorship contribution statement

Mubin He: Conceptualization, Data curation, Investigation, Methodology, Software Writing – original draft. **Dongyu Li:** Data curation, Software, Writing – review & editing. **Zheng Zheng:** Funding acquisition, Data curation, Investigation, Writing – review & editing. **Hequn Zhang:** Data curation, Investigation, Methodology. **Tianxiang Wu:** Investigation, Methodology, Software. **Weihang Geng:** Investigation, Methodology. **Zhengwu Hu:** Data curation, Software. **Zhe Feng:** Data curation, Methodology. **Shiyi Peng:** Investigation, Writing – review & editing. **Liang Zhu:** Data curation,

Software. **Wang Xi:** Conceptualization, Supervision. **Dan Zhu:** Conceptualization, Supervision. **Ben Zhong Tang:** Conceptualization, Supervision, Writing – review & editing. **Jun Qian:** Conceptualization, Funding acquisition, Supervision, Writing – review & editing. All the authors have approved the revised manuscript.

Declaration of Competing Interest

The authors declare that they have no known competing financial interests or personal relationships that could have appeared to influence the work reported in this paper.

Acknowledgements

This work was supported by National Natural Science Foundation of China (61975172, 82001874, 61735016, 81870934, 82001877 and 22105057), and the Innovation Project of Optics Valley Laboratory (Grant No. OVL2021BG011).

Appendix A. Supporting information

Supplementary data associated with this article can be found in the online version at doi:10.1016/j.nantod.2022.101536.

References

- [1] Z.Q. Zhang, W. Liao, H.F. Chen, D. Mantini, J.R. Ding, Q. Xu, Z.G. Wang, C.P. Yuan, G.H. Chen, Q. Jiao, G.M. Lu, BRAIN 134 (2011) 2912–2928, <https://doi.org/10.1093/brain/awr223>
- [2] Y. Stern, E.M. Arenaza-Urquijo, D. Bartres-Faz, S. Belleville, M. Cantlon, G. Chetelat, M. Ewers, N. Franzmeier, G. Kempermann, W.S. Kremen, O. Okonkwo, N. Scarmeas, A. Soldan, C. Udeh-Momoh, M. Valenzuela, P. Vemuri, E. Vuoksimaa, F. Reserve Resilience Protective, ALZHEIMERS Dement. 16 (2020) 1305–1311, <https://doi.org/10.1016/j.jalz.2018.07.219>
- [3] A. Alexander-Bloch, J.N. Giedd, E.T. Bullmore, Nat. Rev. Neurosci. 14 (2013) 322–336, <https://doi.org/10.1038/nrn3465>
- [4] E.M. Reiman, Y.T. Quiroz, A.S. Fleisher, K.W. Chen, C. Velez-Pardo, M. Jimenez-Del-Rio, A.M. Fagan, A.R. Shah, S. Alvarez, A. Arbelaez, M. Giraldo, N. Acosta-Baena, R.A. Sperling, B. Dickerson, C.E. Stern, V. Tirado, C. Munoz, R.A. Reiman, M.J. Huentelman, G.E. Alexander, J.B.S. Langbaum, K.S. Kosik, P.N. Tariot, F. Lopera, LANCET Neurol. 11 (2012) 1048–1056, [https://doi.org/10.1016/S1474-4422\(12\)70228-4](https://doi.org/10.1016/S1474-4422(12)70228-4)
- [5] A. Horn, M. Reich, J. Vorwerk, N.F. Li, G. Wenzel, Q.Q. Fang, T. Schmitz-Hubsch, R. Nickl, A. Kupsch, J. Volkmann, A.A. Kuhn, M.D. Fox, Ann. Neurol. 82 (2017) 67–78, <https://doi.org/10.1002/ana.24974>
- [6] G. Orru, W. Petterson-Yeo, A.F. Marquand, G. Sartori, A. Mechelli, Neurosci. Biobehav. Rev. 36 (2012) 1140–1152, <https://doi.org/10.1016/j.neubiorev.2012.01.004>
- [7] S.L. Jacques, Phys. Med. Biol. 58 (2013) 5007–5008, <https://doi.org/10.1088/0031-9155/58/14/5007>
- [8] J. Xia, J.J. Yao, L.V. Wang, Prog. Electromagn. Res.-PIER 147 (2014) 1–22, <https://doi.org/10.2528/PIER14032303>
- [9] A.B.E. Attia, G. Balasundaram, M. Moothanchery, U.S. Dinish, R.Z. Bi, V. Ntziachristos, M. Olivo, PHOTOACOUSTICS 16 (2019), <https://doi.org/10.1016/j.pacs.2019.100144>
- [10] L.M. Nie, X.Y. Chen, Chem. Soc. Rev. 43 (2014) 7132–7170, <https://doi.org/10.1039/c4cs00086b>
- [11] J. Ouyang, L.H. Sun, F. Zeng, S.Z. Wu, Coord. Chem. Rev. 458 (2022), <https://doi.org/10.1016/j.ccr.2022.214438>
- [12] L.Q. Chen, J.J. Chen, Y.C. Fang, F. Zeng, S.Z. Wu, Chem. Commun. 57 (2021) 7842–7845, <https://doi.org/10.1039/d1cc02845f>
- [13] Z.M. Shang, Z.H. Ding, L. Wang, Y. Liu, Path length coded coherence combination for three-dimensional superresolution, ACTA Phys. Sin. 60 (2011), <https://doi.org/10.7498/aps.60.124204>
- [14] T. Han, J.R. Qiu, D. Wang, J. Meng, Z.Y. Liu, Z.H. Ding, Chin. J. Lasers-zhongguo Jiguang 47 (2020), <https://doi.org/10.3788/cj1202047.0207004>
- [15] P. Chen, L. Jiang, H. Wang, H. Sun, Y. Zhang, R. Liang, Acta Photon. Sin. 48 (2019), <https://doi.org/10.3788/gzxb20194806.0611001>
- [16] A. Holtmaat, T. Bonhoeffer, D.K. Chow, J. Chuckowree, V. De Paola, S.B. Hofer, M. Hubener, T. Keck, G. Knott, W.C. Lee, R. Mostany, T.D. Mrsic-Flogel, E. Nedivi, C. Portera-Cailliau, K. Svoboda, J.T. Trachtenberg, L. Wilbrecht, Nat. Protoc. 4 (2009) 1128–1144, <https://doi.org/10.1038/nprot.2009.89>
- [17] G. Yang, F. Pan, C.N. Parkhurst, J. Grutzendler, W.B. Gan, Nat. Protoc. 5 (2010) 201–208, <https://doi.org/10.1038/nprot.2009.222>
- [18] X. Yu, Y. Zuo, J. Vis. Exp. (2014) 51520, <https://doi.org/10.3791/51520>
- [19] C. Zhang, W. Feng, Y. Zhao, T. Yu, P. Li, T. Xu, Q. Luo, D. Zhu, Theranostics 8 (2018) 2696–2708, <https://doi.org/10.7150/thno.23686>

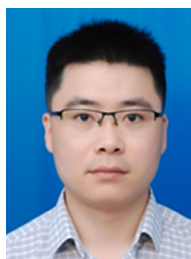
- [21] Y.J. Zhao, T.T. Yu, C. Zhang, Z. Li, Q.M. Luo, T.H. Xu, D. Zhu, *Light Sci. Appl.* 7 (2018) 17153, <https://doi.org/10.1038/lssa.2017.153>
- [22] H.-T. Xu, F. Pan, G. Yang, W.-B. Gan, *Nat. Neurosci.* 10 (2007) 549–551, <https://doi.org/10.1038/nrn1883>
- [23] T. Wang, C. Xu, *Optica* 7 (2020) 947–960, <https://doi.org/10.1364/optica.395825>
- [24] N.G. Horton, K. Wang, D. Kobat, C.G. Clark, F.W. Wise, C.B. Schaffer, C. Xu, *Nat. Photonics* 7 (2013) 205–209, <https://doi.org/10.1038/nphoton.2012.336>
- [25] M. Wang, C. Wu, B. Li, F. Xia, D. Sinefeld, C. Xu, Comparison of excitation wavelengths for in vivo deep imaging of mouse brain, *Proc.SPIE* 10498 (2018), <https://doi.org/10.1117/12.2289065> SPIE2018.
- [26] D.G. Ouzounov, T. Wang, M. Wang, D.D. Feng, N.G. Horton, J.C. Cruz-Hernández, Y.-T. Cheng, J. Reimer, A.S. Tolias, N. Nishimura, C. Xu, *Nat. Methods* 14 (2017) 388–390, <https://doi.org/10.1038/nmeth.4183>
- [27] T. Wang, D.G. Ouzounov, C. Wu, N.G. Horton, B. Zhang, C.-H. Wu, Y. Zhang, M.J. Schnitzer, C. Xu, *Nat. Methods* 15 (2018) 789–792, <https://doi.org/10.1038/s41592-018-0115-y>
- [28] Y. Hontani, F. Xia, C. Xu, *Sci. Adv.* 7 (2021) eabf3531, <https://doi.org/10.1126/sciadv.abf3531>
- [29] J. Luo, Z. Xie, J.W. Lam, L. Cheng, H. Chen, C. Qiu, H.S. Kwok, X. Zhan, Y. Liu, D. Zhu, B.Z. Tang, *Chem. Commun. (Camb.)*, (2001) 1740–1741, <https://doi.org/10.1039/b105159h>
- [30] W. Xu, D. Wang, B.Z. Tang, *Angew. Chem. Int. Ed.* (2020), <https://doi.org/10.1002/anie.202005899>
- [31] Y. Wang, M. Chen, N. Alifu, S. Li, W. Qin, A. Qin, B.Z. Tang, J. Qian, *ACS Nano* 11 (2017) 10452–10461, <https://doi.org/10.1021/acsnano.7b05645>
- [32] K. Li, W. Qin, D. Ding, N. Tomczak, J. Geng, R. Liu, J. Liu, X. Zhang, H. Liu, B. Liu, B.Z. Tang, *Sci. Rep.* 3 (2013) 1150, <https://doi.org/10.1038/srep01150>
- [33] Z. Zheng, D. Li, Z. Liu, H.Q. Peng, H.H.Y. Sung, R.T.K. Kwok, I.D. Williams, J.W.Y. Lam, J. Qian, B.Z. Tang, *Adv. Mater.* 31 (2019) e1904799, <https://doi.org/10.1002/adma.201904799>
- [34] N. Alifu, A. Zebibula, H. Zhang, H. Ni, L. Zhu, W. Xi, Y. Wang, X. Zhang, C. Wu, J. Qian, *Nano Res.* 13 (2020) 2632–2640, <https://doi.org/10.1007/s12274-020-2902-x>
- [35] W. Qin, N. Alifu, J.W.Y. Lam, Y. Cui, H. Su, G. Liang, J. Qian, B.Z. Tang, *Adv. Mater.* 32 (2020) e2000364, <https://doi.org/10.1002/adma.202000364>
- [36] D. Li, H. Zhang, L.L. Streich, Y. Wang, P. Lu, L. Wang, R. Prevedel, J. Qian, *Mater. Chem. Front.* 5 (2021) 3201–3208, <https://doi.org/10.1039/d1qm00243k>
- [37] Y. Wang, W. Wen, K. Wang, P. Zhai, P. Qiu, K. Wang, *Appl. Phys. Lett.* 108 (2016) 021112, <https://doi.org/10.1063/1.4939970>
- [38] L.-C. Cheng, N.G. Horton, K. Wang, S.-J. Chen, C. Xu, *Biomed. Opt. Express* 5 (2014) 3427–3433, <https://doi.org/10.1364/BOE.5.003427>
- [39] H. Liu, X. Deng, S. Tong, C. He, H. Cheng, Z. Zhuang, M. Gan, J. Li, W. Xie, P. Qiu, K. Wang, *Nano Lett.* 19 (2019) 5260–5265, <https://doi.org/10.1021/acs.nanolett.9b01708>
- [40] M. Liu, B. Gu, W. Wu, Y. Duan, H. Liu, X. Deng, M. Fan, X. Wang, X. Wei, K.-T. Yong, K. Wang, G. Xu, B. Liu, *Chem. Mater.* 32 (2020) 6437–6443, <https://doi.org/10.1021/acs.chemmater.0c01577>
- [41] L. Streich, J.C. Boffi, L. Wang, K. Alhalaseh, M. Barbieri, R. Rehm, S. Deivasigamani, C.T. Gross, A. Agarwal, R. Prevedel, *Nat. Methods* (2021), <https://doi.org/10.1038/s41592-021-01257-6>
- [42] F. Xia, M. Gevers, A. Fognini, A.T. Mok, B. Li, N. Akbari, I.E. Zadeh, J. Qin-Dregely, C. Xu, *ACS Photonics* 8 (2021) 2800–2810, <https://doi.org/10.1021/acsp Photonics.1c01018>
- [43] Y. Chen, S. Liu, H. Liu, S. Tong, H. Tang, C. Zhang, S. Yan, H. Li, G. Yang, D. Zhu, K. Wang, P. Wang, *Anal. Chem.* 91 (2019) 9371–9375, <https://doi.org/10.1021/acs.analchem.9b02624>
- [44] Z.-L. Qiu, M.-b He, K.-S. Chu, C. Tang, X.-W. Chen, L. Zhu, L.-P. Zhang, D. Sun, J. Qian, Y.-Z. Tan, *Adv. Opt. Mater.* 9 (2021) 2100482, <https://doi.org/10.1002/adom.202100482>
- [45] R. Merlo, D. Caprioglio, M. Cillo, A. Valenti, R. Mattossovich, G. Morrone, A. Massarotti, F. Rossi, R. Miggiano, A. Leonardi, A. Minassi, G. Peruginio, *J. Enzym. Inhib. Med. Chem.* 36 (2021) 85–97, <https://doi.org/10.1080/14756366.2020.1841182>
- [46] X. Sun, A. Zhang, B. Baker, L. Sun, A. Howard, J. Buswell, D. Maurel, A. Masharina, K. Johnsson, C.J. Noren, M.-Q. Xu, I.R. Corrêa Jr, *ChemBioChem* 12 (2011) 2217–2226, <https://doi.org/10.1002/cbic.201100173>
- [47] D. Srikun, A.E. Albers, C.I. Nam, A.T. Iavarone, C.J. Chang, *J. Am. Chem. Soc.* 132 (2010) 4455–4465, <https://doi.org/10.1021/ja100117u>
- [48] X. Fan, Y. Li, Z. Feng, G. Chen, J. Zhou, M. He, L. Wu, S. Li, J. Qian, H. Lin, *Adv. Sci.* (2021), <https://doi.org/10.1002/adv.202003972>
- [49] Y. Yang, X. Fan, L. Li, Y. Yang, A. Nuernisha, D. Xue, C. He, J. Qian, Q. Hu, H. Chen, J. Liu, W. Huang, *ACS Nano* 14 (2020) 2509–2521, <https://doi.org/10.1021/acsnano.0c00043>
- [50] S. Wang, X. Li, S.Y. Chong, X. Wang, H. Chen, C. Chen, L.G. Ng, J.W. Wang, B. Liu, *Adv. Mater.* (2021) e2007490, <https://doi.org/10.1002/adma.202007490>
- [51] Z. Zheng, H. Zhang, H. Cao, J. Gong, M. He, X. Gou, T. Yang, P. Wei, J. Qian, W. Xi, B.Z. Tang, *ACS Nano* 16 (2022) 6444–6454, <https://doi.org/10.1021/acsnano.2c00672>
- [52] Y. Wang, X. Han, W. Xi, J. Li, A.W. Roe, P. Lu, J. Qian, *Adv. Healthc. Mater.* 6 (2017), <https://doi.org/10.1002/adhm.201700685>
- [53] D.Y. Li, Z. Zheng, T.T. Yu, B.Z. Tang, P. Fei, J. Qian, D. Zhu, *J. Biophotonics* 13 (2020) e202000142, <https://doi.org/10.1002/jbio.202000142>



Mubin He is a Ph.D. candidate student of the College of Optical Science and Engineering of Zhejiang University. He received his bachelor's degree from the College of Biosystems Engineering and Food Science of Zhejiang University in 2018. His current research fields lie in multi-photon bioimaging.



Dongyu Li received his Ph.D. degree from the College of Optical Science and Engineering of Zhejiang University in 2019. He is now a postdoctor in the Wuhan National Laboratory for Optoelectronics, Huazhong University of Science and Technology. His research work focuses on Biomedical Photonics. He is the first author or corresponding author of 13 peer-reviewed SCI papers.



Zheng Zheng received his Ph.D. degree from École Normale Supérieure de Lyon in 2016. He then conducted postdoctoral research under the supervision of Prof. Ben Zhong Tang at The Hong Kong University of Science & Technology in 2016–2020. He is now a professor in School of Chemistry and Chemical Engineering, Hefei University of Technology. His research focuses on the development of new functional organic fluorophores and exploration of their biological applications.



Professor Ben Zhong Tang received his BS and Ph.D. degrees from South China University of Technology and Kyoto University in 1982 and 1988, respectively. He then conducted his postdoctoral work at the University of Toronto. He joined the Hong Kong University of Science & Technology in 1994 and was promoted to Chair Professor in 2008. In 2021, he joined CUHK-Shenzhen as Dean of the School of Science and Engineering. His research interests include the exploration of new advanced materials, new luminescent processes, and new polymerization reactions. He is now serving as Editor-in-Chief of *Aggregate* published by Wiley.



Jun Qian received his Ph.D. degree from the Department of Optical Engineering of Zhejiang University in 2009. He is now a professor in the College of Optical Science and Engineering, Zhejiang University. His research work focuses on Biomedical-Photonics. He is the first author or corresponding author of more than 80 peer-reviewed SCI papers. He has given plenary/invited talks in international/domestic conferences for over 40 times.

Lipid droplets imaging with three-photon microscopy

Mubin He^{*,††}, Hojeong Park^{†,††}, Guangle Niu[‡], Qiming Xia[§], Hequn Zhang^{*},
Ben Zhong Tang^{¶,||} and Jun Qian^{**,**}

**State Key Laboratory of Modern Optical Instrumentations
Centre for Optical and Electromagnetic Research
College of Optical Science and Engineering
International Research Center for Advanced Photonics
Zhejiang University, Hangzhou 310058, P. R. China*

*†Department of Chemistry, The Hong Kong Branch of Chinese
National Engineering Research Center for Tissue Restoration and Reconstruction
The Hong Kong University of Science and Technology
Clear Water Bay, Kowloon, Hong Kong 999077, P. R. China*

*‡Shenzhen Research Institute of Shandong University
Shenzhen 518057, P. R. China*

*§Department of General Surgery, Sir Run Run Shaw Hospital
School of Medicine, Zhejiang University
Hangzhou 310000, P. R. China*

*¶School of Science and Engineering
Shenzhen Institute of Aggregate Science and Technology
The Chinese University of Hong Kong
Shenzhen, Guangdong 518172, P. R. China*

||tangbenz@cuhk.edu.cn

***qianjun@zju.edu.cn*

Received 21 May 2022
Accepted 1 August 2022
Published 14 October 2022

Lipid droplets (LDs) participate in many physiological processes, the abnormality of which will cause chronic diseases and pathologies such as diabetes and obesity. It is crucial to monitor the distribution of LDs at high spatial resolution and large depth. Herein, we carried three-photon imaging of LDs in fat liver. Owing to the large three-photon absorption cross-section of the luminogen named NAP-CF₃ ($1.67 \times 10^{-79} \text{ cm}^6 \text{ s}^2$), three-photon fluorescence fat liver imaging

^{||,**}Corresponding authors.

^{††}Mubin He and Hojeong Park contributed equally to this paper.

This is an Open Access article. It is distributed under the terms of the Creative Commons Attribution 4.0 (CC-BY) License. Further distribution of this work is permitted, provided the original work is properly cited.

reached the largest depth of 80 μm . Fat liver diagnosis was successfully carried out with excellent performance, providing great potential for LDs-associated pathologies research.

Keywords: Lipid droplets; three-photon fluorescence microscopy; fat liver, deep-tissue imaging.

1. Introduction

Lipid droplets (LDs) are intracellular organelles for storing neutral lipids, including triglycerides and cholesterol esters, which are widely present in adipocytes, hepatocytes, and the adrenal cortex.¹ LDs are involved in many physiological processes, including membrane synthesis and trafficking,² inflammation,³ and protein degradation,⁴ and are associated with chronic diseases pathologies such as diabetes, obesity, atherosclerosis, and viral replication.⁵ Thus, it is critically important to image LDs for localization and analysis in biomedical research and clinical diagnosis.

Optical imaging is preferred for the location and analysis of LDs due to its high spatial resolution, real-time performance, and specifically staining ability. Many optical imaging technologies have been applied to LDs imaging, including confocal laser scanning microscopy (CLSM),^{6–9} Raman microscopy,¹⁰ and multi-photon microscopy.^{11–17} CLSM enables high spatial-resolution performance of LD imaging, while super-resolution microscopy including stimulated emission depletion (STED) and structured illumination microscopy (SIM), further improves the spatial resolution of LDs' imaging.^{11,18,19} However, they were constrained within shallow imaging depth due to large scattering effect of short wavelength. As a solution, multi-photon microscopy is an effective way to improve penetration depth owing to its long-wavelength excitation and nonlinear confinement. Two-photon microscopy (2PM) to LDs has been successfully used in cells, mouse tissues, and living zebrafish with good performance.^{13,15–17} Moreover, three-photon microscopy (3PM) holds an even larger penetration depth than 2PM, maintaining high contrast in turbid tissue including mouse brain^{20–24} and liver.²⁵ However, few three-photon fluorescence imaging of LDs were reported,²⁵ where the imaging depth as well as resolution could be further improved.

In this study, we employed a luminogen named NAP-CF₃ with enhanced fluorescence in oleic acid (OA) for LDs imaging in fatty liver through confocal and three-photon microscopy. Moreover,

three-photon fluorescence imaging of LDs in the fatty liver was conducted and reached the largest depth ever reported,^{13,24} which would be significant for fatty liver diagnosis and obesity research. The primary objective of this study was to improve the imaging depth of LDs at the tissue level.

2. Methods

2.1. Materials

Chemicals and reagents were purchased from qualified chemical sources. NAP-CF₃ was synthesized according to a previously published literature.²⁶ OA was bought from Sigma-Aldrich (USA). The mouse (C57BL/6JGpt DIO) was purchased from Gem Pharmatech Company.

2.2. Characterization of NAP-CF₃

The synthetic process of NAP-CF₃ was referred to our previous work.²⁶ The absorption spectra of NAP-CF₃ were recorded by a UV-vis-NIR scanning spectrophotometer (UV-2550, Shimadzu, Japan), while photoluminescence spectra of the NAP-CF₃ were measured by a HITACHI F-2500 fluorescence spectrophotometer with an excitation wavelength of 405 nm. To measure the fluorescence of the NAP-CF₃ mixture in OA, the same concentration of NAP-CF₃ in dimethyl sulfoxide (DMSO) and OA was illuminated by a Xenon lamp at 405 nm.

2.3. Confocal imaging

Confocal fluorescence imaging was conducted on a Zeiss LSM 800 laser confocal microscope. HeLa cells were cultured in standard 5%CO₂/air 37°C environments. NAP-CF₃ (50 nM) and Nile Red (100 nM) were both dispersed in Dulbecco's modified eagle medium (DMEM). HeLa cells were further incubated with these compounds. After incubation, the cells were washed three times with phosphate-buffered saline (PBS, pH = 7.4). To obtain co-stain imaging, NAP-CF₃ was excited by 405-nm laser and

we collected the fluorescence in the 400–500 nm range, while Nile Red was excited by 488 nm laser and its fluorescence was collected in 540–700 nm range.

2.4. Guinea pig tissue preparation

The high-fat fed and normal guinea pig tissue samples were obtained from the Experimental Animal Center of Guangzhou University of Chinese Medicine (SYXK (Yue) 2018-0085). 30 Male Hartley guinea pigs were obtained from the Guangdong Experimental Animal Center. The living condition of guinea pigs were at constant temperature (20–25°C) and 65–70% humidity with a 12-h light/dark cycle in independent ventilation cage. After one week of adaptive feeding, all guinea pigs were randomly divided into control group (5 guinea pigs) and experimental group (25 guinea pigs). The control group was under normal diet whereas the experimental group was under high-fat diet. The guinea pigs were anesthetized with 10% chloral hydrate (0.3 mL/100 g), and the whole livers were taken every week for five weeks.

The frozen liver tissue was embedded with optical cutting temperature (OCT) agent in a cryostat (Thermo Scientific, USA) and sectioned with the thickness of 10 μm . Tissue samples were stained with the culture medium containing 1 μM of NAP-CF₃ in 5% CO₂/air humidified incubator at 37°C for 1 h. The tissues were washed three times with PBS (pH = 7.4) prior to imaging. Fluorescent images were obtained on Zeiss LSM 800 confocal scanning microscope (excitation = 405 nm and emission collection = 480–560 nm for NAP-CF₃).

2.5. Three-photon fluorescence characterization of NAP-CF₃

The glass capillaries contained NAP-CF₃ in DMSO, and OA were imaged under a 3PF microscopy. The 3PF images were recorded under different excitation powers to get the P-I relationship of NAP-CF₃.

The comparison method was applied to measure σ_3 of NAP-CF₃ according to our previous work.²⁷ Fluorescein in saline solution at 1300 nm was selected as the reference.²⁸ NAP-CF₃ in DMSO and fluorescein in saline solution were excited by the 1300 nm fs laser, and their 3PF signals were

collected by a photomultiplier tube (PMT). The mean 3PF intensities were calculated by ImageJ. The σ_3 value of NAP-CF₃ was calculated by the following equation:

$$\sigma_{3_1} = \sigma_{3_0} \frac{F_1 \eta_0 c_0 n_0}{F_0 \eta_1 c_1 n_1}, \quad (1)$$

where F is the 3PF intensity, η is the fluorescence quantum yield, c is the molar concentration of sample, n is the refractive index of the solvent, and the subscripts 1 and 0 represent NAP-CF₃ and fluorescein, respectively.

σ_3 of NAP-CF₃ at other excitation wavelengths were referenced to the value at 1300 nm measured above and calculated by the following equation:

$$\sigma_{3,\lambda} = \sigma_{3,1300} \frac{P_{1300}^3 \tau_\lambda^2 F_\lambda}{P_\lambda^3 \tau_{1300}^2 F_{1300}} \left(\frac{\lambda}{1300} \right)^3, \quad (2)$$

where $\sigma_{3,\lambda}$ is the wavelength dependent three-photon absorption cross-section, $\sigma_{3,1300}$ is σ_3 of NAP-CF₃ at 1300 nm, P_{1300} and P_λ are the time-averaged excitation photon flux (photons/s) on the sample, τ_{1300} and τ_λ are the measured pulse widths on the sample, and F_{1300} and F_λ are the measured 3PF intensities with excitation at 1300 nm and other wavelengths, respectively.

The 3PF photostability of NAP-CF₃ was tested as following. 0.1 mg/mL NAP-CF₃ in OA was contained in a tube capillary and imaged for 24 min continuously under the 1300-nm-fs excitation (average power: 10 mW). The fluorescence intensity was taken from the average intensity of the pixel counts on tube capillary in the field of view (Zoom = 1). Dwell time = 2.2 μs /pixel; field of view: 480 \times 480 μm ; frame rate: 4 frame/slice.

2.6. Three-photon fluorescence imaging of mice liver tissue

The adult model mouse (C57BL/6JGpt DIO) was sacrificed to obtain the fresh mice liver tissues. Immediately, the tissues were incubated with NAP-CF₃ (100 nM) at room temperature in culture medium (DMEM) for 2 h. Afterwards, the tissues were washed with PBS (pH = 7.4) before three-photon fluorescence imaging. The 3PM used a non-collinear optical parametric amplifier (NOPA) with wavelength-tunable femtosecond (fs) laser output and a commercial Bruker scanning microscope. The

NOPA part consisted of a 1030-nm fs pump laser (Spectra-Physics, Spirit) and an optical parametric amplifier system (Spectra-Physics, NOPA-VISIR). 1300-nm fs laser beam was selected as the excitation source and a 60X oil objective (Filling factor = 1; effective NA = 1.35, UPlanSApo60X, Olympus) was applied for high-magnified fluorescence imaging. The full width at half maximum of 1300-nm fs laser beam was measured as 115 fs after the objective. Laser power before objective: 15 mW for 0–30 μm imaging, 30 mW for 31–45 μm imaging, 60 mW for 46–60 μm imaging, and 90 mW for 61–80 μm imaging. The experiments above were performed in compliance with the ethical standards of the Institutional Ethical Committee of Animal Experimentation of Zhejiang University (ZJU-IACUC: ZJU20210222).

3. Results and Discussions

The structure of NAP-CF₃ is shown in Fig. 1(a). The normalized extinction and FL spectra of NAP-CF₃ have been demonstrated in our previous work.²⁶ We first testified the fluorescent enhancement of NAP-CF₃ when bound to LDs. Figure 1(a) showed the extinction spectra of NAP-CF₃ in DMSO and OA. NAP-CF₃ showed an absorption peak at around 420 nm both in DMSO and OA. There is little difference in the extinction spectral shape. However, the fluorescence of NAP-CF₃ in OA showed a strongly enhanced intensity compared with that of NAP-CF₃ in DMSO [Fig. 1(b)]. The

blue-shifted and enhanced fluorescence of NAP-CF₃ in OA is attributed to the nonpolar character of OA and solvatochromic property of NAP-CF₃.

With enhanced emission in OA, NAP-CF₃ could possibly target to LDs specifically, since the viscosity inside LD is very high. Our previous work have confirmed a high clog P value of NAP-CF₃.²⁶ Therefore, NAP-CF₃-labeled LDs possibly have extremely high contrast in imaging.²⁶ To illustrate it, we performed the co-staining LD imaging with commercially available LD-labeled probe, Nile Red (Fig. 2). As shown in Figs. 2(a) and 2(b), LDs were clearly stained with NAP-CF₃ and Nile Red. The merged imaging in Fig. 2(c) demonstrated that the fluorescence of NAP-CF₃ and Nile Red were overlapped well, confirming the high staining specificity of NAP-CF₃ to LDs. The enlarged images in Figs. 2(d)–2(f) showed LDs with high spatial resolution. In Fig. 2(d), other parts which were out of LDs emitted little fluorescence. As shown in Fig. 2(h), NAP-CF₃ displayed clear background, whereas Nile-Red showed partly nonspecific fluorescence from cells that are stained with LDs. The case above verified the enhanced fluorescence of NAP-CF₃ when binding to LDs.

Sequentially, we monitored the development process of fatty liver through confocal microscopy. As shown in Fig. 3, small LDs could be discriminated at an early stage (Week 1). Over time, the size and density of LDs grew bigger and higher. Finally, the fatty liver was full of large LDs, indicating that the fatty liver was mature. High-

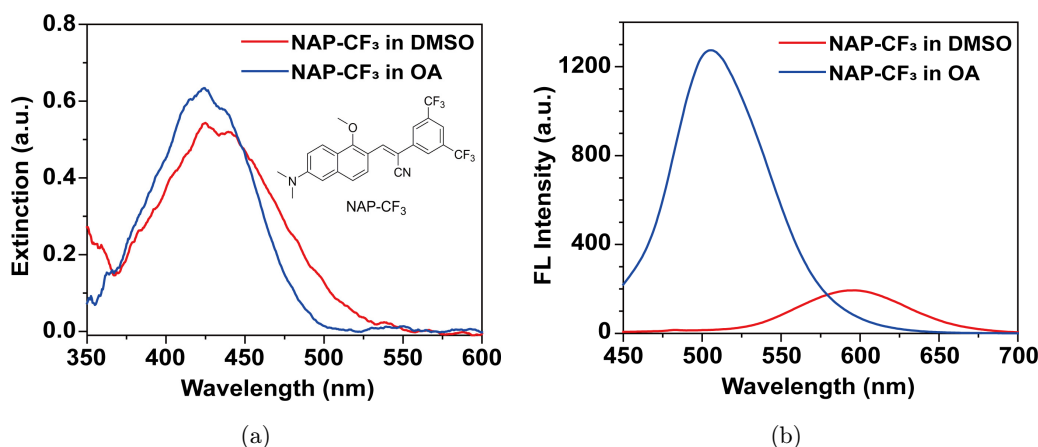


Fig. 1. Optical characterization of NAP-CF₃. (a) The extinction spectra of NAP-CF₃ in DMSO and oleic acid (OA). The concentration of NAP-CF₃ is 10 $\mu\text{g}/\text{mL}$, optical length = 1 mm. Insert: The structure of NAP-CF₃. (b) The fluorescence spectra of NAP-CF₃ (10 $\mu\text{g}/\text{mL}$) in DMSO and OA (Excitation wavelength is 420 nm).

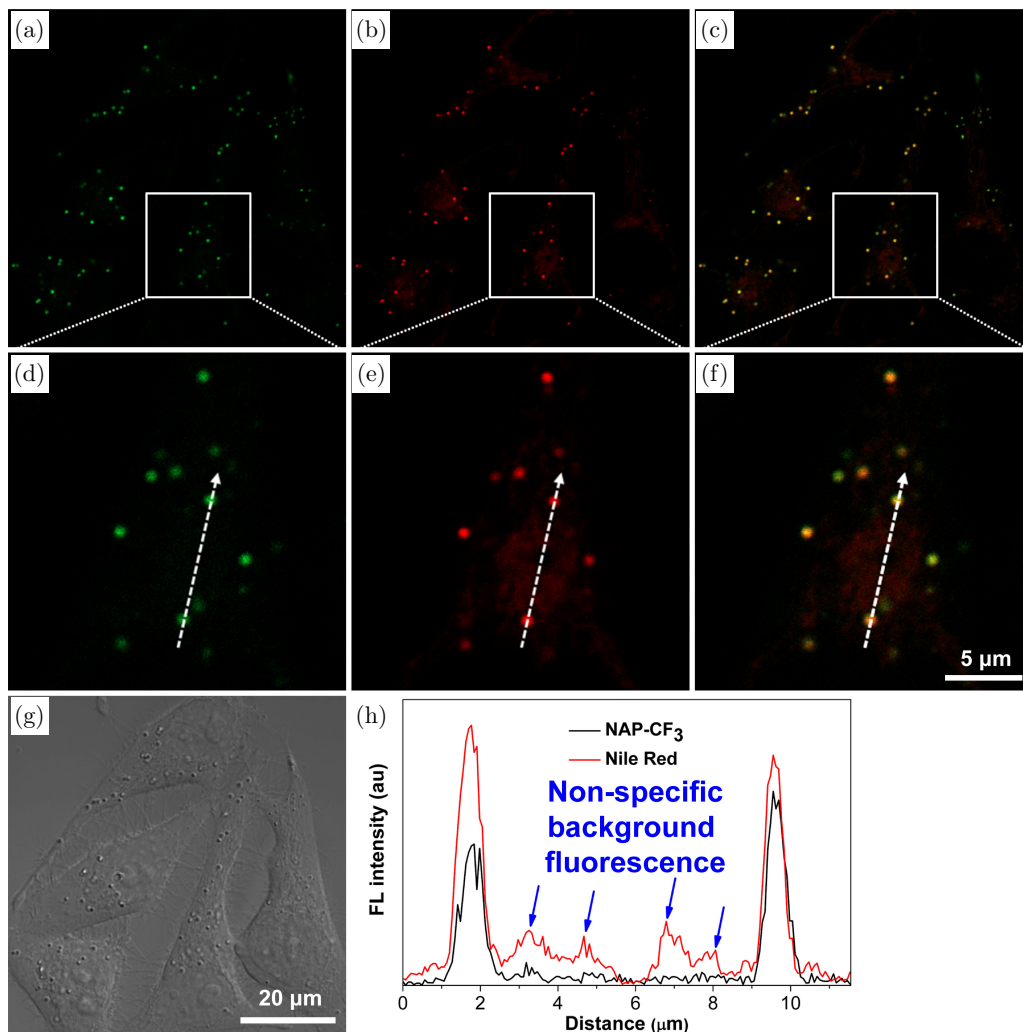


Fig. 2. Colocalized and zoomed-in confocal laser scanning microscope images ($\lambda_{\text{ex}} = 405 \text{ nm}$ for NAP- CF_3 and $\lambda_{\text{ex}} = 488 \text{ nm}$ for Nile-Red) of HeLa cells stained with (a, d) NAP- CF_3 (50 nM) and (b, e) Nile Red (100 nM). (c, f) merged images obtained from two different fluorescent panels and (g) image obtained from the bright field. (h) Fluorescent intensity obtained from NAP- CF_3 and Nile-Red.

contrast LDs imaging labeled by NAP- CF_3 successfully monitored the fatty liver at different stages, ensuring the high efficiency of fatty liver diagnosis.

Although confocal imaging of LDs could realize fatty liver diagnosis, the imaging was constricted within shallow slices (within 10- μm thickness). However, multi-photon imaging allows imaging with larger depth. Therefore, we tested multi-photon absorption performance of NAP- CF_3 . First, we measured the power dependence relationship between the fluorescence intensity of NAP- CF_3 and the excitation intensity. The fitted curve between logarithm of the fluorescence intensity and the excitation intensity was measured with a slope of 2.91 in Fig. 4(a), which indicated that a major three-

photon absorption process happened under 1300-nm fs excitation. We then measured three-photon absorption cross-section (σ_3) spectrum of NAP- CF_3 through comparison method reported previously.²⁷ The results showed that NAP- CF_3 had peak σ_3 at 1300 nm. The σ_3 at 1300 nm was calculated to be $1.67 \times 10^{-79} \text{ cm}^6 \text{ s}^2$, which is larger than most of commercial fluorophores.²² Moreover, we compared three-photon fluorescence imaging of NAP- CF_3 in DMSO and OA. The three-photon fluorescence of NAP- CF_3 in OA was brighter than it in DMSO. Fluorescence intensity of NAP- CF_3 in OA in Fig. 4(c) was 2.2 times as high as the fluorescence intensity of NAP- CF_3 in DMSO. The NAP- CF_3 in OA also showed excellent photostability under

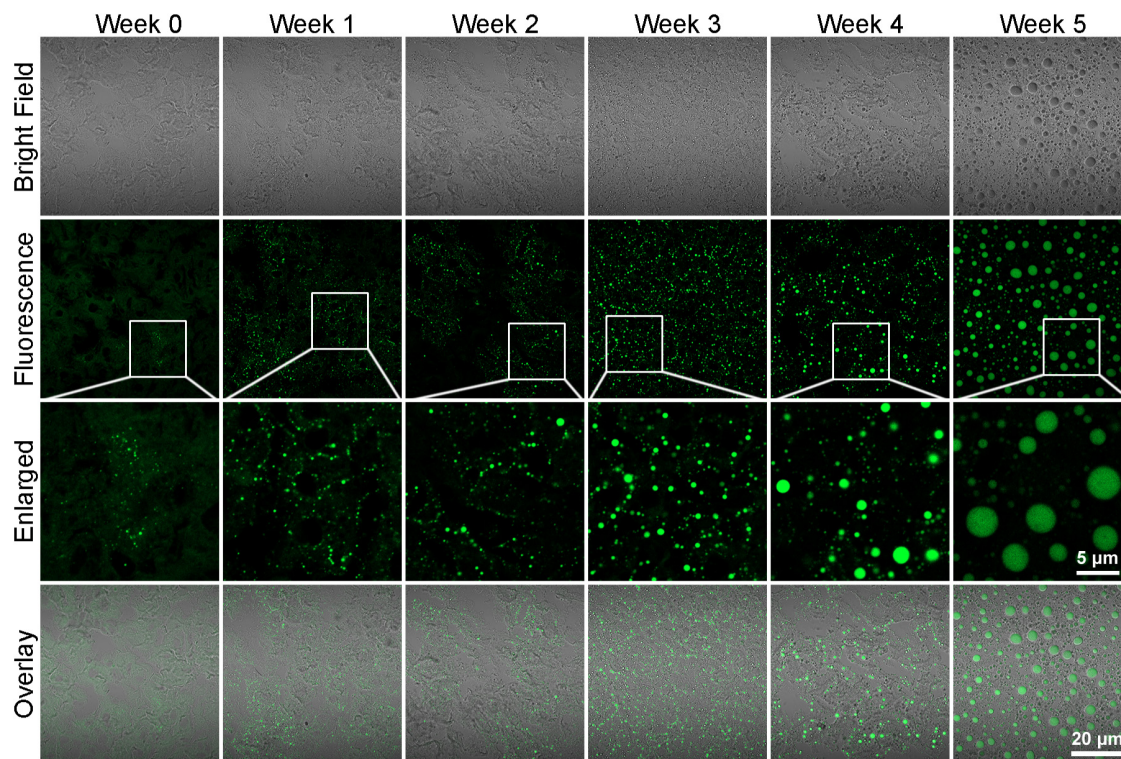


Fig. 3. Confocal laser scanning microscopic images ($\lambda_{\text{ex}} = 405 \text{ nm}$) of high-fat feeding control (Week 0) and experimental (Week 1 to Week 5) guinea pig liver tissues stained with NAP- CF_3 (50 nM) within 10- μm depth.

continuous 1300 nm fs excitation for more than 20 min in Fig. 4(d), where a power intensity of 10 mW is enough for three-photon imaging of LDs in liver tissues. The three-photon fluorescence had only been bleached by less than 15%. The remarkable three-photon performance of NAP- CF_3 guarantees its potential for 3PF LDs imaging.

Given its remarkable 3PF imaging performance, we further performed three-photon fluorescence imaging of LDs in liver tissues. The intensity of 3PF mainly constrains the imaging depth, while the emission wavelength plays a small role because the emission wavelength from green to red in 3PM does not significantly influence the fluorescence collection

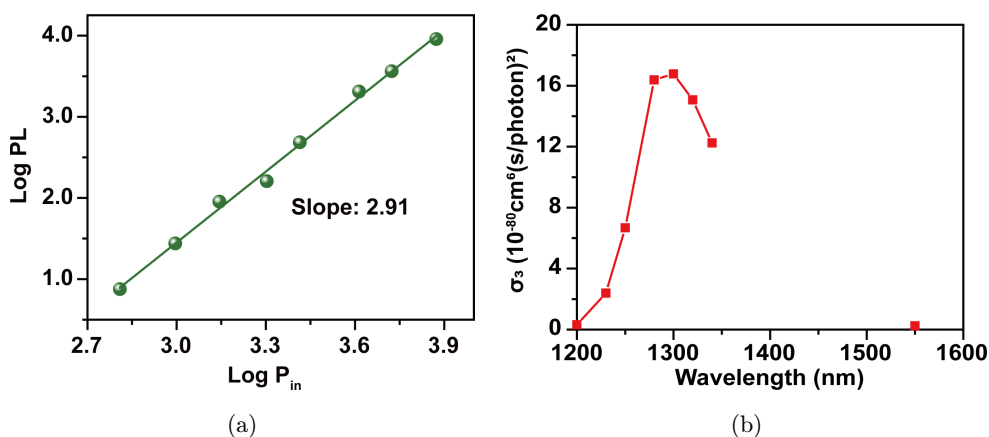


Fig. 4. (a) The logarithm of the fluorescence intensity of NAP- CF_3 against that of the 1300-nm fs excitation intensity curve. (b) The three-photon absorption cross-section spectrum of NAP- CF_3 in DMSO. (c) Quantitative analysis of fluorescence intensity of NAP- CF_3 (10 $\mu\text{g}/\text{mL}$) in DMSO and OA. Insert: three-photon fluorescence imaging of NAP- CF_3 (10 $\mu\text{g}/\text{mL}$) in DMSO and OA under 1300-nm fs excitation. (d) Photostability of NAP- CF_3 (10 $\mu\text{g}/\text{mL}$) in OA under the continuous irradiation of 1300 nm fs laser (Average power: 10 mW).

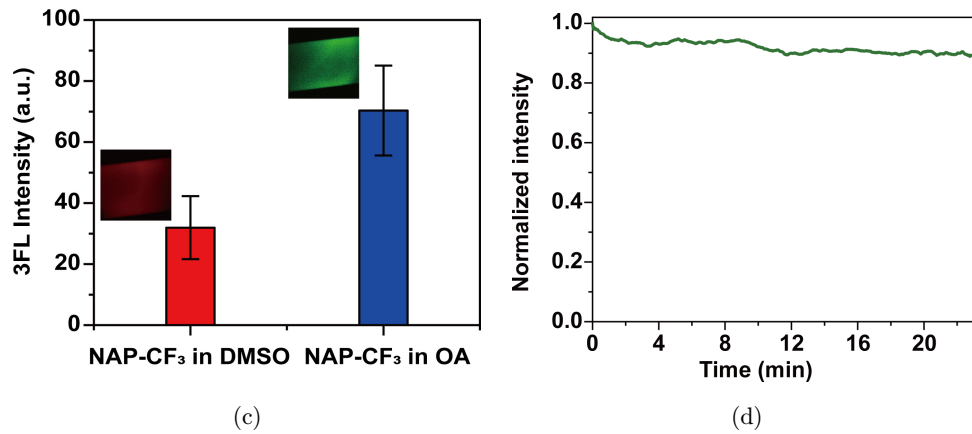


Fig. 4. (Continued)

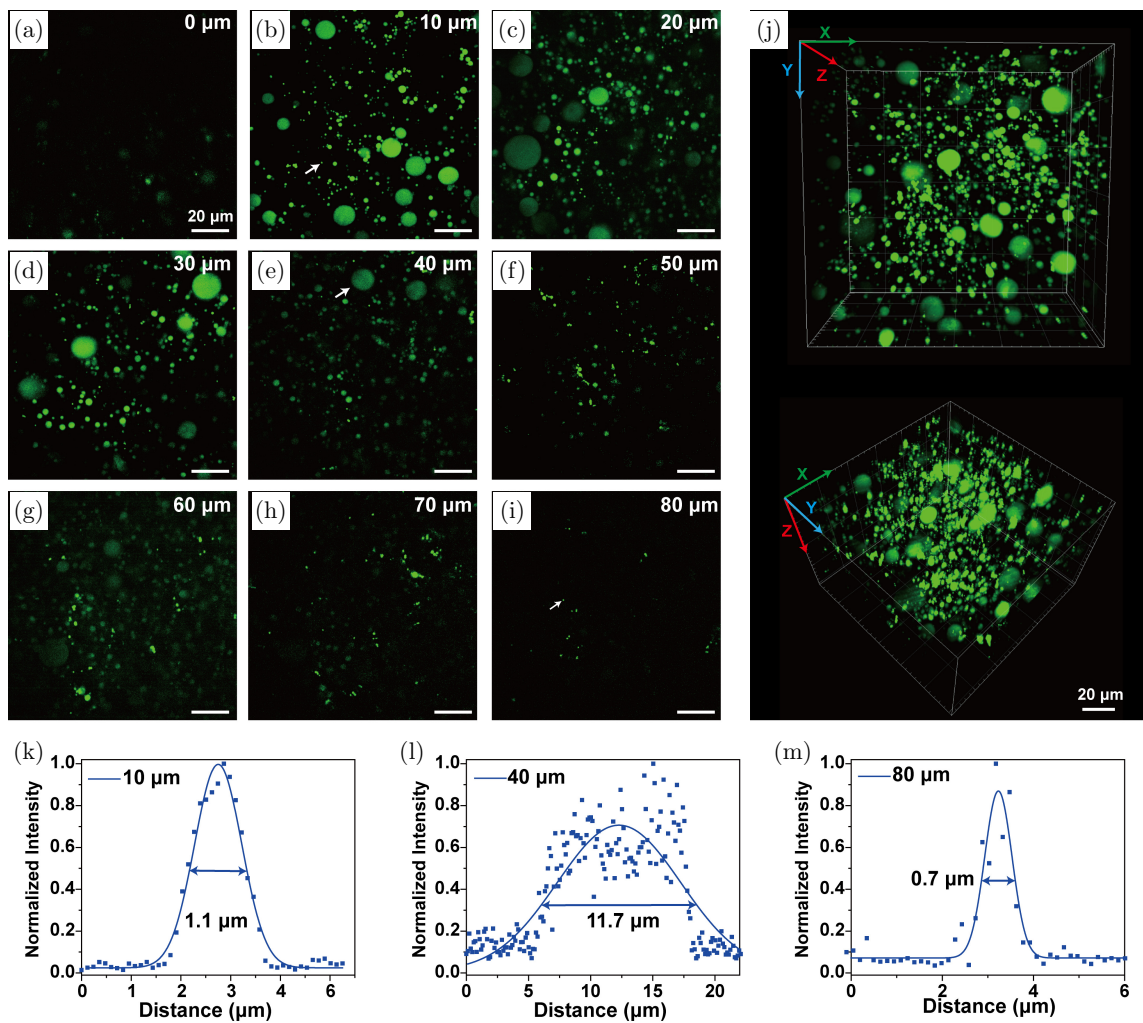


Fig. 5. *Ex vivo* three-photon fluorescence imaging of LDs in live mice fatty liver tissues. (a–i) Three-photon fluorescence microscopic imaging of LDs from 0 to 80 μm depth. (j) Reconstructed 3D three-photon fluorescence imaging of LDs (0–80 μm). (k–m) Gaussian analysis of arrow-pointed LD at imaging depth of 10 μm (b), 40 μm (e), and 80 μm (i).

efficiency.²⁹ Thus, the blue shift of NAP-CF₃ in OA would not hinder the 3PF imaging depth. Due to the enhanced three-photon fluorescence intensity of NAP-CF₃ in OA, deep LDs imaging was carried out in Fig. 5. The high nonlinear effect of 3PM guarantees good optical tomographic capability. Three-photon fluorescence imaging of LDs at different depths from 0 to 80 μm was shown with high contrast in Figs. 5(a)–5(i). Single LD as small as 1.1 μm was shown with high SBR [Fig. 5(k)]. Big LD at depth of 40 μm was also analyzed and was measured to be 11.7 μm [Fig. 5(l)]. Even small LD at depth of 80 μm was distinguishable with large SBR around 12 [Fig. 5(m)]. Finally, the reconstructed 3D images of LDs in Fig. 5(j) clearly showed the distribution of LDs. The effective attenuation length of 3PF imaging in liver was measured as around 15.0 μm , which demonstrated very high turbidity of liver tissue. *In vivo*, three-photon fluorescence imaging of LDs in our work was not achieved due to the fast jitter caused by mouse's breathing. Three-photon fluorescence imaging of LDs demonstrated lots of advantages, including high contrast, high resolution, and large imaging depth.

4. Conclusion

Our study demonstrated excellent imaging performances of NAP-CF₃ in precise high-resolution confocal imaging *in vitro*, and three-photon fluorescence imaging of LDs *ex vivo*. Due to the high specificity of this marker for LDs staining, the background fluorescence interference in imaging is dramatically reduced compared with commercial Nile Red. Meanwhile, the high specificity of NAP-CF₃ to LDs guarantees the diagnosis of fatty liver at an early stage. Three-photon fluorescence imaging promotes LDs imaging to a large depth. The high resolution and deep-tissue imaging of LDs achieved using NAP-CF₃ are important for future LDs-assisted pathologies research.

Conflicts of Interest

There are no conflicts to declare.

Acknowledgments

This work was supported by National Natural Science Foundation of China (61975172, 82001874, 62105184), and the Guangdong Basic

and Applied Basic Research Foundation (2020A1515110578). We thank Prof. Shijie Li from Guangzhou University of Chinese Medicine for giving helpful advices to perform the tissue imaging experiments. M. He and H. Park contributed equally to this paper.

References

1. A. R. Thiam, R. V. Jr. Farese, T. C. Walther, "The biophysics and cell biology of lipid droplets," *Nat. Rev. Mol. Cell Biol.* **14**(12), 775–786 (2013).
2. R. V. Jr. Farese, T. C. Walther, "Lipid droplets finally get a little R-E-S-P-E-C-T," *Cell* **139**(5), 855–860 (2009).
3. T. C. Walther, R. V. Jr. Farese, "Lipid droplets and cellular lipid metabolism," *Annu. Rev. Biochem.* **81**, 687–714 (2012).
4. J. A. Olzmann, C. M. Richter, R. R. Kopito, "Spatial regulation of UBXD8 and p97/VCP controls ATGL-mediated lipid droplet turnover," *Proc. Natl. Acad. Sci. USA* **110**(4), 1345–1350 (2013).
5. N. Kraemer, R. V. Jr. Farese, T. C. Walther, "Balancing the fat: Lipid droplets and human disease," *EMBO Mol. Med.* **5**(7), 973–983 (2013).
6. S. Daemen, M. van Zandvoort, S. H. Parekh, M. K. C. Hesselink, "Microscopy tools for the investigation of intracellular lipid storage and dynamics," *Mol. Metab.* **5**(3), 153–163 (2016).
7. W. Li, B. J. Dobraszczyk, P. J. Wilde, "Surface properties and locations of gluten proteins and lipids revealed using confocal scanning laser microscopy in bread dough," *J. Cereal Sci.* **39**(3), 403–411 (2004).
8. P. Raudsepp, D. A. Brüggemann, M. L. Andersen, "Detection of radicals in single droplets of oil-in-water emulsions with the lipophilic fluorescent probe BODIPY665/676 and confocal laser scanning microscopy," *Free Radic. Biol. Med.* **70**, 233–240 (2014).
9. E. Kim, S. Lee, S. B. Park, "A Seoul-Fluor-based bioprobe for lipid droplets and its application in image-based high throughput screening," *Chem. Commun.* **48**(17), 2331–2333 (2012).
10. C. Zhang, J. Li, L. Lan, J. X. Cheng, "Quantification of lipid metabolism in living cells through the dynamics of lipid droplets measured by stimulated raman scattering imaging," *Anal. Chem.* **89**(8), 4502–4507 (2017).
11. Y. Xu, H. Zhang, N. Zhang, R. Xu, Z. Wang, Y. Zhou, Q. Shen, D. Dang, L. Meng, B. Z. Tang, "An easily synthesized AIE luminogen for lipid droplet-specific super-resolution imaging and two-photon

- imaging, *Mater. Chem. Front.* **5**(4), 1872–1883 (2021).
12. S. Zhang, Z. Yang, M. Li, Q. Zhang, X. Tian, D. Li, S. Li, J. Wu, Y. Tian, “A multi-photon fluorescent probe based on quinoline groups for the highly selective and sensitive detection of lipid droplets,” *Analyst* **145**(24), 7941–7945 (2021).
 13. Y. Yu, H. Xing, H. Park, R. Zhang, C. Peng, H. H. Y. Sung, I. D. Williams, C. Ma, K. S. Wong, S. Li, Q. Xiong, M.-H. Li, Z. Zhao, B. Z. Tang, “Deep-red aggregation-induced emission luminogen based on dithiofuvalene-fused benzothiadiazole for lipid droplet-specific imaging,” *ACS Mater. Lett.* **4**(1), 159–164 (2022).
 14. M. Jiang, X. Gu, J. W. Y. Lam, Y. Zhang, R. T. K. Kwok, K. S. Wong, B. Z. Tang, “Two-photon AIE bio-probe with large Stokes shift for specific imaging of lipid droplets,” *Chem. Sci.* **8**(8), 5440–5446 (2017).
 15. H. Park, S. Li, G. Niu, H. Zhang, Z. Song, Q. Lu, J. Zhang, C. Ma, R. T. K. Kwok, J. M. Y. Lam, K. S. Wong, X. Yu, Q. Xiong, B. Z. Tang, “Diagnosis of fatty liver disease by a multiphoton-active and lipid-droplet-specific AIEgen with nonaromatic rotors,” *Mater. Chem. Front.* **5**(4), 1853–1862 (2021).
 16. T. Shao, T. Liu, H. Liu, M. Zhang, Y. Shen, A. Gao, X. Tian, Q. Zhang, J. Wu, Y. Tian, “Identification of fatty liver disease at diverse stages using two-photon absorption of triphenylamine-based BODIPY analogues,” *J. Mater. Chem. B* **7**(23), 3704–3709 (2019).
 17. L. Guo, M. Tian, R. Feng, G. Zhang, R. Zhang, X. Li, Z. Liu, X. He, J. Z. Sun, X. Yu, “Interface-targeting strategy enables two-photon fluorescent lipid droplet probes for high-fidelity imaging of turbid tissues and detecting fatty liver,” *ACS Appl. Mater. Interfaces* **10**(13), 10706–10717 (2018).
 18. M.-Y. Wu, J.-K. Leung, C. Kam, T. Y. Chou, D. Wang, S. Feng, S. Chen, “A near-infrared AIE probe for super-resolution imaging and nuclear lipid droplet dynamic study,” *Mater. Chem. Front.* **5**(7), 3043–3049 (2021).
 19. X. Nan, E. O. Potma, X. S. Xie, “Nonperturbative chemical imaging of organelle transport in living cells with coherent anti-stokes raman scattering microscopy,” *Biophys. J.* **91**(2), 728–735 (2006).
 20. M. Liu, B. Gu, W. Wu, Y. Duan, H. Liu, X. Deng, M. Fan, X. Wang, X. Wei, K.-T. Yong, K. Wang, G. Xu, B. Liu, “Binary organic nanoparticles with bright aggregation-induced emission for three-photon brain vascular imaging,” *Chem. Mater.* **32**(15), 6437–6443 (2020).
 21. L. Streich, J. C. Boffi, L. Wang, K. Alhalaseh, M. Barbieri, R. Rehm, S. Deivasigamani, C. T. Gross, A. Agarwal, R. Prevedel, “High-resolution structural and functional deep brain imaging using adaptive optics three-photon microscopy,” *Nat. Methods* **18**(10), 1253 (2021).
 22. Y. Hontani, F. Xia, C. Xu, “Multicolor three-photon fluorescence imaging with single-wavelength excitation deep in mouse brain,” *Sci. Adv.* **7**(12), eabf3531 (2021).
 23. Z. L. Qiu, M. B. He, K. S. Chu, C. Tang, X. W. Chen, L. Zhu, L. P. Zhang, D. Sun, J. Qian, Y. Z. Tan, “Well-defined segment of carbon nanotube with bright red emission for three-photon fluorescence cerebrovascular imaging,” *Adv. Opt. Mater.* **9**(19), 2100482 (2021).
 24. N. G. Horton, K. Wang, D. Kobat, C. G. Clark, F. W. Wise, C. B. Schaffer, C. Xu, “In vivo three-photon microscopy of subcortical structures within an intact mouse brain,” *Nat. Photonics* **7**(3), 205–209 (2013).
 25. S. Wang, X. Li, S. Y. Chong, X. Wang, H. Chen, C. Chen, L. G. Ng, J. W. Wang, B. Liu, “In vivo three-photon imaging of lipids using ultrabright fluorogens with aggregation-induced emission,” *Adv. Mater.* **33**(11), e2007490 (2021).
 26. G. Niu, R. Zhang, J. P. C. Kwong, J. W. Y. Lam, C. Chen, J. Wang, Y. Chen, X. Feng, R. T. K. Kwok, H. H. Y. Sung, I. D. Williams, M. R. J. Elsegood, J. Qu, C. Ma, K. S. Wong, X. Yu, B. Z. Tang, “Specific two-photon imaging of live cellular and deep-tissue lipid droplets by lipophilic AIEgens at ultralow concentration,” *Chem. Mater.* **30**(14), 4778–4787 (2018).
 27. M. He, D. Li, Z. Zheng, H. Zhang, T. Wu, W. Geng, Z. Hu, Z. Feng, S. Peng, L. Zhu, W. Xi, D. Zhu, B. Z. Tang, J. Qian, “Aggregation-induced emission nanoprobe assisted ultra-deep through-skull three-photon mouse brain imaging,” *Nano Today* **45**, 101536 (2022).
 28. L.-C. Cheng, N. G. Horton, K. Wang, S.-J. Chen, C. Xu, “Measurements of multiphoton action cross sections for multiphoton microscopy,” *Biomed. Opt. Express* **5**(10), 3427–3433 (2014).
 29. M. Wang, M. Kim, F. Xia, C. Xu, “Impact of the emission wavelengths on in vivo multiphoton imaging of mouse brains,” *Biomed. Opt. Express* **10**(4), 1905–1918 (2019).

Near-Infrared Photothermal Manipulates Cellular Excitability and Animal Behavior in *Caenorhabditis elegans*

Siyi Zhuang, Mubin He, Jiaqi Feng, Shiyi Peng, Haochen Jiang, Yunhao Li, Ning Hua, Yujie Zheng, Qizhen Ye, Miaojin Hu, Ying Nie, Peilin Yu, Xiaomin Yue,* Jun Qian,* and Wei Yang*

Near-infrared (NIR) photothermal manipulation has emerged as a promising and noninvasive technology for neuroscience research and disease therapy for its deep tissue penetration. NIR stimulated techniques have been used to modulate neural activity. However, due to the lack of suitable *in vivo* control systems, most studies are limited to the cellular level. Here, a NIR photothermal technique is developed to modulate cellular excitability and animal behaviors in *Caenorhabditis elegans* *in vivo* via the thermosensitive transient receptor potential vanilloid 1 (TRPV1) channel with an FDA-approved photothermal agent indocyanine green (ICG). Upon NIR stimuli, exogenous expression of TRPV1 in AFD sensory neurons causes Ca^{2+} influx, leading to increased neural excitability and reversal behaviors, in the presence of ICG. The GABAergic D-class motor neurons can also be activated by NIR irradiation, resulting in slower thrashing behaviors. Moreover, the photothermal manipulation is successfully applied in different types of muscle cells (striated muscles and nonstriated muscles), enhancing muscular excitability, causing muscle contractions and behavior changes *in vivo*. Altogether, this study demonstrates a noninvasive method to precisely regulate the excitability of different types of cells and related behaviors *in vivo* by NIR photothermal manipulation, which may be applied in mammals and clinical therapy.

been developed, such as optogenetics,^[1–4] chemogenetics,^[5–7] electrical stimulation,^[8–11] ultrasound stimulation,^[12–15] and magnetothermal modulation.^[16–19] Among them, the most widely used neuromodulation technique is optogenetics, which can manipulate neurons by optical stimulation with spatiotemporal precision and sensitivity. However, implantation of optical fibers often causes tissue damage and immune response, and the penetration of visible light is too shallow to stimulate deep brain tissues.^[20,21] The invasive problem also exists in traditional electrical stimulation, due to the electrodes are needed to be implanted into the mouse brain.^[22,23] Then some non-invasive techniques emerged, such as the magnetothermal modulation, which can perform strong tissue penetration without brain implants concerns, has been applied to evoke motor behaviors in mice. Yet, the activation requires high magnetic field strength, a resonant coil in close vicinity to the subject's head is needed.^[16–18] Another option for non-invasive manipulation

is chemogenetics, using small chemical molecules to regulate target cells through ligand receptors. But the time resolution is coarse and hard to control, because the drugs have

1. Introduction


In order to explore the complex nervous system and achieve precise therapy, a variety of neural manipulation techniques have

S. Zhuang, J. Feng, H. Jiang, Y. Li, N. Hua, Y. Zheng, Q. Ye, M. Hu, Y. Nie, X. Yue, W. Yang
Department of Biophysics
Department of Neurology of the Fourth Affiliated Hospital
Zhejiang University School of Medicine
Hangzhou 310058, China
E-mail: yuexiaomin@zju.edu.cn; yangwei@zju.edu.cn

M. He, S. Peng, J. Qian
State Key Laboratory of Modern Optical Instrumentations
Centre for Optical and Electromagnetic Research
College of Optical Science and Engineering
International Research Center for Advanced Photonics
Zhejiang University
Hangzhou 310058, China
E-mail: qianjun@zju.edu.cn

P. Yu
Department of Toxicology
Department of Medical Oncology of the Second Affiliated Hospital
Zhejiang University School of Medicine
Hangzhou 310058, China

W. Yang
MOE Frontier Science Center for Brain Research and Brain-Machine Integration
Zhejiang University School of Medicine
Hangzhou 310058, China

 The ORCID identification number(s) for the author(s) of this article can be found under <https://doi.org/10.1002/smt.202300848>

© 2023 The Authors. Small Methods published by Wiley-VCH GmbH. This is an open access article under the terms of the Creative Commons Attribution License, which permits use, distribution and reproduction in any medium, provided the original work is properly cited.

DOI: 10.1002/smt.202300848

long residence time in vivo.^[6,7] Ultrasound stimulation is also a non-invasive technique for neural modulation, which can pass through the skull to deep brain regions. And the derived sonogenetics, refers to using ultrasound to modulate neural activity through ultrasound-responsive channels, such as MscL, Prestin, Piezo1 and TRP family channels.^[24–28] However, since the development of ultrasound stimulation is still in its infancy, the underlying mechanism and potential side effects are poorly studied, there are still many uncertainties in its specificity and safety.^[29] Therefore, it is desirable to develop a non-invasive technique to precisely modulate neural activity with high biosafety, especially in vivo.

Near-infrared (NIR) light modulation with a wavelength of 700–1880 nm, which is well known as “biological transparency window” due to its deep tissue penetration, has emerged as a promising and noninvasive technology for neuroscience research and disease therapy.^[30,31] Especially, NIR-stimulated optogenetic tools have been used to directly regulate neural activity through NIR-responsive materials. Such as the lanthanide up-conversion nanoparticles (UCNPs), which can convert NIR light into short wavelength visible light emission to stimulate photosensitive proteins sensitive to visible light (ChR2, Chrimson and NpHR, et al.).^[32–34] Another type of emerged NIR responsive materials is NIR-responsive photothermal materials, which can convert NIR light energy into heat and then trigger thermosensitive proteins expressed on cell membranes. Various kinds of photothermal agents have been synthesized and studied, including organic polymers,^[35,36] gold nanoparticles,^[37] carbon-based materials,^[38,39] semiconductors,^[40] and samll dyes.^[41] Although some NIR-responsive materials have excellent photoconversion or photothermal conversion properties, and already be used to regulate cellular signaling pathways and gene transcription in a noninvasive manner. However, it should be noted that most of the NIR-responsive materials are inorganic or metal nanomaterials, which are difficult to apply in modulation of neural activity in vivo or clinical therapy, due to their biological toxicity and safety hazards.

Indocyanine green (ICG) dye is an FDA-approved photothermal agent, which can effectively transfer optical energy to thermal energy in response to NIR stimuli. And ICG can be metabolized by livers, has a short life time in blood circulation. Due to its excellent photothermal conversion efficiency and biosafety, ICG is widely used in angiography and photothermal treatment of tumor.^[42–45] Therefore, ICG may be a promising candidate material for photothermal modulation of cellular activity in vivo.

The nematode *Caenorhabditis elegans* (*C. elegans*) is an extensively used model organism with numerous advantages for neuroscience research, including the small but well-characterized nervous system, complete connectome, amenability to genetic manipulation, short life span, and complex behavioral characteristics.^[46,47] *C. elegans* offers a fast and mature in vivo experimental system to critically evaluate and optimize the effects and efficacy of neural modulation techniques.

In the present study, we developed a NIR photothermal system to regulate *C. elegans* cellular excitability and related behaviors in freely moving animals through thermosensitive TRPV1 channel with ICG in vivo. We successfully applied the photothermal modulation specifically in different types of neurons and muscle cells to mediate corresponding behaviors. Upon NIR stimuli at

793 nm with ICG, TRPV1 exogenously expressed AFD sensory neurons showed Ca²⁺ influx and increase of neural excitability, and then induced backward locomotion. The GABAergic D-class motor neurons can also be activated by NIR irradiation, resulting in slower thrashing behaviors. Moreover, our system can also activate body wall muscles and vulva muscles, enhancing muscular excitability, leading to muscle contractions which induced paralysis and egg-laying behaviors respectively in *C. elegans*. Meanwhile, ICG showed no negative effects on survival, reproduction and lifespan of the nematodes. Altogether, we demonstrate a non-invasive and effective method to precisely regulate the excitability of different types of cells and animal behaviors in vivo by NIR photothermal manipulation.

2. Results

2.1. Optical and Photothermal Characterization of ICG in vitro

ICG is a tricyanocyanine dye with a molecular weight of 751.4 Da. It is an FDA-approved clinical drug with high biocompatibility and has been widely used in angiography and fluorescence imaging.^[44,45] First, we measured the optical and photothermal characterization of ICG. In our test, ICG showed an absorption spectrum ranging from 600 to 850 nm, the maximum absorption peak was observed at 796.5 nm, and the emission spectrum ranging from 700 to 1100 nm with a peak value at 865.2 nm (Figure 1a). These results suggested that ICG can be effectively excited by NIR stimuli at 793 nm, which would be used in our following experiments. Then, we tested the photothermal efficacy of ICG. After continuous irradiation by 793 nm (10 mW mm⁻²) near-infrared laser, the temperature increased in a dose-dependent manner with ICG concentration at 1, 3, 10, 30, 50, and 100 µg mL⁻¹ (Figure 1c). The temperature of ICG reached plateau to 28.40 ± 0.10, 30.17 ± 0.23 °C, 40.40 ± 1.00 °C, 46.00 ± 0.95 °C, 50.97 ± 0.90 °C and 52.17 ± 0.12 °C, at the time of 0.67, 2.33, 3.00, 4.33, 4.91, and 5.33 min, respectively (Figure 1c-d), but did not change upon laser irradiation at the absence of ICG. The photothermal efficacy of ICG reached saturation level from the concentration of 50 µg mL⁻¹.

We then evaluated the temperature oscillation of ICG in fetal bovine serum (FBS) or in ultrapure water under a pulsed NIR irradiation (10 mW mm⁻², 4 min duration, 4 min intervals, 5 cycles). It was observed that the peak temperature of ICG dissolved in ultrapure water did not decrease significantly during the first three NIR exposures, but began to decrease significantly at the fourth irradiation. However, there was no significant change in the ICG solution mixed with FBS during the entire irradiation (Figure 1b). We also confirmed that pure FBS solution has no temperature oscillation under NIR irradiation (Figure S1, Supporting Information). These results showed a more stable photostability of ICG in FBS at NIR laser irradiation, which can be used for photothermal manipulation, so we performed our experiments with ICG dissolved in FBS.

2.2. In Vitro NIR Photothermal Activation of TRPV1 with ICG

We further evaluated the photothermal efficiency of ICG under NIR illumination in cultured cells. First, we examined whether

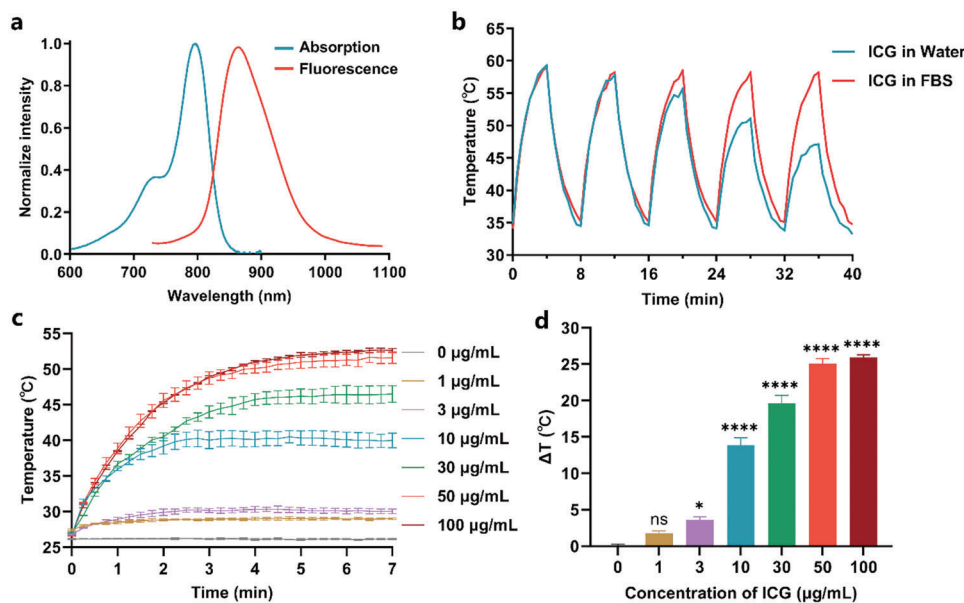


Figure 1. Optical and photothermal characterization of ICG. a) The absorption and fluorescence spectra of ICG. b) The temperature oscillation of 100 $\mu\text{g mL}^{-1}$ ICG in FBS or ultrapure water, within five irradiation-cooling cycles (793 nm, 10 mW mm^{-2}). c) 793 nm NIR-induced photothermal effect of ICG. Data shown as mean \pm SEM, $n = 3$. d) The temperature change of ICG with different concentration when reached the final plateau under NIR irradiation, as in (c). Data shown as mean \pm SEM, $n = 3$. ns, not significant ($p > 0.05$), * $p < 0.05$, **** $p < 0.0001$ by one-way ANOVA.

ICG can be effectively taken up by cells. After 1 h incubation, both the SY5Y neuroblastoma cells (Figure S2a, Supporting Information) and HEK293T cells (Figure S2d, Supporting Information) were effectively labeled by ICG and sustained a detectable signal-to-noise ratio fluorescence in NIR fluorescence microscopic imaging.

Then, to explore if the NIR-ICG photothermal system can modulate cellular activity, we transfected the mouse TRPV1 (mTRPV1) tagged with mCherry in HEK293T cells. The transient receptor potential cation channel subfamily V member 1 (TRPV1) is a well-known temperature-sensitive ion channel. Activating TRPV1 by high temperature ($>43^\circ\text{C}$) can induce Ca^{2+} influx, which is a vital physiological process in neural firing.^[48,49] The Ca^{2+} influx was monitored using an intracellular calcium fluorescent indicator Fluo-8am in our study. When elevated both temperature to 45°C , a calcium increase was observed in mTRPV1-mCherry transfected HEK293T cells (Figure S2b, Supporting Information), but not in control cells which were transfected with mCherry only (Figure S2c, Supporting Information). Importantly, the mTRPV1 transfected HEK293T cells can also be activated by NIR irradiation after ICG incubation, exhibited a significant calcium increase (Figure S2e, Supporting Information). When the cells were treated with ICG or NIR only, or not transfected with mTRPV1, there was no significant change in intracellular calcium signal. These cells could still be activated by capsaicin, the agonist of TRPV1, suggested the effective expression of TRPV1 and normal cellular physiological functions after treatment with the NIR and ICG. These data demonstrated that exogenously expressed TRPV1 could be activated by NIR stimuli with photothermal agent ICG, leading to a calcium response in HEK293T cells.

2.3. Photothermal Characterization of ICG in *C. elegans* In Vivo

Having demonstrated the effectiveness of NIR-ICG system in vitro, we asked whether the photothermal manipulation can be used in living animals. We chose *Caenorhabditis elegans* as the experimental model, and investigated the photothermal characterization of ICG in vivo. In order to test whether ICG could be introduced into the nematodes, we mixed ICG with *Escherichia coli*, the food of *C. elegans*. After ≈ 12 h of feeding, the wide-field near-infrared fluorescence imaging was performed. And the ICG fluorescence signals could be firstly observed in the anterior pharynx in *C. elegans* after feeding with $0.2 \mu\text{g mL}^{-1}$ ICG. Moreover, when increasing the ICG concentration to $1 \mu\text{g mL}^{-1}$ and $2 \mu\text{g mL}^{-1}$, the whole pharynx and intestine of the nematode progressively exhibited obvious ICG fluorescence signals (Figure 2a). These results indicated that ICG could enter the nematodes by feeding and distribute along the digestive system of the worms.

To explore whether the heat generated by NIR-ICG photothermal system was sufficient to regulate the physiological activities of *C. elegans*, we generated a transgenic strain carrying a transcriptional reporter gene *gfp* driven by the promoter of *hsp-4* gene (heat shock protein). Using this transgenic strain, we can directly detect the expression of HSP-4 by observing the GFP fluorescence intensity changes. HSP-4 is expressed in several tissues including hypodermis, intestine, spermatheca, and some neuron cells. And the transcription of *hsp-4* can be upregulated in response to endoplasmic reticulum stress induced by dithiothreitol (DTT) or tunicamycin (unfolded protein response) as well as in response to heat shock.^[50,51] To test the thermal activation efficiency of *Phsp-4::GFP* strain, we incubated the nematodes at 33°C for different lengths of time, then detected the GFP fluorescence intensity of the worms. We found that the GFP represented

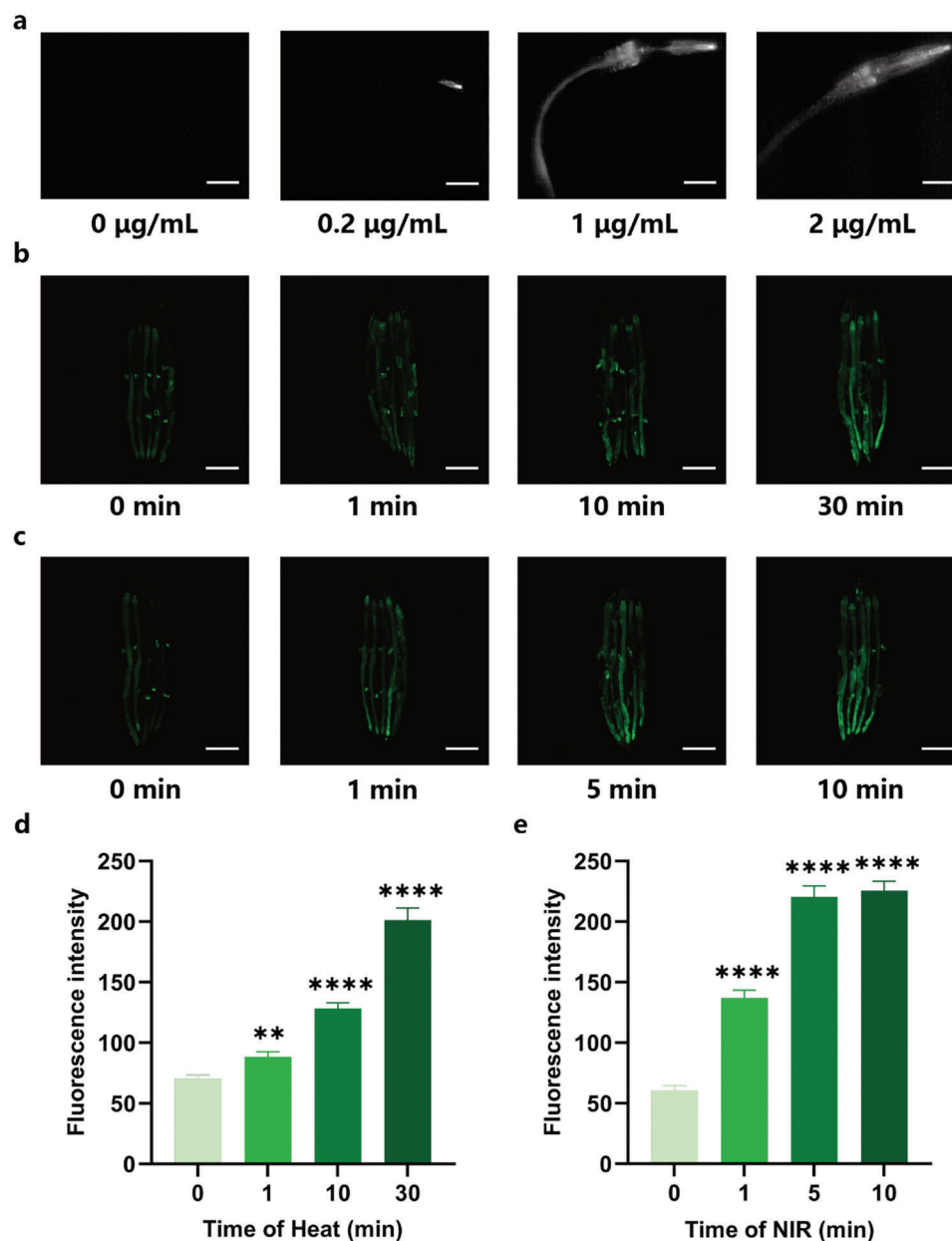


Figure 2. Photothermal characterization of ICG in *C. elegans* in vivo. a) Wide-field near-infrared fluorescence images of *C. elegans* after feeding with ICG (0, 0.2, 1, 2 µg mL⁻¹, 12 h). Scale bar = 50 µm. b) Confocal images of *Phsp-4::GFP* strain *C. elegans* after heating at 33 °C (0, 1, 10, 30 min). Scale bar = 200 µm. c) Confocal images of *Phsp-4::GFP* strain *C. elegans* after NIR irradiation (0, 1, 5, 10 min, 793 nm, 10 mW mm⁻²) with ICG (10 µg mL⁻¹). Scale bar = 200 µm. d,e) Quantification of *Phsp-4::GFP* expression in the entire animals as depicted in (b) and (c). Fluorescence intensity was detected 2 h after treatment. Data shown as mean ± SEM, n ≥ 35. ** *p* < 0.01, **** *p* < 0.0001 by Brown-Forsythe and Welch ANOVA tests.

expression of HSP-4 increased obviously and progressively after heating from 1 to 30 min (Figure 2b,d). Then, we performed the heat shock experiment through our NIR-ICG photothermal system. Excitingly, the photothermal manipulation also induced significant heat shock effect. After feeding with 10 µg mL⁻¹ ICG for 12 h, worms were irradiated by continuous NIR light (793 nm, 10 mW mm⁻²). We also applied gradient experiments at different stimulation times. With the extension of NIR irradiation time, the expression of HSP-4 also increased, in the presence of ICG.

It showed that the expression of HSP-4 was visibly upregulated under NIR irradiation for only 1 min. And treated worms with NIR-ICG photothermal stimulation for 5 min or 10 min was sufficient to fully activate HSP-4 expression, which demonstrated the high efficiency and effectiveness of our photothermal system (Figure 2c,e). NIR irradiation at 793 nm had no effect on temperature change of the NGM plates per se (Figure S3, Supporting Information). Collectively, these data suggested that ICG could successfully perform photothermal conversion response to NIR

stimuli in vivo. Moreover, it is the first time to modulate the expression of heat shock proteins by a photothermal system, rather than direct heat in *C. elegans*.

2.4. Distribution of ICG in *C. elegans* Ingested by Feeding

To further test if our NIR-ICG photothermal system can regulate the activity of specific tissue cells in vivo, we constructed transgenic nematode strains expressing TRPV1 in different types of neurons and muscle cells. DsRed was used to label the target tissue cells. Confocal images showed the exogenous expression of mTRPV1-sl2-DsRed in AFD sensory neurons, the GABAergic D-class motor neurons (D-MNs), body wall muscles and vulva muscles in *C. elegans* driven by their own tissue-specific promoters, respectively (Figure S4, Supporting Information). Then to test if these tissue cells can be activated specifically by NIR with ICG, these transgenic worms were fed by *Escherichia coli* food mixed with ICG, as in the previous photothermal heat shock experiment indicated. After about 12 h of feeding, two-photon scanning fluorescence microscopic (TPFSM) imaging was performed to detect the expression of mTRPV1-sl2-DsRed and the location of ingested ICG on the same worm. The ICG fluorescence signals were widely distributed along the alimentary canal of *C. elegans* (Figure 3). We then measured the distance between ICG and TRPV1 expressed tissue cells (Figure 3b–d). We found that the ingested ICG has a distance $\approx 5 \mu\text{m}$ from AFD sensory neurons, $9 \mu\text{m}$ from D-class motor neurons, $8 \mu\text{m}$ from vulva muscles and $10 \mu\text{m}$ from body wall muscles, respectively. As the data showed, the distance between ICG and tissue cells was less than $10 \mu\text{m}$, indicating a possible effective photothermal transfer to targeted cells. Next, we examined the activation of these specific tissue cells by NIR-ICG photothermal stimulation and detected some interesting corresponding behavioral output.

2.5. In Vivo NIR Photothermal Modulation of AFD Sensory Neurons Excitability and Reversal Locomotion

AFD neurons are the main thermosensors in *C. elegans*, which respond to thermal fluctuations at temperatures above its cultivation temperature (T_c).^[52,53] The animal increases its reversal and turn frequency when detects a rise in temperature and then moves back down the gradient toward T_c (negative thermotaxis). This avoidance response requires the cell autonomous function of cGMP-dependent TAX-2/TAX-4 cation channels in AFD neurons.^[54,55] We constructed a transgenic strain expressing mTRPV1 in AFD neurons in *tax-2* mutant worms (*tax-2*; *Pgcy-8::mTRPV1::sl2::Dsred*, also shown as *tax-2*; AFD::mTRPV1). When performed NIR irradiation at 50 mW mm^{-2} power density, N2 worms fed with ICG showed a rapid retreat behavior, and the reversal rate increased with the concentration of ICG (Figure 4a–b). This result proved our NIR-ICG photothermal system can effectively induce thermal sensing retreat behavior. While there was no obvious behavioral response to the photothermal system in *tax-2* mutant worms, which is consistent with previous research that *tax-2* mutations lost the major heat sensing abilities. Excitingly, *tax-2*; AFD::mTRPV1 transgenic worms showed a rescued heat sensing phenotype, exhib-

ited a ICG concentration-dependent (from 0 to $4 \mu\text{g mL}^{-1}$) photothermal reversal behavior as N2 worms (Figure 4a–b). What's more, both N2 and *tax-2*; AFD::mTRPV1 transgenic worms showed NIR power-dependent (from 0 to 16 mW mm^{-2}) photothermal reversal behavior with ingested ICG concentration at $2 \mu\text{g mL}^{-1}$, but not in *tax-2* mutations (Figure 4a,c). These results showed that our NIR-ICG manipulation can effectively induce thermosensitive reversal behavior through the thermosensitive TRPV1 channel expressed in AFD sensory neurons in vivo.

Previous research reported AFD neurons responded to thermal stimuli above T_c with Ca^{2+} influx via cGMP-dependent TAX-2/TAX-4 cation channels.^[56–58] To further test if our NIR-ICG photothermal system can regulate the excitability of AFD sensory neurons through TRPV1, we co-expressed TRPV1 and GCaMP5 in AFD neurons in the background of *tax-2* mutation (*tax-2*; *Pgcy-8::mTRPV1::sl2::Dsred+Pgcy-8::GCaMP5*, also showed as *tax-2*; AFD::mTRPV1+ GCaMP5), which enabled us to measure the intracellular calcium changes in AFD neurons. When we rapidly raised the temperature of the bath solution in which the *C. elegans* were incubated to $\approx 45^\circ\text{C}$, the AFD neurons showed an increase in calcium signal. Interestingly, a large increase in calcium was also observed in AFD neurons upon NIR irradiation at 25 mW mm^{-2} power density with ICG concentration of $10 \mu\text{g mL}^{-1}$. But there was no response when NIR was performed alone (Figure 4d–f). Compared with direct heating, it took a longer time for AFD neurons to increase the intracellular calcium to the peak value under NIR-ICG photothermal stimulation, although the peak values were almost equal (Figure 4d). The different dynamic characteristics suggested that photothermal manipulation can activate AFD neurons in a slower and gentler manner, indicating a better controllability in vivo. Together, these results demonstrated our NIR-ICG manipulation can effectively activate AFD sensory neurons and regulate thermosensitive reversal behavior through TRPV1 in vivo.

2.6. NIR Activate D-Class Motor Neurons to Reduce Thrashing Frequency in Swimming Behavior

Next, we examined if our NIR-ICG photothermal system can regulate the activity of motor neurons which did not have temperature sensitivity. We constructed a transgenic strain expressing mTRPV1 in D-class motor neurons (*tax-2*; *Pttr39::mTRPV1::sl2::Dsred*, also shown as *tax-2*; D-MNs::mTRPV1). In *C. elegans*, D-MNs are inhibitory motor neurons which can release GABA neurotransmitter to muscle cells, causing muscle relaxation along the body, then slow down or halt locomotion.^[59,60] We performed a thrashing assay, wherein nematodes generated body bends in M9 solution. NIR illumination (793 nm , 12.5 mW mm^{-2}) induced a significantly reduced thrashing frequency with ICG ($1 \mu\text{g mL}^{-1}$) in *tax-2*; D-MNs::mTRPV1 animals. And the motor behaviors can resume after the light was removed, which showed that the photothermal manipulation did not cause any tissue damage (Figure 5a). Neither N2 nor *tax-2* mutant animals showed obvious slower thrashing upon NIR stimulation with ICG, suggested that TAX-2 did not function in D-MNs, it was the exogenously expressed

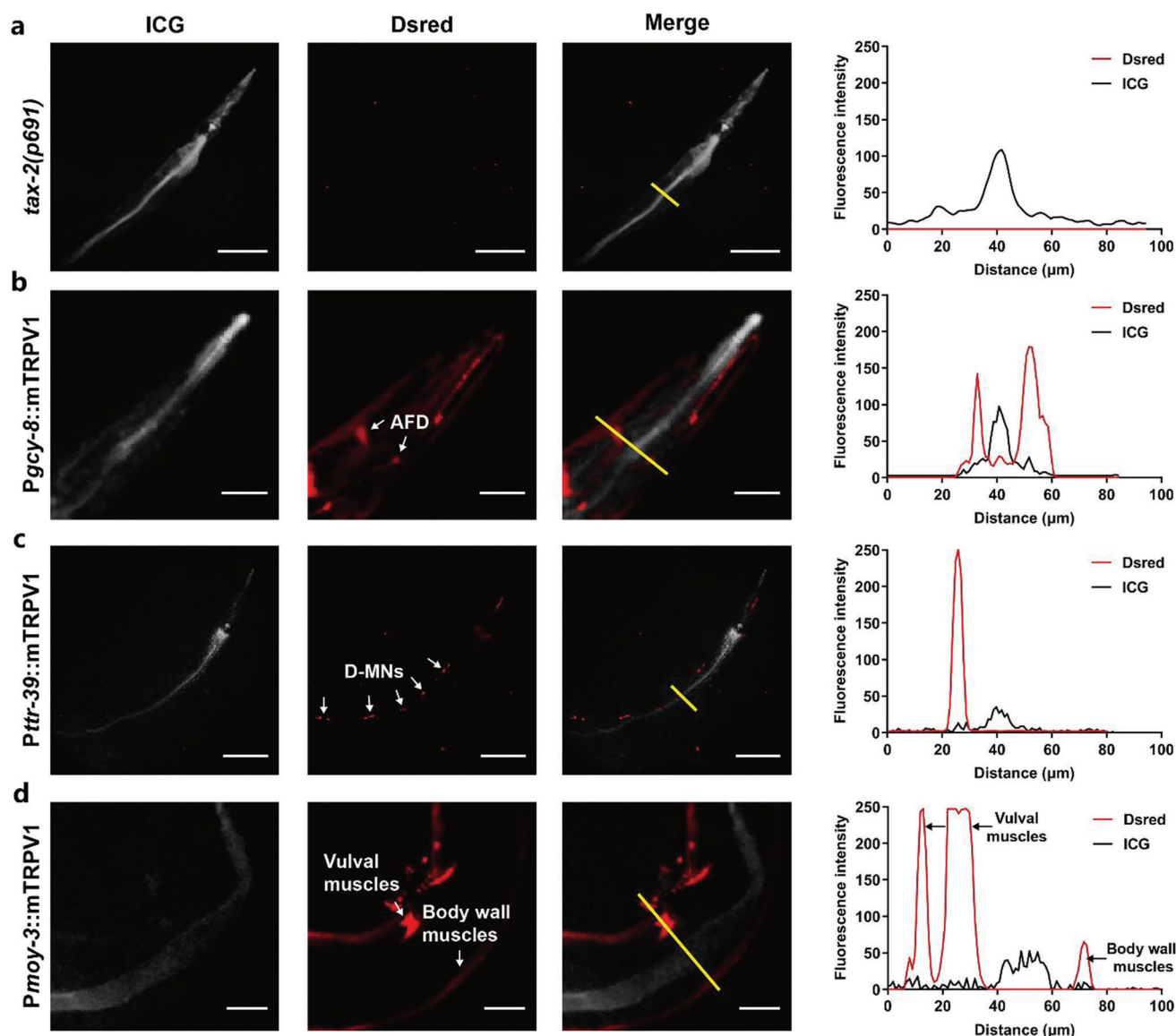


Figure 3. The distribution of ICG ingested by feeding and the expression of mTRPV1 in specific tissue cells in *C. elegans*. Representative two-photon fluorescence images of ICG distribution (gray) after feeding ($2 \mu\text{g mL}^{-1}$, 12 h) and mTRPV1-sl2-DsRed (red) expression in *C. elegans*. a) *tax-2(p691)* was imaged as a control group. mTRPV1-sl2-DsRed were specifically expressed in AFD sensory neurons b), D-class motor neurons c), body wall muscles and vulva muscles d), respectively. Scale bar = $100 \mu\text{m}$ (a,c), $20 \mu\text{m}$ (b), $25 \mu\text{m}$ (d). White arrows, the position of tissue cells. Yellow line in Merge group, the position where fluorescence intensity was determined. Right panel in each row showed fluorescence intensity value along the line (yellow, in merge group) and the distances between mTRPV1 and ICG in each group.

mTRPV1 which be activated by the photothermal stimulation. And applying NIR or ICG alone also did not slow down the swimming behaviors (Figure 5a-b). What's more, the D-MNs regulated thrashing had NIR intensity dependence and ICG dose dependence (Figure 5c-d). These results suggested that NIR irradiation can activate mTRPV1 expressed in D-MNs to excite the motor neurons through photothermal conversion material ICG, and then induce motor behavior changes mediated by the motor neurons. In conclusion, our photothermal system regulates not only the activity of thermosensory neurons, but also the activity of motor neurons and related behaviors.

2.7. NIR Photothermal Modulation of Muscle Cells and Physiological Behaviors in *C. elegans*

So far, our NIR-ICG photothermal manipulation has been effectively applied in nervous system in vivo, then we wondered if it could also be used in other systems to manipulate the excitability of other excitable cells besides neurons in freely behaving animals. To explore the possibility, we expressed mTRPV1 in muscle cells driven by muscular system specific promoter *Pmyo-3* (*Pmyo-3::mTRPV1::sl2::Dsred*). There are two main types of muscle in *C. elegans*: multiple sarcomere/obliquely striated muscles

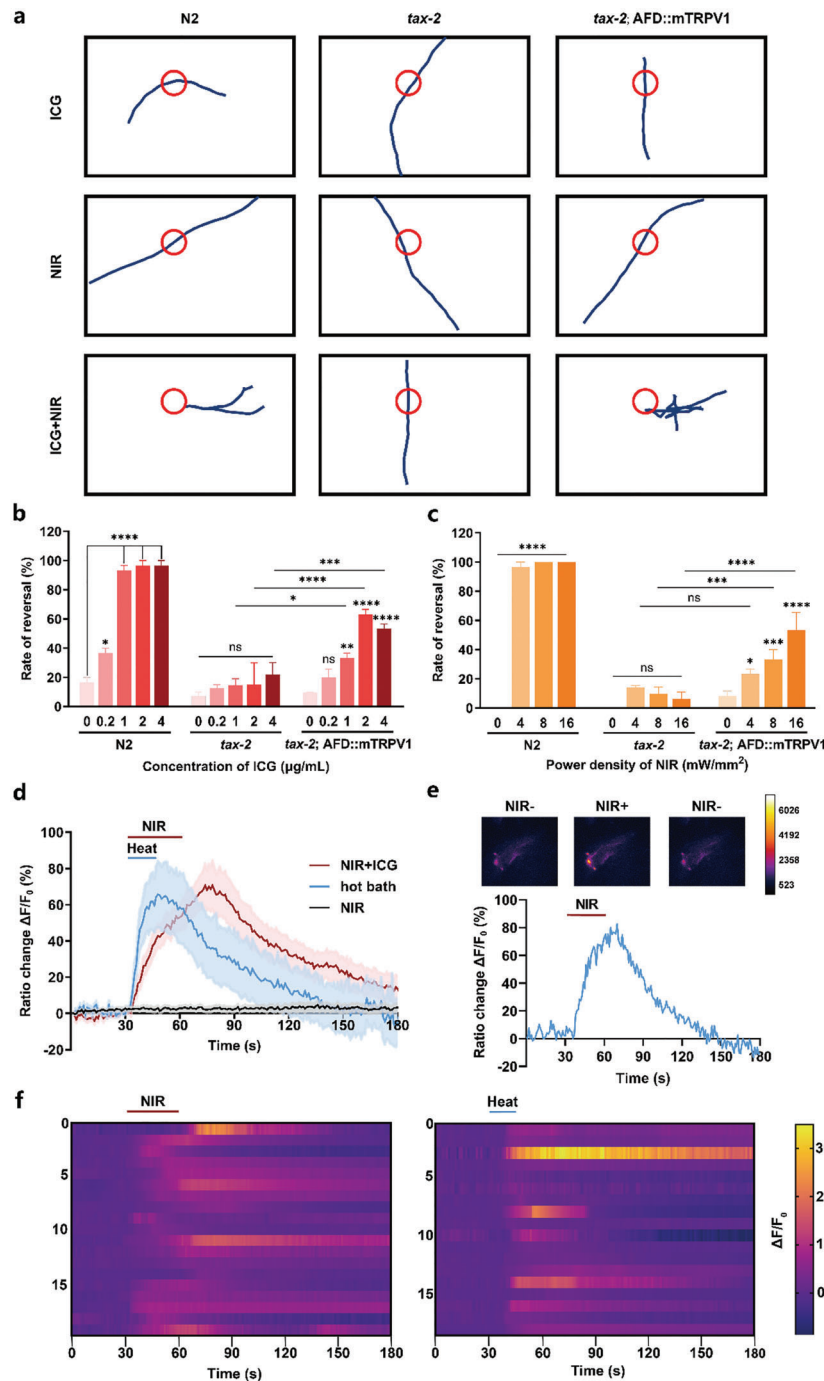


Figure 4. In vivo NIR photothermal modulation of AFD sensory neurons excitability and reversal locomotion. a) Representative track graphs of N2, *tax-2*(*p691*) and *tax-2*;P_{gcy-8}::mTRPV1::sl2::Dsred *C. elegans* strains, when treated with ICG and/or NIR. Also see Video S1 (Supporting Information). b) Quantification of reversal rate under NIR (793 nm, 16 mW mm⁻²) irradiation fed with different concentration of ICG. c) Reversal rate under different power densities of NIR laser irradiation fed with ICG (2 µg mL⁻¹). Each measurement was repeated 3 times, n ≥ 20. Data shown as mean ± SEM. ns, not significant (p > 0.05), * p < 0.05, ** p < 0.01, *** p < 0.001, **** p < 0.0001 by two-way ANOVA. d) Calcium responses of AFD neurons in *tax-2*; AFD::mTRPV1 *C. elegans* upon heating (45 °C, 15 s) or NIR (25 mW mm⁻², 30 s) with/without ICG (10 µg mL⁻¹). e) Representative time-lapse rainbow images of GCaMP5-based calcium responses (up) and soma fluorescence change (down) from an AFD neuron. NIR (25 mW mm⁻²) was applied for 30 s with ICG (10 µg mL⁻¹). f) Representative calcium responses of AFD neurons upon NIR or heating as in (d). The ordinate indicated the number of worms used in the experiments.

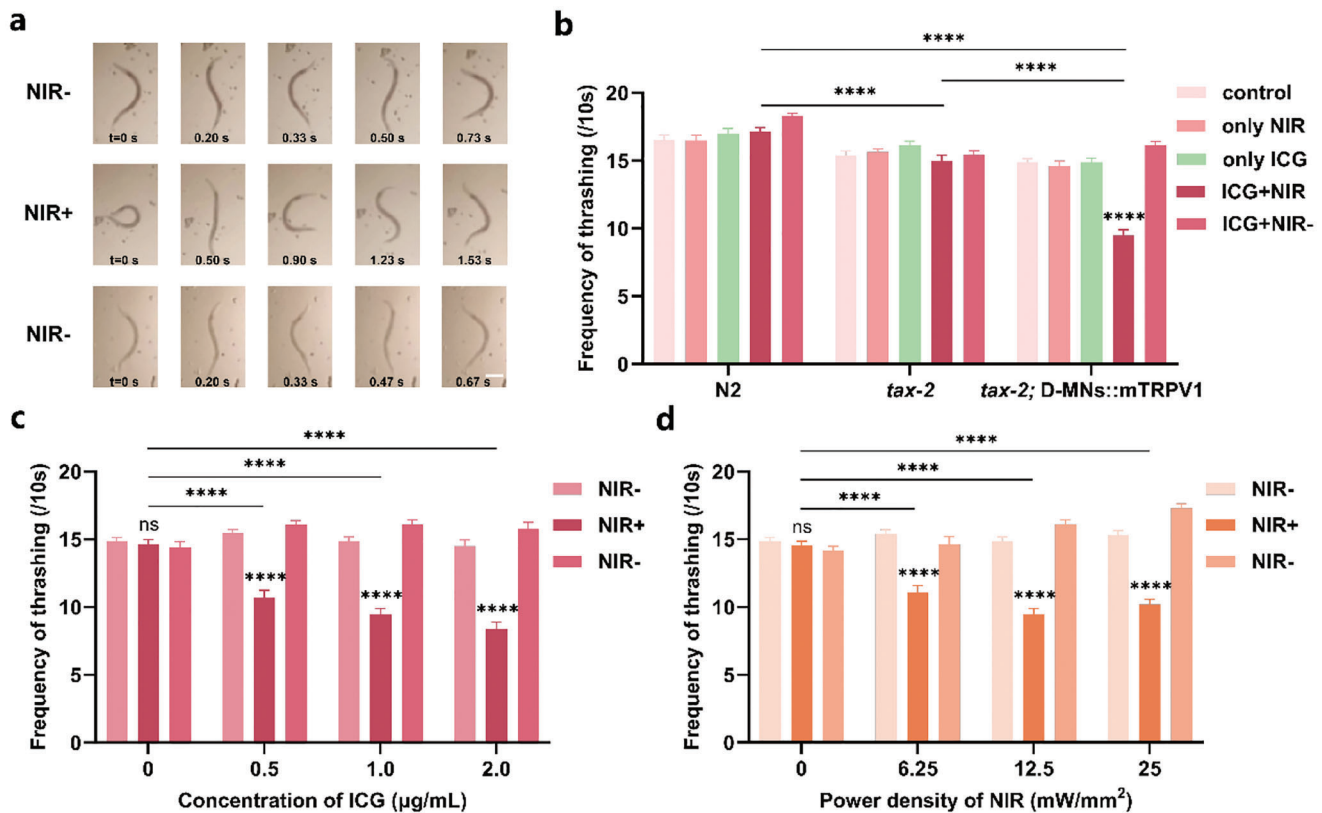


Figure 5. NIR activate D-class motor neurons to reduce thrashing frequency in swimming behavior. a) The series images of thrashing in *tax-2*; D-MNs::mTRPV1 animals before (upper panel NIR-), during (middle panel NIR+) and after (lower panel NIR-) NIR (793 nm, 12.5 mW mm⁻²) illumination, with ICG concentration at 1 µg mL⁻¹ in M9 solution. Thrashing was significantly reduced during NIR illumination. Scale bar = 200 µm. Also see Video S2 (Supporting Information). b) Quantification of thrashing frequency during NIR irradiation in respective genetic backgrounds and experimental conditions. Control: no NIR, no ICG; NIR: 793 nm, 12.5 mW mm⁻², ICG: 1 µg mL⁻¹. n ≥ 34. Data shown as mean ± SEM. ns, not significant (p > 0.05), **** P < 0.0001 by two-way ANOVA. c) Quantification of thrashing frequency in *tax-2*; D-MNs::mTRPV1 animals before (left column NIR-), during (middle column NIR+) and after (right column NIR-) NIR (793 nm, 12.5 mW mm⁻²) illumination, with different concentrations of ICG dissolved in M9 solution. d) Quantification of thrashing frequency in *tax-2*; D-MNs::mTRPV1 animals in the presence of ICG (1 µg mL⁻¹) before (left column NIR-), during (middle column NIR+) and after (right column NIR-) NIR (793 nm) illumination of different intensities. c,d) Data shown as mean ± SEM. n ≥ 35. The NIR+ data were compared with both before and after NIR application. ns, not significant (p > 0.05), **** p < 0.0001 by two-way ANOVA.

and nonstriated muscles.^[61] The 95 striated body wall muscle cells are the functional equivalents of vertebrate skeletal muscles. First, we examined the effects and efficacy of the NIR-ICG photothermal system on body wall muscles. Other studies have shown that activating body wall muscles with drugs or optogenetic tools will cause muscle contraction and induce nematodes to be stiff and paralyzed. As we expected, our photothermal manipulation (200 mW mm⁻² NIR with 10 µg mL⁻¹ ICG) could also induced stiffness and paralysis of *C. elegans* by excited the body wall muscles. And the mTRPV1 expressed worms (also shown as BM::mTRPV1) had a much higher ratio of paralysis compared with N2 worms (Figure 6a). At the same time, the BM::mTRPV1 worms took significantly shorter time to be stiff respond to NIR irradiation (Figure 6b). These results proved the effectiveness of our photothermal system in activating body wall muscles *in vivo*.

Next, we examined its modulatory effect on another type of muscle, the vulva muscles, which belong to the nonstriated muscles and directly regulate egg-laying behavior in *C. elegans*. A young adult hermaphrodite generally has a store of 10–15 eggs

in its uterus at any given time. Increasing the cellular excitability of the vulva muscles can result in muscle contractions, open the vulva and compress the uterus, then allow the eggs to be expelled into the environment.^[62] In our previous study, we successfully used Channelrhodopsin-2 (ChR2) optogenetic tools to activate vulva muscles and induced nematodes egg-laying.^[63] Interestingly, the egg-laying behavior driven by vulva muscles also be triggered by NIR-ICG photothermal system (50 mW mm⁻² NIR with 7.5 µg mL⁻¹ ICG) in mTRPV1 expressed worms (also shown as VM::mTRPV1), but not in N2 worms (Figure 6c-d). And the egg laying could not be stimulated by ICG alone (Figure 6d). So, our photothermal system can modulate not only striated muscles, but also nonstriated muscles *in vivo*.

Collectively, we successfully modulated two types of neurons (AFD sensory neurons and D-MNs motor neurons) and two types of muscles (BM striated muscles and VM nonstriated muscles) through our photothermal system in freely moving animals. As far as we know, it was the first time to achieve precisely photothermal modulation of different types of excitable cells and corresponding behaviors in different systems *in vivo*.

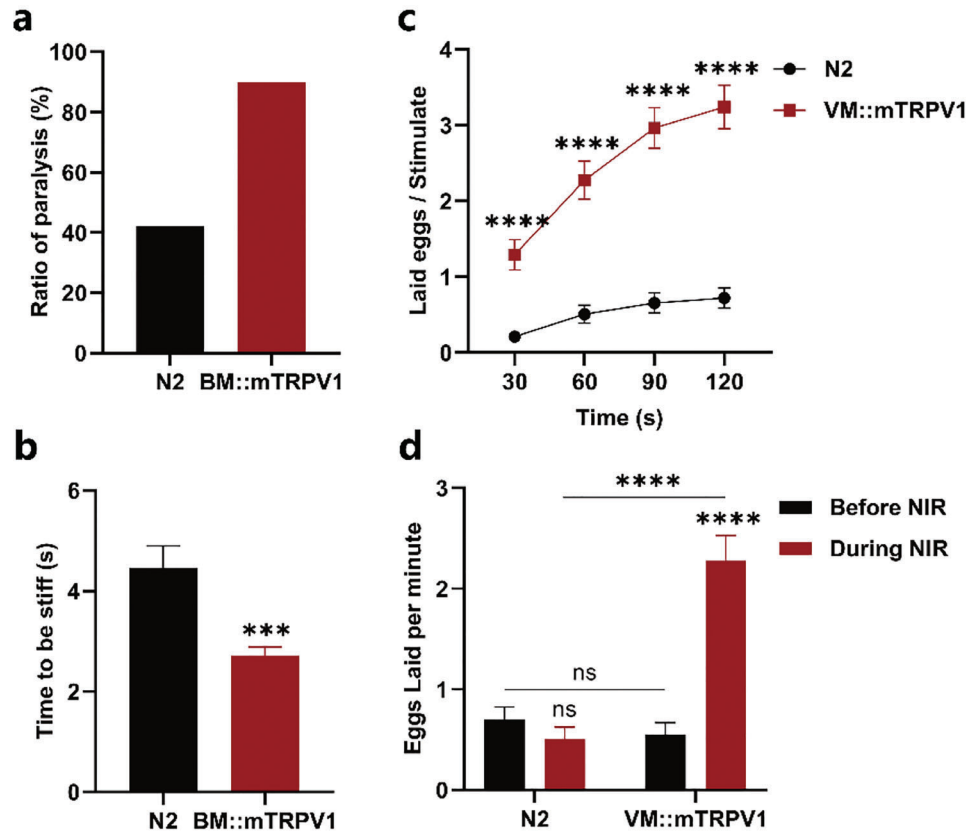


Figure 6. NIR photothermal modulation of paralysis and egg-laying behaviors through mTRPV1 expressed in muscles with ICG. a) Ratio of paralysis in N2 and BM::mTRPV1 animals under NIR (793 nm, 200 mW mm⁻²) illumination for 10 s, with ICG (10 µg mL⁻¹). n ≥ 70. Also see Video S3 (Supporting Information). b) NIR irradiation time required for animals to be stiff. Data shown as mean ± SEM. n ≥ 35. *** p < 0.001 by Welch's t test. c) Time course of laid eggs upon NIR (793 nm, 50 mW mm⁻²) stimulation with ICG concentration at 7.5 µg mL⁻¹. d) The number of eggs laid per min before or during NIR illumination. Also see Video S4 (Supporting Information). c,d) Data shown as mean ± SEM. n ≥ 58. ns, not significant (p > 0.05), **** p < 0.0001 by two-way ANOVA.

2.8. Biological Safety of ICG

ICG is an FDA-approved photothermal agent. It has been largely used in fluorescent imaging and photothermal therapy. In order to widely apply our photothermal manipulation in mammals or other experimental systems, we tested the biological safety of ICG. We incubated nematodes with different concentrations of ICG (up to 10 µg mL⁻¹), then counted the survival rate of the worms after 24 h of feeding. In our experiments, almost all the worms were still alive with ingested ICG (Figure S5a, Supporting Information). To examine the long-term toxicity of ICG, we compared the lifespan and reproduction of *C. elegans* cultured with or without ICG. When worms were continually fed with ICG, the lifespan of adults showed no significant difference compared with the control animals. Interestingly, worms fed with ICG at a concentration of 10 µg mL⁻¹ even had a slight increase in lifespan (Figure S5b, Supporting Information). The reproduction was examined by measuring the number of eggs. We found the nematodes did not exhibit any egg-laying defects when fed with different concentrations of ICG (0, 2, 10 µg mL⁻¹). The number of eggs accumulated in uterus in D2 worms, which represented the ability of egg-laying behavior was almost equal (Figure S5e, Supporting Information). And the number of eggs laid per day

also exhibited no difference (Figure S5c, Supporting Information), showing that ICG did not affect the brood size of the worms (Figure S5d, Supporting Information). These results all demonstrated the high biological safety of ICG.

Taken all together, we developed a 793 nm NIR light irradiation photothermal manipulation system with ICG to regulate cellular excitability in different systems through thermosensitive TRPV1 channel, and mediated corresponding physiological behaviors in vivo (Figure 7).

3. Discussion

Non-invasive neuromodulation techniques have attracted much attention in neuroscience research and disease therapy in recent years. Photothermal modulation offers a new approach to this field. However, due to the lack of research in vivo, most studies and applications were limited to the cellular level. Our study first achieved precise photothermal modulation of different types of excitable cells and related behaviors in freely moving animals with a non-invasive manner.

In our study, by activating the thermosensitive channel TRPV1 under NIR irradiation with photothermal agent ICG, which has excellent photothermal conversion efficiency and biosafety, we

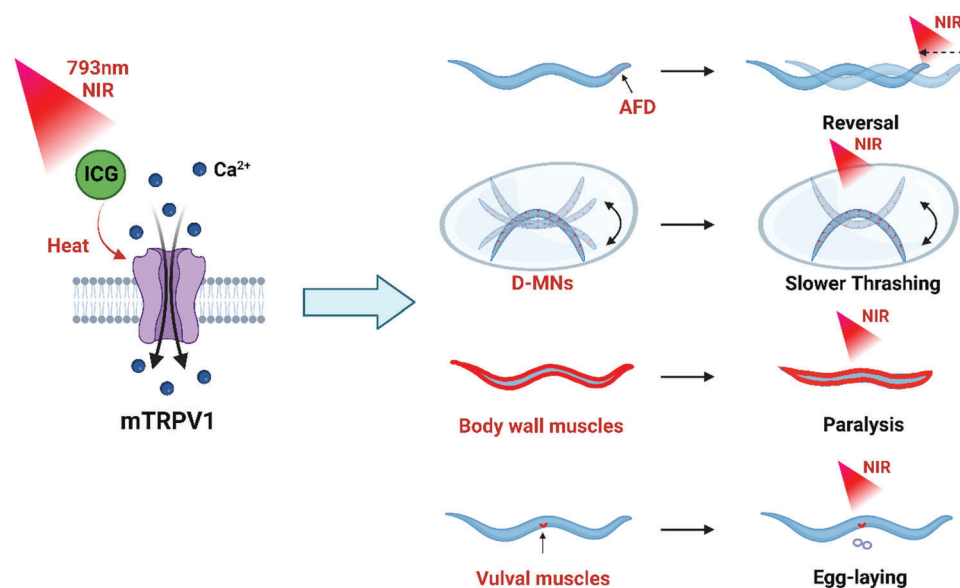


Figure 7. NIR modulates *C. elegans* cellular excitability and animal behaviors through TRPV1 with ICG. NIR light (793 nm) irradiation can activate the thermosensitive TRPV1 channel through photothermal agents ICG to precisely regulate the excitability of different types of cells and related behaviors in *C. elegans* in vivo. Mouse TRPV1 channels are expressed exogenously in AFD sensory neurons, D-class motor neurons (D-MNs), body wall muscles and vulva muscles. In the presence of ICG, NIR illumination effectively activate TRPV1, cause Ca^{2+} influx, lead to increased excitability of tissue cells, and then induce reversal, slower thrashing, paralysis and egg-laying behaviors, respectively.

successfully achieved in vivo precise regulation of the cellular excitability in both nervous and muscular systems, and mediated a variety of related physiological behaviors. In order to fully demonstrated the effectiveness of our photothermal manipulation, we performed multiple experiments including animal behaviors, in vitro and in vivo calcium imaging, wide-field near-infrared fluorescence imaging, two-photon fluorescence imaging, confocal imaging, heat shock assay, biosafety test, and pharmacological assay. After demonstrated TRPV1 expressed HEK293T cells could be activated by NIR stimuli with photothermal agent ICG with a calcium response, we applied our photothermal modulation in *C. elegans* for in vivo detection. In our test, ICG showed widely distribution in *C. elegans* after 12 h of feeding, and performed photothermal conversion response upon NIR stimuli to induce the expression of heat shock protein HSP-4 in vivo. And then we successfully modulated two types of neurons (AFD sensory neurons and D-MNs motor neurons) and two types of muscles (BM striated muscles and VM nonstriated muscles) through NIR stimulation with ICG. We specifically excited these different types of excitable cells and induced reversal locomotion, slower swimming, paralysis and egg-laying behaviors, respectively. In addition, we tested the biosafety of ICG for survival, reproduction and lifespan, and found no negative effect. We developed a non-invasive photothermal manipulation system to regulate cellular excitability in different systems and mediated related physiological behaviors in vivo.

The wavelength of NIR we used in our experiments was 793 nm, which belongs to the range of NIR-I, due to ICG showed the highest absorption peak at this value (Figure 1a). Compared to visible light, NIR-I light exhibits a deeper tissue penetration. Compared to NIR-II light, the NIR-I light shows less water absorption, non-specific thermal effect and hyperthermia effect.

However, it cannot be avoided that NIR-I light possessed relatively lower tissue penetration depth compared to NIR-II, which might hinder deep NIR photothermal manipulation. In our in vivo experiments, the minimum NIR light intensity used was only 4 mW mm^{-2} , and the concentration of ICG just ranged from $0.2 \mu\text{g mL}^{-1}$ to $10 \mu\text{g mL}^{-1}$. Both the NIR light intensity and ICG concentration we applied were at a very low level, almost the lowest values used for cellular activity modulation in vivo. The low light power density and low agent concentration requirement demonstrated the sensitivity and effectiveness of our photothermal manipulation.

There are several NIR stimulated photothermal materials have been synthesized and studied. Such as the semiconducting polymer nanoparticles have been applied to target TRPV1-expressed neuron cells response to NIR stimuli in vitro, or as a cargo encapsulating TRPV1 agonist capsaicin in cancer therapy.^[64,65] The gold nanoparticles packed microcapsules were used to regulate Wnt signaling pathway upon NIR stimuli in *Hydra*.^[37] And $\text{Cu}_2\text{x Se}$ -anti-TRPV1 nanoparticles were used to target the microglia and open TRPV1 channels under NIR irradiation to promote phagocytosis and degradation of $\alpha\text{-syn}$ in PD model.^[66] However, the biosafety of these inorganic or metal nanomaterials still needs to be considered and further tested, which resulting in the research and application of these materials still be limited to the cellular level in vitro. In our study, the photothermal conversion material ICG showed excellent photothermal conversion efficiency compared to these materials, as well as excellent photostability in FBS solution (Figure 1b). ICG showed higher photothermal stability when binding to FBS, because ICG could bind to the hydrophobic region of protein, avoiding aggregation induced quenching effect.^[67,68] Due to the weak photodynamic character of pure ICG, we didn't observe ICG induced ROS production in

C. elegans. Meanwhile, ICG exhibited high biocompatibility and high biosafety performance. Long term continuously fed by ICG had no negative effects on survival, reproduction and lifespan in *C. elegans* (Figure S5, Supporting Information). What's more, worms fed with ICG at a concentration of $10 \mu\text{g mL}^{-1}$ even had a slight increase in lifespan. As an FDA-approved agent, ICG has already been widely used in angiography and photothermal treatment of tumor. And clinical studies have shown that ICG has a short life time in blood circulation, which can be metabolized by the livers. Due to its excellent photothermal conversion efficiency and biosafety, ICG exhibited its advantages in photothermal regulation in vivo.

Recently, some other neural activity modulations by NIR were also performed in behaving animals. Gao's group has applied NIR to manipulate the upconversion nanoparticles (UCNPs) for motor regulation and neuron ablation in *C. elegans*. NIR at 808 nm stimulated Er-UCNPs and specifically controlled Chrimson expressed DVC interneuron and D-class motor neurons.^[32] In addition, they used orthogonal emissive UCNPs excited by dual-NIR illumination (808 and 980 nm) to activate the optogenetic sensor BiPOLES expressed cholinergic motor neurons, which enabled bidirectional control of motor behaviors.^[69] And they also developed an 808 nm NIR light-induced neuron ablation method by simultaneously activating miniSOG and Chrimson based on UCNPs.^[70] Another work needs to be mentioned is made by Hong and Pu's group, TRPV1 ectopically expressed neurons in the hippocampus, motor cortex and ventral tegmental area of mice can be activated upon NIR-II illumination at 1064 nm, with macromolecular transducers consisting of a semi-conducting polymer core and an amphiphilic polymer shell.^[71] However, in both works, only the neurons were modulated. In our study, in addition to in vivo manipulate neural activity and motor behaviors in two different types of neurons, the AFD thermosensitive neurons and the D-class motor neurons, we also successfully performed the NIR photothermal modulation in muscular system. Both the straited muscles (body wall muscle cells, functional equivalent to vertebrate skeletal muscles) and nonstriated muscles (vulva muscles) can be excited by NIR stimuli, induced paralysis and egg-laying behaviors respectively, which verified a broader application of our photothermal manipulation. So far, our approach appears to be the first photothermal modulation method to regulate different types of excitable cells and corresponding behaviors in vivo. In clinical treatment for neurodegenerative diseases and movement disorders (Parkinson's disease, Alzheimer's disease, Huntington's disease, amyotrophic lateral sclerosis, et al.), as well as in sports rehabilitation trainings, direct regulation of neurons often cannot achieve desired therapeutic effect, due to the complexity of neural circuits. Our photothermal manipulation can also regulate muscle cells directly in vivo, providing a new approach for clinical treatment. And the efficacy and specificity of our photothermal manipulation suggest it may also be applied in some other type of excitable cells or in other experimental systems. At the same time, some photothermal heater-thermometer platforms that can simultaneously achieve heating and thermometry have been standardized, which will accelerate the application of photothermal manipulation and therapy.^[72–74]

In conclusion, this study demonstrates a noninvasive and effective method to precisely regulate the excitability of different

types of cells and mediate related animal behaviors in vivo by NIR photothermal manipulation. The approach appears to be the first photothermal modulation method to be applied in both nervous and muscular systems in freely moving animals with a non-invasive manner. And the manipulation system shows excellent effectiveness, specificity and biological safety, suggesting a wide range of application prospect.

4. Experimental Section

Optical and Photothermal Characterization of ICG: The absorption spectra of ICG ($10 \mu\text{g mL}^{-1}$ dissolved in ultrapure water) were measured by a UV-vis-NIR scanning spectrophotometer (UV-2550, Shimadzu Co., Ltd). And the emission spectra were recorded by a PG2000 spectrometer (Ideoaptics Instrumnets). For photothermal efficacy measurement, ICG in FBS solutions (0, 1, 3, 10, 30, 50, and $100 \mu\text{g mL}^{-1}$, $100 \mu\text{L}$) were irradiated by a 793 nm CW laser (Suzhou Rugkuta Optoelectronics Co., Ltd., China) at a power density of 10 mW mm^{-2} . Temperatures were recorded every 15 s by an infrared thermal imaging camera (Ti25, Fluke IR Fusion Technology Inc., USA). For photostability test, $100 \mu\text{g mL}^{-1}$ ICG in FBS or ultrapure water were irradiated by NIR (793 nm, 10 mW mm^{-2}) for 4 min, following with 4 min cooling time. The irradiation and cooling cycles were repeated 5 times. Temperatures were recorded every 30 s by an infrared thermal imaging camera (Ti25, Fluke IR Fusion Technology Inc., USA).

Cell Culture and Transfection: SY5Y neuroblastoma cells were cultured in DMEM/F-12 (Gibco) and HEK293T cell were cultured in DMEM (Gibco), containing 10% Fetal Bovine Serum Premium (PAN, ST30-3302) and 1% Pen Strep-Penicillin Streptomycin (Gibco), maintained at 37°C with 5% CO_2 . Cell transfection was performed using lipofectamine 3000 (Thermo Fisher) with $1.5 \mu\text{g}$ of mouse TRPV1 (mTRPV1) plasmid or $0.2 \mu\text{g}$ mCherry plasmid in 3.5 cm plates.

***C. elegans* Strains and Culture:** Strains were maintained at 20°C on nematode growth medium (NGM) plates seeded with the OP50 strain of *Escherichia coli* under standard conditions,^[75] unless otherwise stated. For ICG-feeding groups, ICG was mixed with *E. coli* to a final diffusion concentration on the plates as needed, then fed nematodes for 12 h before experiments. The N2 Bristol strain of *C. elegans* was used as wild-type. Transgenic lines used in this study include: Ym_ST089 YmIS6[Phsp-4::GFP], Ym_ST055 *tax-2(p691)*, Ym_ST087 *tax-2(p691)*; YmEx27[Pgcy8::mTRPV1::sl2::Dsred+Pgcy8::GCaMP5], Ym_ST198 *tax-2(p691)*; YmEx28[Pttr-39::mTRPV1::sl2::Dsred+Pttr39::GCaMP5], Ym_ST059 YmEx1[Pmyo-3::mTRPV1::sl2::Dsred+Ptmc-2-GCaMPx].

NIR Fluorescence Microscopic Imaging In Vitro: NIR-I fluorescence microscopic imaging of SY5Y neuroblastoma cells were operated on confocal microscopy (STELLARIS 8 FALCON, Leica). NIR-II wide-field fluorescence microscopic imaging of HEK293T cells were operated on NIR-II-MS optical system (Sunnyoptical). The cells were incubated with ICG ($50 \mu\text{g mL}^{-1}$) in HBSS solution for 1 h. The extra ICG was washed away or just left while imaging.

Confocal Imaging of *C. elegans*: The NaN_3 anesthetized young adult *C. elegans* were immobilized on a glass slide with an agar pad. After cover the agar pad with a coverslip, the fluorescence signals were recorded using Z axis scanning mode by a confocal microscope (FV1000, Olympus) with a Plan-Apochromatic 20 \times (Figure 2a,c) or 60 \times (Figure S4, Supporting Information) objective.

Two-photon Fluorescence Imaging of *C. elegans*: Worms were fed with ICG (0, 0.2, 1, $2 \mu\text{g mL}^{-1}$) for 12 h, then anesthetized and immobilized as described before. The images were taken by a two-photon fluorescence scanning microscope (Olympus, FV1200). A 1040 nm femtosecond (fs) laser (150 fs, 50 MHz) was introduced as excitation source. The signal of DsRed fluorescent probe was recorded by inner photomultiplier tube (PMT), while the fluorescence of ICG was collected by an outer photomultiplier tube (PMT, H7422-50, Hamamatsu) through NDD mode using a 750 nm long-pass filter.

Calcium Imaging: HEK293T cells were incubated with calcium indicator Fluo-8am for 30 min at 37°C in the dark. Cells transfected with

mTRPV1-mCherry or mCherry only were used to detect the fluorescence intensity changes under heat, capsaicin or NIR treatments. The heating process was controlled by perfusing preheated bath solution at 45 °C. And then 10 μM capsaicin was given after 5.5 min. The optical fiber was used to lead the light source of NIR stimulation (793 nm, 10 mW mm⁻²) to detect photothermal effect. HEK293T cells in ICG group were incubated with 50 μg mL⁻¹ ICG for 1 h. After washing twice with HBSS, Fluo-8am was added for incubation. The extracellular solution (ECS) for cell calcium imaging contained 140 mM NaCl, 5 mM KCl, 1.2 mM MgSO₄, 1.5 mM CaCl₂, 10 mM HEPES, 10 mM D-glucose, and pH 7.4.

For calcium imaging *in vivo*, AFD::GCaMP5 expressed young adult *C. elegans* were immobilized with surgical glue (Gluturo Topical Tissue Adhesive, Abbott Laboratories) on a glass pad, covered with bath solution (145 mM NaCl, 2.5 mM KCl, 1 mM MgCl₂, 5 mM CaCl₂, 10 mM HEPES, 20 mM glucose, 325~335 mOsm, pH 7.3). Heat stimulation was performed by perfusing preheated bath solution at 45 °C. The worms in the NIR+ICG group were fed with 10 μg mL⁻¹ ICG for 12 h and covered in a bath solution with 10 μg mL⁻¹ ICG when recording. The optical fiber was used to lead the light source of NIR stimulation (793 nm, 10 mW mm⁻²). Calcium imaging was acquired on an inverted microscope (Olympus IX71) with a 40× objective lens. Raw images were acquired with a QImaging optiMOS Scientific CMOS (sCMOS) camera controlled by the micro-Manager 1.4 software. All image stacks were analyzed using the ImageJ software.

Optical System for Photothermal Manipulating of *C. elegans* Behaviors *In Vivo*: The optical system was based on a stereomicroscope (SZN71 Sunnyoptical). 793 nm CW laser was focused on the plate through a focus lens (focus length = 160 mm) and control the spot diameter of 2 mm or as needed. The behavior changes of *C. elegans* was recorded by a VIS CCD (RETIGA-SRV, QImaging) with a white LED illumination.

Heat Shock of *C. elegans*: A total of 100 adult worms of YmIs6[Phsp-4::GFP] were placed on a seeded NGM plate to lay eggs for 2 hours, and the eggs were cultured at 20 °C until the young adult stage. For the heat group, enough nematodes were transferred to fresh NGM plates. Then the plates were heated in water bath at 33 °C for 0, 1, 10, 30 min, respectively. For the NIR+ICG group, nematodes were incubated on fresh NGM plates with ICG (10 μg mL⁻¹) for 12 h to get the young adult stage. Then transferred enough nematodes to M9 droplets with ICG (10 μg mL⁻¹) on glass pads. 793 nm CW laser was focused on the droplets for 0, 1, 5, 10 min, respectively. Fluorescence intensity was detected 2 h after treatment. Worms were anesthetized and immobilized as described before. Imaging was performed using an upright fluorescence microscope (Olympus, BX51WI) with a 5× objective lens (Figure 2d,e). Raw images were acquired with a QImaging optiMOS Scientific CMOS (sCMOS) camera controlled by the micro-Manager 1.4 software. All image stacks were analyzed using the ImageJ software.

Reversal Assay: After fed with different concentrations of ICG for 12 h, young adult *C. elegans* were transferred to a fresh test plate without *Escherichia coli* food on it. After a few minutes of acclimatization, NIR irradiation (793 nm) was performed with different power densities as stated. The NIR spot with a diameter less than 2 mm was placed in front of the *C. elegans* when the worm moved forward. The response behaviors when worms moved into the NIR spot were recorded and classified as go forward and go backward (reversal behavior). A stereoscope (SZN71 Sunnyoptical) equipped with a high-sensitivity digital CCD camera (RETIGA-SRV-Qimaging, Fast1394) was used for recording.

Thrashing Assay: M9 solution with different concentrations of ICG were dropped (50 μL each) on glass pads. Young adult nematodes fed by the equal concentration of ICG were transferred into the droplets to acclimate for ≈1~2 min. Then thrashing behaviors were recorded by a digital camera. For NIR irradiation experiments, animals were first recorded for 20 s as a baseline value, then illuminated under 793 nm NIR light for 20 s to detect the effect of photothermal stimulation, finally recorded for another 20 s after removing NIR to examine the recovery of swimming behaviors.

Paralysis Assay: Young adult worms fed by ICG (10 μg mL⁻¹, 12 h) were transferred to a fresh plate without *E. coli* food on it. After a few minutes of acclimatization, the NIR (793 nm, 200 mW mm⁻²) light was placed onto the body of the nematodes. The motor behaviors upon NIR were recorded

and classified as movement and paralysis. And the NIR irradiation time (within 10 s) required for animals to be stiff was also be counted.

Egg-Laying Assay: For the egg-laying behavior test under photothermal manipulation, nematodes in D2 stage which have been fed by 7.5 μg mL⁻¹ ICG were transferred to fresh NGM plates with ICG. After a few minutes of acclimatization, laid eggs by each worm before or during NIR irradiation (793 nm, 50 mW/mm²) were recorded by a digital camera (Figure 6c-d). For biological safety test of ICG, the effects on reproduction were examined by counting the number of eggs laid per day by each worm in the whole life, and the unlayed eggs in D2 animals, respectively. Worms were incubated on NGM plates with different concentrations of ICG (0, 2, 10 μg mL⁻¹), single worm on single plate. Then the worms were transferred to fresh ICG plates every day after D1 stage, until the egg-laying physiological behavior was over. The number of eggs laid per day was recorded and manually counted (Figure S5c, Supporting Information), and the number of progeny was calculated by accumulating all data (Figure S5c, Supporting Information). For egg retention assays, individual D2 worm was dissolved in a 10 μL droplet of 50% NaOCl solution and the number of retained eggs was counted after 5 min.

Lethality Assay: ICG at different concentrations was added to NGM plates mixed with *E. coli*. After dry for 1–2 h at room temperature, the L4 larva were allowed to transfer onto the plates. Number of dead worms was recorded after 24 h incubation and the viability rate of *C. elegans* was estimated after 3 times repetition.

Lifespan Analysis: For biological safety test of ICG, the effects on lifespan were performed by counting the number of survival nematodes cultured on NGM plates at 20 °C with different concentrations of ICG (0, 2, 10 μg mL⁻¹) until all tested animals were dead. Every 15~20 N2 worms at L4 stage were cultured on a 6 cm NGM plate with ICG, and needed to be transferred to a fresh plate every day in egg-laying period. The survival number was recorded from D1 stage. And the nematodes lost or died accidentally due to crawling off or drilling into the NGM plates were removed out from the test. The number of valid worms was more than 110 in each group.

Quantification and Statistical Analysis: All statistical tests in this study were performed using GraphPad Prism 8. Student's t test, or one- or two-way ANOVA were performed to determine statistical significance. If the variances were significantly different, the Welch's t test or Brown-Forsythe and Welch ANOVA tests were used. P values below 0.05 were considered significant. Data were presented as mean ± SEM. Details of the statistical analyses performed for each figure were provided in the figure legends.

Supporting Information

Supporting Information is available from the Wiley Online Library or from the author.

Acknowledgements

S.Z., M.H., J.F., and S.P. contributed equally to this work. This research was supported by the National Natural Science Foundation of China (82030108 to W.Y.) and the MOE Frontier Science Center for Brain Science & Brain-Machine Integration, Zhejiang University. The authors were grateful to the Core Facilities of Zhejiang University Institute of Neuroscience for technical assistance. The authors thank Shangbang Gao and Suhong Xu for their generous gifts of the plasmid and *C. elegans* strains.

Conflict of Interest

The authors declare no conflict of interest.

Data Availability Statement

The data that support the findings of this study are available from the corresponding author upon reasonable request.

Keywords

animal behavior, *Caenorhabditis elegans*, cellular excitability, near-infrared (NIR) light, TRPV1

Received: July 9, 2023
Revised: August 12, 2023
Published online:

- [1] L. Fenno, O. Yizhar, K. Deisseroth, *Annu. Rev. Neurosci.* **2011**, *34*, 389.
- [2] E. S. Boyden, F. Zhang, E. Bamberg, G. Nagel, K. Deisseroth, *Nat. Neurosci.* **2005**, *8*, 1263.
- [3] V. Gradinaru, M. Mogri, K. R. Thompson, J. M. Henderson, K. Deisseroth, *Science* **2009**, *324*, 354.
- [4] N. C. Klapoetke, Y. Murata, S. S. Kim, S. R. Pulver, A. Birdsey-Benson, Y. K. Cho, T. K. Morimoto, A. S. Chuong, E. J. Carpenter, Z. Tian, J. Wang, Y. Xie, Z. Yan, Y. Zhang, B. Y. Chow, B. Surek, M. Melkonian, V. Jayaraman, M. Constantine-Paton, G. K. Wong, E. S. Boyden, *Nat. Methods* **2014**, *11*, 338.
- [5] J. L. Gomez, J. Bonaventura, W. Lesniak, W. B. Mathews, P. Sysa-Shah, L. A. Rodriguez, R. J. Ellis, C. T. Richie, B. K. Harvey, R. F. Dannals, M. G. Pomper, A. Bonci, M. Michaelides, *Science* **2017**, *357*, 503.
- [6] G. M. Alexander, S. C. Rogan, A. I. Abbas, B. N. Armbruster, Y. Pei, J. A. Allen, R. J. Nonneman, J. Hartmann, S. S. Moy, M. A. Nicoletis, J. O. McNamara, B. L. Roth, *Neuron* **2009**, *63*, 27.
- [7] C. J. Magnus, P. H. Lee, J. Bonaventura, R. Zemla, J. L. Gomez, M. H. Ramirez, X. Hu, A. Galvan, J. Basu, M. Michaelides, S. M. Sternson, *Science* **2019**, *364*, eaav5282.
- [8] G. V. Goddard, D. C. McIntyre, C. K. Leech, *Exp Neurol* **1969**, *25*, 295.
- [9] H. S. Mayberg, A. M. Lozano, V. Voon, H. E. McNeely, D. Seminowicz, C. Hamani, J. M. Schwab, S. H. Kennedy, *Neuron* **2005**, *45*, 651.
- [10] B. D. Greenberg, L. A. Gabriels, D. A. Malone, Jr., A. R. Rezaei, G. M. Friehs, M. S. Okun, N. A. Shapira, K. D. Foote, P. R. Cosyns, C. S. Kubu, P. F. Malloy, S. P. Salloway, J. E. Giftakis, M. T. Rise, A. G. Machado, K. B. Baker, P. H. Stypulkowski, W. K. Goodman, S. A. Rasmussen, B. J. Nuttin, *Mol. Psychiatry* **2010**, *15*, 64.
- [11] N. Grossman, D. Bono, N. Dedic, S. B. Kodandaramaiah, A. Rudenko, H. J. Suk, A. M. Cassara, E. Neufeld, N. Kuster, L. H. Tsai, A. Pascual-Leone, E. S. Boyden, *Cell* **2017**, *169*, 1029.
- [12] G. T. Clement, K. Hynynen, *Phys Med Biol* **2002**, *47*, 1219.
- [13] Y. Tufail, A. Matyushov, N. Baldwin, M. L. Tauchmann, J. Georges, A. Yoshihiro, S. I. Tillery, W. J. Tyler, *Neuron* **2010**, *66*, 681.
- [14] D. Folloni, L. Verhagen, R. B. Mars, E. Fouragnan, C. Constans, J. F. Aubry, M. F. S. Rushworth, J. Sallet, *Neuron* **2019**, *101*, 1109.
- [15] X. Hou, Z. Qiu, Q. Xian, S. Kala, J. Jing, K. F. Wong, J. Zhu, J. Guo, T. Zhu, M. Yang, L. Sun, *Adv. Sci. (Weinh)* **2021**, *8*, 2101934.
- [16] R. Chen, G. Romero, M. G. Christiansen, A. Mohr, P. Anikeeva, *Science* **2015**, *347*, 1477.
- [17] H. Huang, S. Delikanli, H. Zeng, D. M. Ferkey, A. Pralle, *Nat. Nanotechnol.* **2010**, *5*, 602.
- [18] R. Munshi, S. M. Qadri, Q. Zhang, I. Castellanos Rubio, P. Del Pino, A. Pralle, *Elife* **2017**, *6*, e27069.
- [19] S. A. Stanley, L. Kelly, K. N. Latcha, S. F. Schmidt, X. Yu, A. R. Nectow, J. Sauer, J. P. Dyke, J. S. Dordick, J. M. Friedman, *Nature* **2016**, *531*, 647.
- [20] X. Gong, D. Mendoza-Halliday, J. T. Ting, T. Kaiser, X. Sun, A. M. Bastos, R. D. Wimmer, B. Guo, Q. Chen, Y. Zhou, M. Pruner, C. W. Wu, D. Park, K. Deisseroth, B. Barak, E. S. Boyden, E. K. Miller, M. M. Halassa, Z. Fu, G. Bi, R. Desimone, G. Feng, *Neuron* **2020**, *107*, 197.
- [21] F. Zhang, A. M. Aravanis, A. Adamantidis, L. de Lecea, K. Deisseroth, *Nat. Rev. Neurosci.* **2007**, *8*, 577.
- [22] S. K. Kalia, T. Sankar, A. M. Lozano, *Curr. Opin. Neurol.* **2013**, *26*, 374.
- [23] M. H. Histed, V. Bonin, R. C. Reid, *Neuron* **2009**, *63*, 508.
- [24] S. Ibsen, A. Tong, C. Schutt, S. Esener, S. H. Chalasani, *Nat. Commun.* **2015**, *6*, 8264.
- [25] M. Duque, C. A. Lee-Kubli, Y. Tufail, U. Magaram, J. Patel, A. Chakraborty, J. Mendoza Lopez, E. Edsinger, A. Vasan, R. Shiao, C. Weiss, J. Friend, S. H. Chalasani, *Nat. Commun.* **2022**, *13*, 600.
- [26] J. Ye, S. Tang, L. Meng, X. Li, X. Wen, S. Chen, L. Niu, X. Li, W. Qiu, H. Hu, M. Jiang, S. Shang, Q. Shu, H. Zheng, S. Duan, Y. Li, *Nano Lett.* **2018**, *18*, 4148.
- [27] Y. S. Huang, C. H. Fan, N. Hsu, N. H. Chiu, C. Y. Wu, C. Y. Chang, B. H. Wu, S. R. Hong, Y. C. Chang, A. Yan-Tang Wu, V. Guo, Y. C. Chiang, W. C. Hsu, L. Chen, C. Pin-Kuang Lai, C. K. Yeh, Y. C. Lin, *Nano Lett.* **2020**, *20*, 1089.
- [28] Z. Qiu, J. Guo, S. Kala, J. Zhu, Q. Xian, W. Qiu, G. Li, T. Zhu, L. Meng, R. Zhang, H. C. Chan, H. Zheng, L. Sun, *iScience* **2019**, *21*, 448.
- [29] C. Rabut, S. Yoo, R. C. Hurt, Z. Jin, H. Li, H. Guo, B. Ling, M. G. Shapiro, *Neuron* **2020**, *108*, 93.
- [30] Z. Feng, T. Tang, T. Wu, X. Yu, Y. Zhang, M. Wang, J. Zheng, Y. Ying, S. Chen, J. Zhou, X. Fan, D. Zhang, S. Li, M. Zhang, J. Qian, *Light Sci Appl* **2021**, *10*, 197.
- [31] A. M. Smith, M. C. Mancini, S. Nie, *Nat. Nanotechnol.* **2009**, *4*, 710.
- [32] Y. Ao, K. Zeng, B. Yu, Y. Miao, W. Hung, Z. Yu, Y. Xue, T. T. Y. Tan, T. Xu, M. Zhen, X. Yang, Y. Zhang, S. Gao, *ACS Nano* **2019**, *13*, 3373.
- [33] S. Chen, A. Z. Weitemier, X. Zeng, L. He, X. Wang, Y. Tao, A. J. Y. Huang, Y. Hashimoto-dani, M. Kano, H. Iwasaki, L. K. Parajuli, S. Okabe, D. B. L. Teh, A. H. All, I. Tsutsui-Kimura, K. F. Tanaka, X. Liu, T. J. McHugh, *Science* **2018**, *359*, 679.
- [34] A. H. All, X. Zeng, D. B. L. Teh, Z. Yi, A. Prasad, T. Ishizuka, N. Thakor, Y. Hiromu, X. Liu, *Adv. Mater.* **2019**, *31*, 1803474.
- [35] J. Yang, J. Choi, D. Bang, E. Kim, E. K. Lim, H. Park, J. S. Suh, K. Lee, K. H. Yoo, E. K. Kim, Y. M. Huh, S. Haam, *Angew Chem Int Edit* **2011**, *50*, 441.
- [36] Z. B. Zha, X. L. Yue, Q. S. Ren, Z. F. Dai, *Adv. Mater.* **2013**, *25*, 777.
- [37] A. Ambrosone, V. Marchesano, S. Carregal-Romero, D. Intartaglia, W. J. Parak, C. Tortiglione, *ACS Nano* **2016**, *10*, 4828.
- [38] C. A. Poland, R. Duffin, I. Kinloch, A. Maynard, W. A. H. Wallace, A. Seaton, V. Stone, S. Brown, W. MacNee, K. Donaldson, *Nat. Nanotechnol.* **2008**, *3*, 423.
- [39] K. Yang, S. A. Zhang, G. X. Zhang, X. M. Sun, S. T. Lee, Z. A. Liu, *Nano Lett.* **2010**, *10*, 3318.
- [40] R. F. Zhang, F. Yan, Y. Chen, *Adv. Sci.* **2018**, *5*, 1801175.
- [41] B. Li, H. Liu, Y. He, M. Zhao, C. Ge, M. R. Younis, P. Huang, X. Chen, J. Lin, *Angew Chem Int Ed Engl* **2022**, *61*, e202200025.
- [42] J. Yu, D. Javier, M. A. Yaseen, N. Nitin, R. Richards-Kortum, B. Anvari, M. S. Wong, *J. Am. Chem. Soc.* **2010**, *132*, 1929.
- [43] E. P. Porcu, A. Salis, E. Gavini, G. Rassu, M. Maestri, P. Giunchedi, *Biotechnol. Adv.* **2016**, *34*, 768.
- [44] L. Luo, L. Yan, A. Amirshaghghi, Y. Wei, T. You, S. Singhal, A. Tsourkas, Z. Cheng, *ACS Appl. Bio Mater.* **2020**, *3*, 2344.
- [45] J. T. Alander, I. Kaartinen, A. Laakso, T. Patila, T. Spillmann, V. V. Tuchin, M. Venermo, P. Valisuo, *Int. J. Biomed. Imaging* **2012**, *2012*, 1.
- [46] T. Kaletta, M. O. Hengartner, *Nat Rev Drug Discov* **2006**, *5*, 387.
- [47] W. R. Schafer, *Curr. Biol.* **2005**, *15*, R723.
- [48] M. J. Caterina, M. A. Schumacher, M. Tominaga, T. A. Rosen, J. D. Levine, D. Julius, *Nature* **1997**, *389*, 816.
- [49] M. J. Caterina, A. Leffler, A. B. Malmberg, W. J. Martin, J. Trafton, K. R. Petersen-Zeit, M. Koltzenburg, A. I. Basbaum, D. Julius, *Science* **2000**, *288*, 306.
- [50] V. Prahlad, T. Cornelius, R. I. Morimoto, *Science* **2008**, *320*, 811.
- [51] M. Al-Amin, I. Kawasaki, J. Gong, Y. H. Shim, *Mol. Cells* **2016**, *39*, 163.
- [52] M. Beverly, S. Anbil, P. Sengupta, *J. Neurosci.* **2011**, *31*, 11718.
- [53] D. Ramot, B. L. MacLinnis, M. B. Goodman, *Nat. Neurosci.* **2008**, *11*, 908.

- [54] H. Komatsu, I. Mori, J. S. Rhee, N. Akaike, Y. Ohshima, *Neuron* **1996**, 17, 707.
- [55] A. Takeishi, Y. V. Yu, V. M. Hapiak, H. W. Bell, T. O'Leary, P. Sengupta, *Neuron* **2016**, 90, 235.
- [56] A. Kuhara, N. Ohnishi, T. Shimowada, I. Mori, *Nat. Commun.* **2011**, 2, 355.
- [57] L. Luo, N. Cook, V. Venkatachalam, L. A. Martinez-Velazquez, X. Zhang, A. C. Calvo, J. Hawk, B. L. MacInnis, M. Frank, J. H. Ng, M. Klein, M. Gershow, M. Hammarlund, M. B. Goodman, D. A. Colon-Ramos, Y. Zhang, A. D. Samuel, *Proc Natl Acad Sci U S A* **2014**, 111, 2776.
- [58] Y. Tsukada, M. Yamao, H. Naoki, T. Shimowada, N. Ohnishi, A. Kuhara, S. Ishii, I. Mori, *J. Neurosci.* **2016**, 36, 2571.
- [59] S. L. McIntire, E. Jorgensen, J. Kaplan, H. R. Horvitz, *Nature* **1993**, 364, 337.
- [60] J. E. Richmond, E. M. Jorgensen, *Nat. Neurosci.* **1999**, 2, 791.
- [61] K. Gieseler, H. Qadota, G. M. Benian, *WormBook* **2017**, 2017, 1.
- [62] W. R. Schafer, *C. elegans biology* **2005**, 1.
- [63] X. Yue, J. Zhao, X. Li, Y. Fan, D. Duan, X. Zhang, W. Zou, Y. Sheng, T. Zhang, Q. Yang, J. Luo, S. Duan, R. Xiao, L. Kang, *Neuron* **2018**, 97, 571.
- [64] Y. Lyu, C. Xie, S. A. Chechetka, E. Miyako, K. Pu, *J. Am. Chem. Soc.* **2016**, 138, 9049.
- [65] X. Zhen, C. Xie, Y. Jiang, X. Ai, B. Xing, K. Pu, *Nano Lett.* **2018**, 18, 1498.
- [66] J. Yuan, H. Liu, H. Zhang, T. Wang, Q. Zheng, Z. A.-O. Li, *Adv. Mater.* **2022**, 34, 2108435.
- [67] A. C. Bhasikuttan, J. Mohanty, W. M. Nau, H. Pal, *Angew Chem Int Ed Engl* **2007**, 46, 4120.
- [68] M. S. Baptista, G. L. Indig, *J. Phys. Chem. B* **1998**, 102, 4678.
- [69] J. Guo, L. Chen, F. Xiong, Y. Zhang, R. Wang, X. Zhang, Q. Wen, S. Gao, Y. Zhang, *Nanoscale* **2023**, 15, 7845.
- [70] Y. Zhang, W. Zhang, K. Zeng, Y. Ao, M. Wang, Z. Yu, F. Qi, W. Yu, H. Mao, L. Tao, C. Zhang, T. T. Y. Tan, X. Yang, K. Pu, S. Gao, *Small (Weinheim an der Bergstrasse Germany)* **2020**, 16, 1906797.
- [71] X. Wu, Y. Jiang, N. J. Rommelfanger, F. Yang, Q. Zhou, R. Yin, J. Liu, S. Cai, W. Ren, A. Shin, K. S. Ong, K. Pu, G. Hong, *Nat. Biomed. Eng.* **2022**, 6, 754.
- [72] E. Carrasco, B. del Rosal, F. Sanz-Rodriguez, A. J. de la Fuente, P. H. Gonzalez, U. Rocha, K. U. Kumar, C. Jacinto, J. G. Sole, D. Jaque, *Adv. Funct. Mater.* **2015**, 25, 615.
- [73] Y. K. Wu, M. N. A. Alam, P. Balasubramanian, A. Ermakova, S. Fischer, H. Barth, M. Wagner, M. Raabe, F. Jelezko, T. Weil, *Nano Lett.* **2021**, 21, 3780.
- [74] Ferdinandus, M. Suzuki, C. Q. Vu, Y. Harada, S. R. Sarker, S. Ishiwata, T. Kitaguchi, S. Arai, *ACS Nano* **2022**, 16, 9004.
- [75] S. Brenner, *Genetics* **1974**, 77, 71.



310012

杭州市西湖区天目山路 46 号宁波大厦 1301 室 杭州中成专利事务所
有限公司
朱莹莹(17764577667)

发文日:

2023 年 04 月 25 日



申请号: 202310454120.8

发文序号: 2023042501688590

专利申请受理通知书

根据专利法第 28 条及其实施细则第 38 条、第 39 条的规定, 申请人提出的专利申请已由国家知识产权局受理。现将确定的申请号、申请日等信息通知如下:

申请号: 2023104541208

申请日: 2023 年 04 月 25 日

申请人: 浙江大学

发明人: 杨巍, 钱骏, 岳晓敏, 庄斯宜, 何木斌, 冯佳琪, 张宜

发明创造名称: 一种操控线虫特定神经元和肌肉细胞兴奋性的方法及其装置

经核实, 国家知识产权局确认收到文件如下:

权利要求书 1 份 2 页, 权利要求项数: 10 项

说明书 1 份 7 页

说明书附图 1 份 4 页

说明书摘要 1 份 1 页

发明专利请求书 1 份 5 页

实质审查请求书 文件份数: 1 份

申请方案卷号: 23-212069-00069613

提示:

1. 申请人收到专利申请受理通知书之后, 认为其记载的内容与申请人所提交的相应内容不一致时, 可以向国家知识产权局请求更正。

2. 申请人收到专利申请受理通知书之后, 再向国家知识产权局办理各种手续时, 均应当准确、清晰地写明申请号。

审查员: 自动受理

联系电话: 010-62356655

审查部门: 初审及流程管理部



200101
2022.10

纸件申请, 回函请寄: 100088 北京市海淀区蓟门桥西土城路 6 号 国家知识产权局专利局受理处收
电子申请, 应当通过专利业务办理系统以电子文件形式提交相关文件。除另有规定外, 以纸件等其他形式提交的文件视为未提交。



项目批准号	61975172
申请代码	F051201
归口管理部门	
依托单位代码	31005808A1112-2096



61975172 1005706

国家自然科学基金委员会 资助项目计划书

资助类别：面上项目

亚类说明：

附注说明：

项目名称：CW光激发的ICG近红外反斯托克斯荧光特性及其活体功能应用

直接费用：63万元 执行年限：2020.01-2023.12

负责人：钱骏

通讯地址：浙江大学紫金港校区东五教学楼光及电磁波研究中心219房间

邮政编码：310058 电 话：0571-88206515转215

电子邮件：qianjun@zju.edu.cn

依托单位：浙江大学

联系人：薛建龙 电 话：0571-88981080

填表日期：2019年08月17日

国家自然科学基金委员会制



国家自然科学基金委员会资助项目计划书填报说明

- 一、项目负责人收到《关于国家自然科学基金资助项目批准及有关事项的通知》（以下简称《批准通知》）后，请认真阅读本填报说明，参照国家自然科学基金相关项目管理办法及《国家自然科学基金资助项目资金管理办法》（请查阅国家自然科学基金委员会官方网站首页“政策法规”栏目），按《批准通知》的要求认真填写和提交《国家自然科学基金委员会资助项目计划书》（以下简称《计划书》）。
- 二、填写《计划书》时要求科学严谨、实事求是、表述清晰、准确。《计划书》经国家自然科学基金委员会相关项目管理部门审核批准后，将作为项目研究计划执行和检查、验收的依据。
- 三、《计划书》各部分填写要求如下：
 - （一）简表：由系统自动生成。
 - （二）摘要及关键词：各类获资助项目都必须填写中、英文摘要及关键词。
 - （三）项目组主要成员：计划书中列出姓名的项目组主要成员由系统自动生成，与申请书原成员保持一致，不可随意调整。如果批准通知中“项目评审意见及修改意见表”中“对研究方案的修改意见”栏目有调整项目组成员相关要求的，待项目开始执行后，按照项目成员变更程序另行办理。
 - （四）资金预算表：根据批准资助的直接费用，按照《国家自然科学基金项目预算表编制说明》填报资金预算表和预算说明书。国家重大科研仪器研制项目、重大项目还应按照预算评审后批复的直接费用各科目金额填报资金预算表、预算说明书及相应的预算明细表。
 - （五）正文：
 1. 面上项目、青年科学基金项目、地区科学基金项目：如果《批准通知》中没有修改要求的，只需选择“研究内容和研究目标按照申请书执行”即可；如果《批准通知》中“项目评审意见及修改意见表”中“对研究方案的修改意见”栏目明确要求调整研究期限和研究内容等的，须选择“根据研究方案修改意见更改”并填报相关修改内容。
 2. 重点项目、重点国际（地区）合作研究项目、重大项目、国家重大科研仪器研制项目：须选择“根据研究方案修改意见更改”，根据《批准通知》的要求填写研究（研制）内容，不得自行降低、更改研究目标（或仪器研制的技术性能与主要技术指标以及验收技术指标）或缩减研究（研制）内容。此外，还要突出以下几点：
 - （1）研究的难点和在实施过程中可能遇到的问题（或仪器研制风险），拟采用的研究（研制）方案和技术路线；
 - （2）项目主要参与者分工，合作研究单位之间的关系与分工，重大项目还需说明课题之间的关联；
 - （3）详细的年度研究（研制）计划。



3. 国家杰出青年科学基金、优秀青年科学基金和海外及港澳学者合作研究基金项目：须选择“根据研究方案修改意见更改”，按下列提纲撰写：
 - (1) 研究方向；
 - (2) 结合国内外研究现状，说明研究工作的学术思想和科学意义（限两个页面）；
 - (3) 研究内容、研究方案及预期目标（限两个页面）；
 - (4) 年度研究计划；
 - (5) 研究队伍的组成情况。
4. 国家自然科学基金基础科学中心项目：须选择“根据研究方案修改意见更改”，应当根据评审委员会和现场考察专家组的意见和建议，进一步完善并细化研究计划，作为评估和验收的依据。按下列提纲撰写：
 - (1) 五年拟开展的研究工作（包括主要研究方向、关键科学问题与研究内容）；
 - (2) 研究方案（包括骨干成员之间的分工及合作方式、学科交叉融合研究计划等）；
 - (3) 年度研究计划；
 - (4) 五年预期目标和可能取得的重大突破等；
 - (5) 研究队伍的组成情况。
5. 对于其他类型项目，参照面上项目的方式进行选择和填写。



简表

申请者信息	姓名	钱骏	性别	男	出生年月	1981年07月	民族	汉族	
	学位	博士			职称	教授			
	是否在站博士后	否		电子邮件	qianjun@zju.edu.cn				
	电话	0571-88206515转215		个人网页	http://mypage.zju.edu.cn/qianjun				
	工作单位	浙江大学							
	所在院系所	光电科学与工程学院							
依托单位信息	名称	浙江大学					代码	31005808A1112	
	联系人	薛建龙		电子邮件	new@zju.edu.cn				
	电话	0571-88981080		网站地址	www.zju.edu.cn				
合作单位信息	单位名称								
项目基本信息	项目名称	CW光激发的ICG近红外反斯托克斯荧光特性及其活体功能应用							
	资助类别	面上项目			亚类说明				
	附注说明								
	申请代码	F051201:光学探针、标记与光学成像			F051206:医学光学诊断与治疗				
	基地类别	现代光学仪器国家重点实验室							
	执行年限	2020.01-2023.12							
	直接费用	63万元							



科学问题属性

- “鼓励探索，突出原创”：科学问题源于科研人员的灵感和新思想，且具有鲜明的首创性特征，旨在通过自由探索产出从无到有的原创性成果。
- “聚焦前沿，独辟蹊径”：科学问题源于世界科技前沿的热点、难点和新兴领域，且具有鲜明的引领性或开创性特征，旨在通过独辟蹊径取得开拓性成果，引领或拓展科学前沿。
- “需求牵引，突破瓶颈”：科学问题源于国家重大需求和经济主战场，且具有鲜明的需求导向、问题导向和目标导向特征，旨在通过解决技术瓶颈背后的核心科学问题，促使基础研究成果走向应用。
- “共性导向，交叉融通”：科学问题源于多学科领域交叉的共性难题，具有鲜明的学科交叉特征，旨在通过交叉研究产出重大科学突破，促进分科知识融通发展为完整的知识体系。

请阐明选择该科学问题属性的理由（800字以内）：

反斯托克斯发光能将长波长(低能量)的激发光子转换为短波长(高能量)的发射光子，因此，反斯托克斯发光生物成像具有信噪比高、深度大和光损伤小等众多优势。多光子荧光成像和基于稀土纳米颗粒的上转换发光成像是目前研究最广泛的两种反斯托克斯荧光生物成像方式，引起了国内外研究者的广泛关注。与它们不同的是，基于热带吸收的反斯托克斯发光可通过CW激光激发实现，且发光强度显著依赖于温度，此外，它还具有光致漂白效应不明显，能产生光致制冷效应等优势。目前，它已被逐渐用于生物成像、温度传感等。遗憾的是，由于缺乏激发和荧光发射波长都位于近红外波段、且具有高生物兼容性、可代谢的小分子探针，基于热带吸收的反斯托克斯发光成像目前很少被用于活体研究。为了解决这一问题，申请人独辟蹊径，通过仔细观察与对比，发现吲哚菁绿（ICG）这一唯一在临床上批准使用的近红外荧光成像造影剂的分子结构和典型的热带吸收分子polymethiine的结构相似，表明它的振动能级较丰富；此外，ICG还具有大的吸收、荧光发射效率以及小的斯托克斯频移——以上特征表明ICG很好地符合了热带吸收材料的基本光学、化学特征。通过前期研究，申请人已证明ICG具有反斯托克斯荧光，且其是基于热带吸收而产生的。鉴于此，申请人将在本项目中对ICG的热带吸收诱导反斯托克斯发光特性进行系统研究，搭建反斯托克斯荧光小动物全身成像系统、扫描显微成像系统等，开展ICG在活体功能成像、光热治疗、生物调控中的应用，如：小动物全身成像、脑血管扫描显微成像、活体光热治疗过程中温度的实时监测、光致制冷生物调控等。填补热带吸收小分子材料在近红外波段以及活体应用中的空缺，在反斯托克斯发光生物成像这一前沿热点领域取得开拓性成果，为材料化学研究者们开发新的近红外热带吸收材料提供借鉴，为将来的基础医学研究和潜在的临床应用提供参考。



项目摘要

中文摘要:

反斯托克斯发光生物成像具有信噪比高、深度大和光损伤小等众多优势。基于热带吸收的反斯托克斯发光可通过CW激光激发实现，且显著依赖于温度，已被逐渐用于生物成像、温度传感等。然而，由于缺乏激发和荧光发射波长都位于近红外波段、且具有高生物兼容性、可代谢的小分子探针，基于热带吸收的反斯托克斯发光成像很少被用于活体研究。在本项目中，我们拟对唯一在临床上使用的近红外荧光成像造影剂ICG的热带吸收诱导反斯托克斯发光特性进行系统研究，搭建反斯托克斯荧光小动物全身成像系统、扫描显微成像系统等，开展ICG在活体功能成像、光热治疗、生物调控中的应用，如：小动物全身成像、脑血管扫描显微成像、活体光热治疗过程中温度的实时监测、光致制冷生物调控等。为材料化学研究者们开发新的近红外热带吸收材料提供借鉴，为将来的基础医学研究和潜在的临床应用提供参考。

Abstract:

Anti-stokes luminescence bioimaging possesses the advantages of high signal to noise ratio, large penetration depth and low photon-damage. Anti-stokes luminescence based on hot-band absorption can be directly excited by the continuous wave (CW) laser and is highly dependent on the temperature, and has been gradually employed for bioimaging, temperature sensing and so on. However, due to the lack of biocompatible and clearable small-molecule probes whose excitation and emission wavelength are both in the near infrared (NIR) spectral region, optical bioimaging based on hot-band absorption induced anti-stokes luminescence are rarely utilized for in vivo study. In this proposed project, we will systematically investigate the hot-band absorption induced anti-stokes luminescence features of indocyanine green (ICG), which is the only kind of NIR optical contrast agent adopted in clinically applications. We will further build anti-stokes fluorescence in vivo whole-body and scanning microscopic imaging systems, and utilize ICG for in vivo functional imaging, photothermal therapy, and biological regulating, including small animal whole-body organ imaging, real-time temperature monitoring during in vivo photothermal therapy, photon-induced cooling for biological stimulation, and so on. We really hope that our work can provide references for developing new NIR-emitted hot-band absorption materials, as well as be helpful for the future basic medical research and potential clinical applications.

关键词(用分号分开): 荧光脂质体; 吲哚菁绿; 热带吸收; 反斯托克斯发光; 活体功能应用

Keywords(用分号分开): fluorescent liposome; indocyanine green (ICG); hot-band absorption; anti-stokes luminescence; in vivo functional applications



项目组主要成员

编号	姓名	出生年月	性别	职称	学位	单位名称	电话	证件号码	项目分工	每年工作时间(月)
1	钱骏	1981.07	男	教授	博士	浙江大学	0571-88206515 转215	33068119810726 1555	项目负责人	6
2	阿卜杜热合曼·则比布拉	1987.04	男	医师	博士	浙江大学	15924110078	65312319870428 1112	活体和临床(如有) 光学生物成像	3
3	冯哲	1995.10	男	博士生	学士	浙江大学	18530193366	41088319951015 0319	开展活体光学生物 治疗和调控	9
4	周静	1995.12	女	博士生	学士	浙江大学	18888763019	33068219951222 0926	研究ICG反斯托克斯 发光等光学特性、 搭建光学成像系统	9
5	何木斌	1996.11	男	博士生	学士	浙江大学	17816890181	36253119961104 0316	开展活体光学生物 成像	9
6	薛丁玮	1992.08	男	博士生	学士	浙江大学	15700179920	33022619920827 2892	开展活体光学生物 治疗	6
7	朱亮	1994.03	男	博士生	学士	浙江大学	15868181658	33052219940330 3915	开展活体光学生物 调控	4
8	蔡朝冲	1994.12	男	硕士生	学士	浙江大学	13291899389	36233019941208 5039	搭建光学成像系统	9
9	倪沪桅	1995.03	男	硕士生	学士	浙江大学	18868109583	33038219950318 4090	搭建光学成像系统	9
总人数				高级	中级	初级	博士后	博士生	硕士生	
9				1	1			5	2	



项目批准号	62035011
申请代码	F0511
归口管理部门	
依托单位代码	31005808A1112-2096



620350111005526

国家自然科学基金委员会 资助项目计划书

资助类别： 重点项目

亚类说明： _____

附注说明： 光学成像介导的活体肿瘤微环境调控研究

项目名称： 无标记受激辐射寿命成像介导的活体肿瘤微环境调控研究

直接费用： 296万元 执行年限： 2021.01-2025.12

负责人： 丁志华

通讯地址： 浙江省杭州市浙大路38号浙江大学玉泉校区光电学院

邮政编码： 310027 电 话： 0571-87951194

电子邮件： zh_ding@zju.edu.cn

依托单位： 浙江大学

联系人： 薛建龙 电 话： 0571-88981080

填表日期： _____ 2020年10月01日

国家自然科学基金委员会制



国家自然科学基金委员会资助项目计划书填报说明

- 一、项目负责人收到《关于国家自然科学基金资助项目批准及有关事项的通知》（简称《批准通知》）后，请认真阅读本填报说明，参照国家自然科学基金相关项目管理办法和《国家自然科学基金资助项目资金管理办法》（请查阅国家自然科学基金委员会官方网站首页“政策法规”栏目），按《批准通知》的要求认真填写和提交《国家自然科学基金委员会资助项目计划书》（简称《计划书》）。
- 二、填写《计划书》时要科学严谨、实事求是、表述清晰、准确。《计划书》经国家自然科学基金委员会相关项目管理部门审核批准后，将作为项目研究计划执行、检查和验收的依据。
- 三、《计划书》各部分填写要求如下：
 - （一）简表：由系统自动生成。
 - （二）摘要及关键词：各类获资助项目都应当填写中、英文摘要及关键词。
 - （三）项目组主要成员：计划书中列出姓名的项目组主要成员由系统自动生成，与申请书原成员保持一致，不可随意调整。如果批准通知中“项目评审意见及修改意见表”中“对研究方案的修改意见”栏目有调整项目组成员相关要求的，待项目开始执行后，按照项目成员变更程序另行办理。
 - （四）资金预算表：根据批准资助的直接费用，按照《国家自然科学基金项目预算表编制说明》填报资金预算表和预算说明书。国家重大科研仪器研制项目、重大项目还应按照预算评审后批复的直接费用各科目金额填报资金预算表、预算说明书及相应的预算明细表。国家杰出青年科学基金项目资助经费试行包干制管理，无需填报资金预算表和预算说明书。
 - （五）正文：
 1. 面上项目、青年科学基金项目、地区科学基金项目：如果《批准通知》中没有修改要求的，只需选择“研究内容和研究目标按照申请书执行”即可；如果《批准通知》中“项目评审意见及修改意见表”中“对研究方案的修改意见”栏目明确要求调整研究期限和研究内容等的，须选择“根据研究方案修改意见更改”并填报相关修改内容。
 2. 重点项目、重点国际（地区）合作研究项目、重大项目、国家重大科研仪器研制项目、原创探索计划项目：须选择“根据研究方案修改意见更改”，根据《批准通知》的要求填写研究（研制）内容，不得自行降低、更改研究目标（或仪器研制的技术性能与主要技术指标以及验收技术指标）或缩减研究（研制）内容。此外，还要突出以下几点：
 - （1）研究的难点和在实施过程中可能遇到的问题（或仪器研制风险），拟采用的研究（研制）方案和技术路线；
 - （2）项目主要参与者分工，合作研究单位（如有）之间的关系与分工，重大项目还需说明课题之间的关联；
 - （3）详细的年度研究（研制）计划。



3. 国家杰出青年科学基金、优秀青年科学基金和创新研究群体项目：须选择“根据研究方案修改意见更改”，按下列提纲撰写：
 - (1) 研究方向；
 - (2) 结合国内外研究现状，说明研究工作的学术思想和科学意义（限两个页面）；
 - (3) 研究内容、研究方案及预期目标（限两个页面）；
 - (4) 年度研究计划；
 - (5) 研究队伍的组成情况。
4. 国家自然科学基金基础科学中心项目：须选择“根据研究方案修改意见更改”，应当根据评审委员会和现场考察专家组的意见和建议，进一步完善并细化研究计划，作为评估和验收的依据。按下列提纲撰写：
 - (1) 五年拟开展的研究工作（包括主要研究方向、关键科学问题与研究内容）；
 - (2) 研究方案（包括骨干成员之间的分工及合作方式、学科交叉融合研究计划等）；
 - (3) 年度研究计划；
 - (4) 五年预期目标和可能取得的重大突破等；
 - (5) 研究队伍的组成情况。
5. 对于其他类型项目，参照面上项目的方式进行选择和填写。



简表

项目负责人信息	姓名	丁志华	性别	男	出生年月	1967年10月	民族	汉族	
	学位	博士			职称	教授			
	是否在站博士后	否		电子邮件	zh_ding@zju.edu.cn				
	电话	0571-87951194		个人网页					
	工作单位	浙江大学							
	所在院系所	光电科学与工程学院							
依托单位信息	名称	浙江大学					代码	31005808A1112	
	联系人	薛建龙		电子邮件	new@zju.edu.cn				
	电话	0571-88981080		网站地址	www.zju.edu.cn				
合作单位信息	单位名称								
	新疆医科大学								
项目基本信息	项目名称	无标记受激辐射寿命成像介导的活体肿瘤微环境调控研究							
	资助类别	重点项目			亚类说明				
	附注说明	光学成像介导的活体肿瘤微环境调控研究							
	申请代码	F0511:生物、医学光学与光子学							
	基地类别	现代光学仪器国家重点实验室							
	执行年限	2021.01-2025.12							
	直接费用	296万元							



科学问题属性

- “鼓励探索，突出原创”：科学问题源于科研人员的灵感和新思想，且具有鲜明的首创性特征，旨在通过自由探索产出从无到有的原创性成果。
- “聚焦前沿，独辟蹊径”：科学问题源于世界科技前沿的热点、难点和新兴领域，且具有鲜明的引领性或开创性特征，旨在通过独辟蹊径取得开拓性成果，引领或拓展科学前沿。
- “需求牵引，突破瓶颈”：科学问题源于国家重大需求和经济主战场，且具有鲜明的需求导向、问题导向和目标导向特征，旨在通过解决技术瓶颈背后的核心科学问题，促使基础研究成果走向应用。
- “共性导向，交叉融通”：科学问题源于多学科领域交叉的共性难题，具有鲜明的学科交叉特征，旨在通过交叉研究产出重大科学突破，促进分科知识融通发展为完整的知识体系。

请阐明选择该科学问题属性的理由（800字以内）：

尽管发展了手术治疗、放射性治疗、化学治疗、分子靶向药物治疗，以及免疫疗法等，目前恶性肿瘤的治疗效果仍不尽如人意，主要表现为治疗本身的毒副作用、肿瘤的耐药、以及治疗后肿瘤的复发与转移等，而肿瘤微环境的组织缺氧、弱酸性等生理特征被认为是影响治疗效果的重要因素。调控肿瘤微环境，干预肿瘤细胞的新陈代谢水平，成为了改善肿瘤治疗效果的国际热点课题。但目前缺乏检测细胞新陈代谢水平的有效手段。时间分辨寿命成像是一种高灵敏的方法，但现有技术存在诸多局限性，如成像速度难以适应活体检测、需要外源性的标记物、不能针对非荧光样品等，限制了其对活体肿瘤组织的检测能力，制约了肿瘤调控研究中对纳米载体体系和细胞间相互作用机制的揭示、对纳米粒子调控方案与效果的反馈、对配套抗肿瘤药物疗法的评估。

为此，本项目提出一种具有原始创新性的时间分辨寿命成像方法。基于受激辐射寿命成像机制，并引入基于谱域光学相干显微术的轴向并行探测方法，以实现代谢特异性非荧光/荧光物质的快速成像。其中，受激辐射突破了荧光物质的框架，可对非荧光色团实现寿命成像，拓展了代谢成像的应用范畴。同时，创造性地将相干探测的理念引入到受激辐射寿命成像中，通过轴向并行探测手段，预期在时间效率上比目前的荧光寿命成像提高约一个数量级。

本项目以宫颈癌为典型应用对象，研究以调节组织溶氧量、酸碱度等为目标、具备优化的药物负载率、肿瘤靶向性、微环境摄取率的纳米载体体系，构建基于受激辐射与相干探测的内窥式寿命成像系统，以适应宫颈癌的微环境调控与探测需求。开展量化的图像表征和多元参量的融合分析，精准解析宫颈癌微环境调控中的代谢途径改变，形成对纳米载体体系调控水平的定量评价与反馈，以期最终改善治疗方案。本项目无需任何外源性的标记而实现细胞代谢水平的精准描述，尽可能避免了标记物对活体肿瘤微环境的改变，为阐明肿瘤细胞的耐药、优化和创新肿瘤治疗手段提供了一种全新的思路。



项目摘要

中文摘要:

肿瘤微环境的组织乏氧和弱酸化等特征与肿瘤的转移、复发、耐药等密切相关。通过肿瘤微环境调控干预细胞新陈代谢水平是解决问题的可行途径，但是高灵敏的细胞代谢探测手段极度缺乏。代谢分子寿命成像是满足上述需求的潜在方法，但现有技术存在诸多局限性，如成像速度难以适应活体检测、依赖外源性标记物、不能针对非荧光样品等。本项目提出受激辐射寿命成像机制，引入基于谱域光学相干显微技术的轴向并行探测方法，可实现对非荧光/荧光物质的快速寿命成像，在成像速度上比现有方法提升一个数量级。本项目研发以调控宫颈组织溶氧量、酸碱度等目标的纳米载体体系，构建内窥式寿命成像系统，开展高度量化的图像表征，实现细胞代谢途径的精准描述，形成宫颈癌微环境调控水平的定量评价和反馈。本项目开辟了非荧光物质的寿命成像新技术，规避了外源性标记物对活体肿瘤微环境的改变，为阐明肿瘤细胞的耐药、优化和创新宫颈癌治疗手段提供了一种全新的思路。

Abstract:

Tumor microenvironment is characteristic of hypoxia and weak acidity, closely related to the metastasis, recurrence and drug-resistance. It is possible to solve the problem by altering cellular metabolism via tumor microenvironment regulation; however, there is lack of highly-sensitive detection approaches. Lifetime imaging of metabolic molecules is a potential promising approach, while it has several limitations, including its limited time-efficiency for in vivo imaging, relying on exogenous labels, and the inability to detect non-fluorescent samples. In this project, we have proposed the stimulated emission based time-resolved lifetime imaging mechanism, applied the parallel detection along the axial direction by frequency-domain optical coherence microscopy, so as to achieve fast lifetime imaging of both non-fluorescent and fluorescent specimens, with about one order of improvement in time-efficiency. We will develop nano-materials aiming at adjusting oxygen concentration and pH value of cervical tissues, build the lifetime imaging endoscope, and perform highly-quantitative image analysis, so as to achieve accurate description of cellular metabolism and quantitative feedback of regulation ability of the nano-materials in cervical cancer. This project provides a scheme that enables lifetime imaging for non-fluorescent specimens, avoids the possible disruptions to tumor microenvironment by exogenous labels, and provides new insights into understanding drug-resistance, as well as improving and/or developing treatments for cervical cancer.

关键词(用分号分开): 肿瘤微环境; 寿命成像; 受激辐射; 光学相干层析; 微环境调控

Keywords(用分号分开): Tumor microenvironment; Lifetime imaging; Stimulated emission; Optical coherence tomography; Microenvironment regulation

项目组主要成员

编号	姓名	出生年月	性别	职称	学位	单位名称	电话	证件号码	项目分工	每年工作时间(月)
1	丁志华	1967.10	男	教授	博士	浙江大学	0571-87951194	330106196710280578	项目负责人	6
2	努尔尼沙·阿力甫	1988.11	女	讲师	博士	新疆医科大学	15925692249	653101198811112025	纳米载运体系制备	6
3	胡燕军	1971.01	女	主任医师	博士	浙江大学	13588006497	330103197101240023	实验结果的医学解读	6
4	陈立峰	1971.01	男	副主任医师	硕士	浙江大学	13735867156	33010319710112003X	实验结果的医学分析	6
5	何木斌	1996.11	男	博士生	学士	浙江大学	17816890181	362531199611040316	操作动物实验	9
6	邱建榕	1993.09	男	博士生	学士	浙江大学	15267015639	36242819930902731X	光学系统构建	10
7	孟佳	1993.04	男	博士生	硕士	浙江大学	17717806216	130203199304053014	负责图像分析	10
8	杨珊珊	1991.09	女	博士生	硕士	浙江大学	18958088203	410922199109170324	光学系统搭建	10
9	韩涛	1995.12	男	硕士生	学士	浙江大学	18520729210	340802199512100212	光学系统搭建	10
10	王迪	1995.07	男	硕士生	学士	浙江大学	18868159915	610126199507037018	光学系统搭建	10
总人数				高级	中级	初级	博士后	博士生	硕士生	
10				3	1	0	0	4	2	